Chapter 6

APPLICATION OF MAGNETIC RESONANCE TECHNIQUES TO THE STUDY OF DEFECTS IN SOLIDS

J.-Martin Spaeth

1 INTRODUCTION

Point defects such as impurity atoms or ions or intrinsic defects such as vacancies, interstitials, or antisite defects in binary crystals or aggregates of these defects very often determine the bulk properties of a solid. For example, this occurs in ionic crystals, oxides, and, particularly, in semiconductors. Therefore, it is of prime interest for materials science to have methods that are able to determine the defect structures and to correlate them with the bulk properties of materials, like optical or electronic properties. The latter is very important for microelectronics and optoelectronics in semiconductors or for the production of tunable or high-power lasers, just to name two fields of actual worldwide interest. Radiation damage of solids and detection of ionizing radiation are other fields where the knowledge of the structures of the defects created and their interactions are absolutely necessary.

There are many methods to *characterize* solids, a term currently used often in semiconductor research and technology. However, with a closer look, very few methods can determine defect structures, let alone determine them accurately on a microscopic or *atomic* scale. Local vibrational mode (LVM) spectroscopy can often determine the impurity that is involved in a defect and the defect symmetry, but correlation to other properties is not easily possible. Mössbauer effect, perturbed angular correlation (PAC), and other methods of the so-called nuclear solid state physics can frequently offer information about the symmetry of a defect and about nuclear quadrupole interactions with a very high sensitivity. The method is restricted, however, to a few suitable nuclei that must be incorporated into the solid for this investigation, which also limits their use.

Paramagnetic resonance is the most powerful technique; however, it is useful only when the defects are paramagnetic. Fortunately, this is very often the case, especially when transition metals or rare earth ions are involved. In radiation damage, where electron and hole pairs are created, and in semiconductors, where upon doping the Fermi level can often be suitably shifted, the defects of interest are or can be made paramagnetic.

Electron spin resonance (ESR) is a widely used method. Unfortunately, for the investigation of defects in solids it is suitable only in particularly favorable cases. In solids, generally, the ESR suffers from large line widths in contrast to its powerful use in chemistry. A combination of ESR and nuclear magnetic resonance (NMR), the so-called *electron nuclear double resonance* (*ENDOR*), is the most powerful tool, if it works for the specific defect under investigation. In materials science, ENDOR spectra are usually very complicated. This may be the reason why ENDOR spectroscopy in solids is not more popular. However, computer-assisted experiments and analysis of spectra, together with advanced ENDOR methods, made ENDOR spectroscopy quite feasible and of practical use beyond simple model cases, for which this spectroscopy was originally applied following its discovery in 1959 [1].

The number of defects needed for ENDOR in solids is about two orders of magnitude higher than necessary for detection by ESR, which limits the method to rather high defect concentrations of about 10^{15}–$10^{16}\mathrm{cm}^{-3}$ or more in most practical cases. Optical detection of ESR and ENDOR proved to be more sensitive by several orders of magnitude and therefore has received much attention recently, especially in semiconductor physics, where defect concentrations of $10^{15}\mathrm{cm}^{-3}$ and less are of technological importance and where thin layers are important for devices. These samples cannot be studied by conventional ESR and ENDOR because of the small volume and resulting small number of defects. Several other advantageous features of optical detection seem to be causing a revival of this kind of magnetic resonance spectroscopy. Among these features is the possibility of measuring ESR and ENDOR with high spatial resolution, which is very important from technological aspects, for example, when there is a need for electrically homogeneous large wafers for microelectronic and optoelectronic applications. This is a resolution that cannot be obtained for ESR by imaging techniques using magnetic field gradients as is done for NMR imaging.

This chapter reviews briefly the multiple magnetic resonance techniques presently available to determine the defect structures and to correlate defect structures with bulk properties. It outlines what can be accomplished. A precise analysis of the spectra is beyond the scope of this chapter. For convenience the examples used to illustrate the methods are taken largely from the recent work of the group at the University of Paderborn. Therefore, this is not a review in the sense of summarizing all work done in the field. Furthermore, it is assumed that the reader is familiar with the basic concepts and the realization of ESR, which is not discussed in detail. For this reference is especially made to McKinney and Goldberg [2] and textbooks [3–6]. In these textbooks the ESR of point defects in solids is discussed in detail. The ESR of transition metal ion impurities in solids is discussed comprehensively by Abragam and Bleaney [3].

This chapter does not deal with how to measure ENDOR using electron spin–echo methods. These methods have certain advantages, especially at low frequencies, but they also have serious disadvantages, especially in the regime of broad ESR lines and high ENDOR frequencies. The reader is referred to recent articles by Schweiger for these experimental methods [6].

2 STRUCTURE DETERMINATION OF DEFECTS BY MAGNETIC RESONANCE

2.1 Basic Concepts

The ability to determine defect structures by paramagnetic resonance spectroscopy is based on the measurement of the magnetic interaction between the magnetic moment of the unpaired electron(s) or hole(s) of the defect and the magnetic moments of nuclei belonging to the *impurity* atom of the defect (if any) and the atoms of its surrounding lattice. This interaction is usually called *hyperfine* (*hf*) *interaction* when it occurs between the unpaired electron (hole) and the central nucleus of the impurity atom, if such a defect is under study. It is called *superhyperfine* (*shf*) *interaction* or *ligand hyperfine* (*lhf*) *interaction* when it occurs between the magnetic moment of the unpaired electron (hole) and the magnetic moments of the nuclei of the surrounding lattice. In Figure 6.1 a schematic representation of a defect is shown, and the electron spin and the nuclear spins are indicated. The hyperfine interaction is often resolved in ESR; if the impurity nucleus occurs in several magnetic isotopes, then a chemical identification of the impurity is easily possible by taking advantage of the known magnetic moments, the ratio of which determines the ratio of the observed hyperfine splittings (see Section 3), and by measuring the ESR signal intensities, which reflect the natural abundance of the different isotopes. Unfortunately,

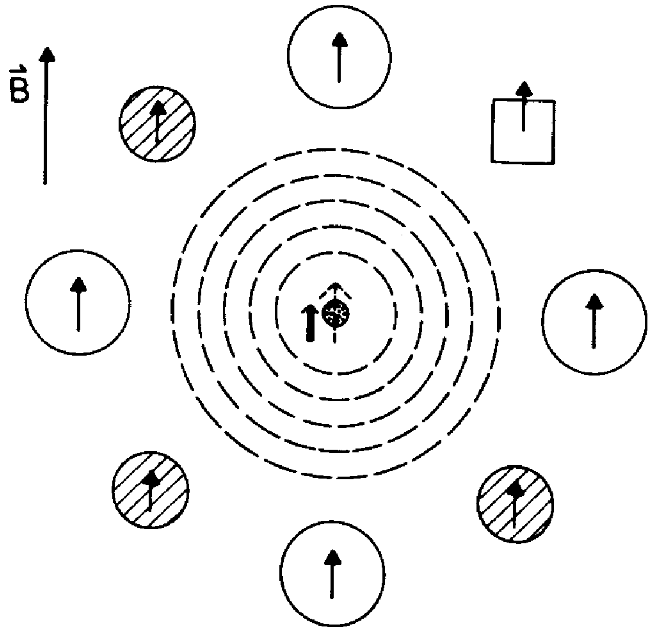

Figure 6.1 Schematic representation of a defect in a binary solid. The unpaired electron spin, electron spin density distribution, and nuclear spins of the lattice nuclei are indicated. The spins, which are aligned in an external static magnetic field **B**, are indicated by arrows. The open square represents a vacancy, which can have an unpaired electron spin due to dangling bonds at the neighboring atoms. The hatched and open circles represent two kinds of atoms or ions, for example, cations and anions in a binary ionic crystal.

there are important and common impurities, like oxygen, where over 99% of the isotopes are nonmagnetic. Here, a specific doping with a magnetic isotope (e.g., ^{17}O) may be necessary.

The g-factors (g-tensors) of the ESR spectra also contain information on the defect structure; they reflect the symmetry of the defects. The deviations of the principal values of the g-tensor from the g-value of the free electron ($g_e = 2.0023$) are due to the mixing of orbital contributions and the spin contribution to the total magnetic moment. This mixing is caused by the spin–orbit interaction. The orbital parts *see* the electrical crystal field around the defect and reflect therefore its symmetry [4, 5]. For a precise structure determination, apart from symmetry, the g-factor analysis usually does not yield enough reliable information, since excited-state energies, which are mostly unknown, are involved in the g-factor analysis [2, 3–6].

If it were possible to measure the NMR of the nuclei of the surrounding lattice, the local magnetic fields seen by the nuclei would give also the required information on the defect structure, since they are a superposition of the applied static magnetic field and the field equivalent of the superhyperfine or ligand hyperfine interactions. If the local fields of all the nuclei and their symmetry relation to the defect site were known, the structure of the defect, including the presence of vacancies and lattice distortions, can be derived. Unfortunately, however, NMR is not sensitive enough. One needs at least about 10^{19} nuclei like protons to measure NMR, while one deals with defect concentrations of 10^{16} cm^{-3} and less and sample volumes usually well below 1 cm^3.

Generally, in ESR the superhyperfine interaction is not well resolved; if it is at all, it is usually only with the nearest-neighbor nuclei. Therefore, ESR spectroscopy is often suitable for impurity identification by a resolved hyperfine interaction, but not for a precise microscopic structure determination. Recently, in fact, in GaAs several ESR spectra were observed with the same central ^{75}As hyperfine splitting and almost the same line width, which all belong to different defect structures. These different defects have only one common feature: an arsenic antisite; that is, an arsenic atom on a Ga site is involved. However, the remaining structure is different. By measuring only ESR one can be badly misled.

A higher resolution for the superhyperfine interactions and a higher sensitivity than obtained in NMR is achieved by measuring electron nuclear double resonance (ENDOR) [1]. The NMR transition of neighbor nuclei coupled to the unpaired electron causes a change of the electron spin polarization under suitable experimental conditions (partly saturated ESR), which can be detected as ENDOR signals (see Section 4). Thus, the NMR transitions are detected using a quantum transformation to higher quanta, the ESR microwave quanta, which results in a higher sensitivity. If we take one step further, that is, a quantum transformation to optical quanta, the optical detection of ESR and ENDOR is reached, which renders the measurement of superhyperfine interactions even more sensitive. This reason and the fact that there are less NMR lines compared to ESR superhyperfine lines from the same number of neighbor nuclei make the use of modern multiple resonance methods like ENDOR, ODESR (optically detected ESR), and ODENDOR (optically detected ENDOR) very useful when determining defect structures.

By resolving the superhyperfine interaction and the ligand quadrupole interactions one can determine the number and the symmetry relation of neighbor nuclei to the defect center and also the coupling constants such as superhyperfine and quadrupole constants. However, it is not possible to determine from the coupling constants the distance of the identified nuclei from the defect center without having a theoretical wave function for the defect electron (hole) or without assumptions about the radial part of this wave function, for example, whether it falls off monotonously with distance from the defect core. This is very often, but not always, the case. There may be oscillations of the unpaired spin density with distance especially for shallow defects in semiconductors. If a reasonable assumption about this radial part can be made, then a clear defect model can be derived unless there are special symmetry conditions where one cannot decide between possible sites. For example, this occurs for the substitutional and one tetrahedral interstitial site in the diamond structure where the same symmetry types of neighbor nuclei occur, only with a different sequence. If nothing is known about the wave function, one cannot decide on the site from ENDOR alone. For instance, this occurred recently for chalcogen defects in silicon [7].

2.2 Specific Problems in Materials Science

A single defect species in a simple single crystal is a rare case in materials science. Generally, in materials of interest, there are many defect species present simultaneously, very often with overlapping ESR spectra of very different signal intensity. Hence, the measurement of straight ENDOR usually results in such a complicated spectrum that an analysis is impossible. Here the use of a sort of excitation spectrum of ENDOR, *ENDOR-induced ESR* (sometimes called *field-swept ENDOR*), and *electron nuclear triple resonance* (*double ENDOR*) are of great help. With the latter method it is possible to measure separately the ENDOR spectra of one particular defect species (see Section 5.2). The selectivity is also high by using optical detection, since the absorption or emission bands of different defect species seldom overlap completely. Therefore, an optical transition specific to one defect species can be used for its exclusive measurement.

Another problem is connected with the correlation between bulk properties and the defects causing them. Obviously, by optical detection, a correlation can be made to optical properties of the crystals. Another problem is that of correlation to electrical properties that are usually characterized by the energy levels of a particular defect in the energy gap of a semiconductor. Here it is possible to perform photo-ESR, photo-ENDOR, photo-ODESR, and photo-ODENDOR experiments. The idea is to codope the material so that the energy level of the defect in question is not occupied. By irradiating the sample with light of variable energy one can lift electrons from the valence band and populate the energy levels so that a magnetic resonance measurement is possible. In this way a correlation to the energy levels of the defects can be achieved (see Section 6.6.1).

The work discussed in here refers to single crystals only; powders and amorphous materials are beyond the scope of this chapter.

3 ELECTRON SPIN RESONANCE

In a static magnetic field B_0 along the z axis of a laboratory system a free electron has the magnetic moment

$$\mu_z = -g_e \mu_B m_s \tag{1}$$

where g_e is the g-factor of the free electron ($g = 2.0023$), μ_B is the Bohr magneton ($\mu_B = e\hbar/2m_e = 9.274078 \cdot 10^{-24}\,\mathrm{A \cdot m^2}$), and m_s is the electron spin quantum number, $\pm\frac{1}{2}$. In a magnetic field the potential energy is

$$E = g_e \mu_B B_0 m_s \tag{2}$$

giving rise to the two electron Zeeman levels shown in Figure 6.2*a* as a function of the static magnetic field B_0. In the basic ESR experiment a magnetic dipole

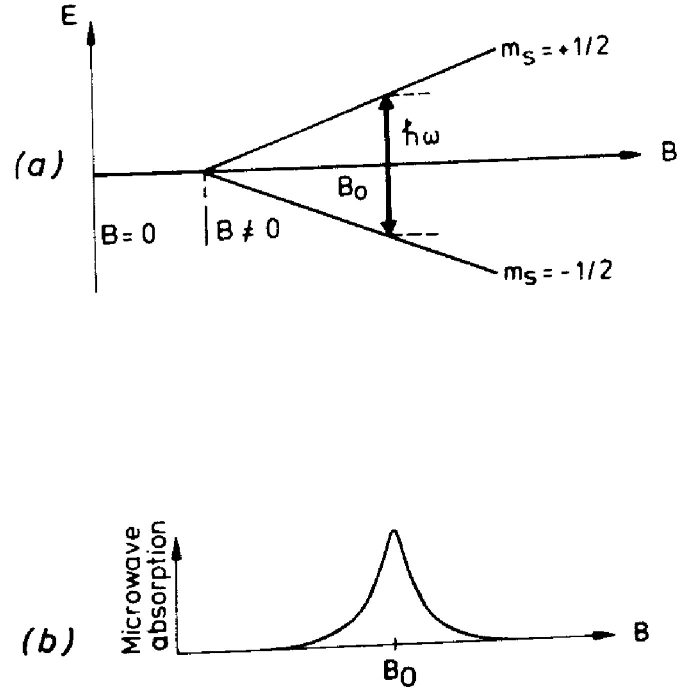

Figure 6.2 (*a*) Electron Zeeman levels for $S = \frac{1}{2}$ in $B = 0$ and $B \neq 0$. The magnetic dipole transition of the basic ESR experiment is indicated and occurs at $B = B_0$ for the microwave energy $\hbar\omega$. (*b*) Microwave absorption at $B = B_0$: the ESR line.

transition is induced between the Zeeman levels for $m_s = \pm\frac{1}{2}$ if the resonance condition

$$h\nu_{\text{ESR}} = g_e\mu_B B_0 \tag{3}$$

is fulfilled, where ν_{ESR} is the frequency of the oscillating magnetic field driving the transition [2–5]. The transition is characterized by $\Delta m_s = \pm 1$ as selection rule. Since $\nu_{\text{ESR}}/B_0 = g_e\mu_B/h = 2.802\,\text{MHz}/10^{-4}\text{T}$, the frequency is in the microwave region for the most commonly used magnetic fields. In solids one uses X band around 10 GHz ($B_0 = 0.35\,\text{T}$), K band around 24 GHz ($B_0 = 0.86\,\text{T}$), and Q band around 35 GHz ($B_0 = 1.2\,\text{T}$). For technical reasons one varies the magnetic field and keeps ν_{ESR} constant (Figure 6.2*b*). Upon resonance a microwave absorption is measured. To be able to use lock-in techniques for sensitivity enhancement one measures the derivative of the absorption as a consequence of magnetic field modulation [5].

In paramagnetic defects the electron is usually bound to an (impurity) atom or occupies a vacancy; therefore, the magnetism of the defect contains both spin and orbital angular momentum contributions. This is taken into account in the formalism of the effective spin and the spin Hamiltonian, which usually both refer to the ground state of the system that is of prime interest for the structure determination. For a justification and further details refer to the textbooks of ESR (e.g., [3–5]).

The spin Hamiltonian for the Zeeman interaction is

$$\mathscr{H} = \mu_B \mathbf{B}_0 \tilde{g} \mathbf{S} \tag{4}$$

where $\mathbf{S}$ is the operator of the effective spin, and $\tilde{g}$ is the g-tensor that reflects the symmetry of the defect [4, 5].

From (4) it follows that

$$E = \mu_B B_0 (g_x^2 l^2 + g_y^2 m^2 + g_z^2 n^2)^{1/2} m_s \qquad \text{and} \tag{5}$$

$$E = g\mu_B B_0 m_s \tag{6}$$

where g_x, g_y, and g_z are the principal values of the g-tensor in the principal axis form; l, m, and n are the direction cosines of the tensor orientation with respect to the laboratory frame: $l = \cos(x, x')$, $m = \cos(y, y')$, and $n = \cos(z, z')$, where x, y, z is the laboratory (crystal) axis system and (x', y', z') is that of the principal axes of the g-tensor. The deviations of the principal values of the g-tensor from the free electron value are caused by contributions of orbital angular momentum, which are mixed into the spin contributions by spin–orbit interactions. Their magnitude depends on both the spin–orbit interaction and the energy differences between the ground and excited states [5]. The electrical crystal field experienced by the defect, for example, by an impurity atom at its crystalline site, influences the defect energy through the orbital contributions to the magnetic moment. Therefore the ESR spectra are dependent on the relative orientation of the static magnetic field B_0 to the crystal axes. This is formally expressed by (5) and (6). A measurement of the angular dependence of the ESR spectrum for rotation of the magnetic field B_0 in one or several crystal planes reveals the symmetry of the crystal field experienced by the defect, and thus also reveals the symmetry of its electronic wave function [4, 5]. From ESR investigations often only this is known for a point defect in a single crystal, which then is *characterized* by its symmetry. If the defect has lower point symmetry than the crystalline site and hence several equivalent orientations are possible with respect to crystal symmetry operations, then in the experiment for a particular field orientation B_0 several defect orientations are measured simultaneously. If the g-anisotropy is not very big, the overlaps of such ESR lines can make an analysis difficult. Figure 6.3 shows a defect with C_{2v} symmetry. The defect is the singly ionized thermal donor *NL8* in silicon. The thermal donor has two (110) mirror planes and one twofold axis along [001] [8, 9]. For the orientation chosen in the spectrum of Figure 6.3*a* several defect orientations overlap. Figure 6.3*b* shows the angular dependence of the ESR spectra. The center orientations

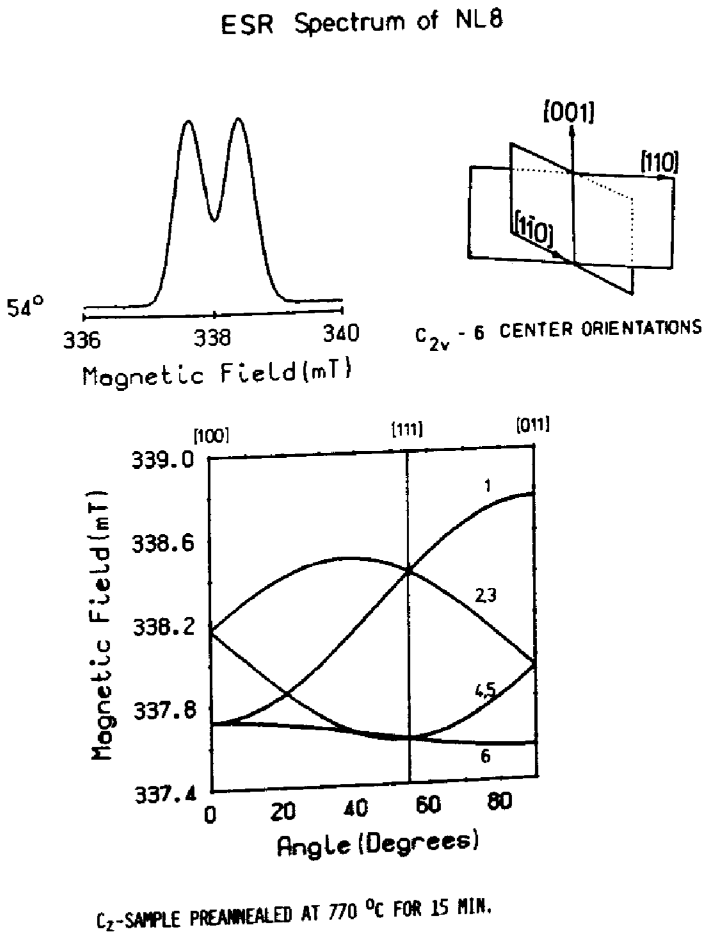

Figure 6.3 Angular dependence of the ESR spectrum of the thermal donors in silicon (so-called *NL8 ESR spectrum*) for rotation of B_0 in a (110) plane between ⟨100⟩ and ⟨011⟩. The different lines are caused by the g-factor anisotropy and the different center orientations in the crystal. The thermal donors have C_{2v} symmetry.

are noted. From the angular dependence the defect symmetry was inferred. Electron spin resonance does not reveal more information about the defect structure (see Section 4.4). The defect is formed by oxygen aggregation in silicon [8, 9].

When the defect contains several electrons (or holes) with parallel spin, the spin Hamiltonian must have additional terms caused by spin–orbit and crystal field effects. These terms are often called *fine-structure terms*. They depend on both the spin operator and the magnetic field. The term of lowest order in the spin, and the most important, is shown in (7) in addition to the electron Zeeman term [3].

$$\mathscr{H} = \mu_B B_0 \tilde{g} \mathbf{S} + \mathbf{S}\tilde{F}\mathbf{S} \tag{7}$$

For the simple case of axial symmetry of the defect the energy becomes (for an isotropic g-factor)

$$E = g_e \mu_B B_0 m_s + D/6\{[3\cos^2\theta - 1][3m_s^2 - S(S+1)]\} \tag{8}$$

where $D = \frac{3}{2}F_z$. Equation (8) is valid in perturbation theory of first order, that is, for the approximation that the fine-structure term is small compared to the electronic Zeeman term. The angle between the z axis of the fine-structure tensor in its principal axis system and the orientation of B_0 is θ [5]. There is no fine-structure splitting for $S = \frac{1}{2}$. For further details see, for example, [3, 5].

For $S = \frac{3}{2}$ Figure 6.4 shows that there are three allowed transitions for $\Delta m_s = \pm 1$; for $S = \frac{5}{2}$ there are five transitions. As an example Figure 6.5 shows

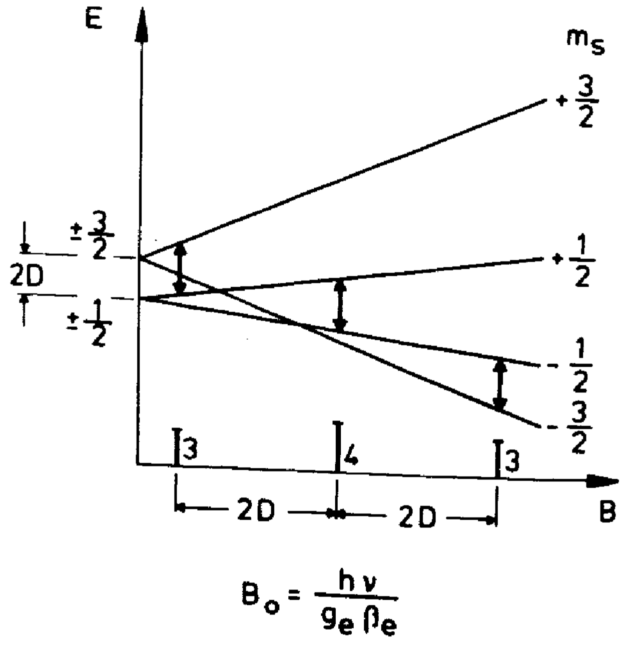

Figure 6.4 The ESR transitions for a defect with $S = \frac{3}{2}$ and fine-structure splitting.

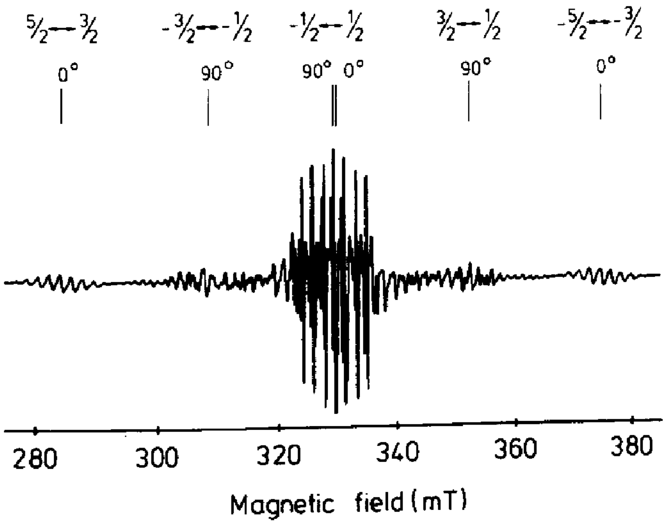

Figure 6.5 The ESR spectrum of Fe^{3+} defects in $RbCdF_3$ in the tetragonal phase. The fine-structure splitting is indicated by the m_s spin quantum numbers. The angles refer to the orientation between the axes of the domains and the external magnetic field, since the crystal contains several domains. Not all fine-structure transitions are marked by the m_s quantum numbers for all domain orientations. $B_0 \parallel \langle 100 \rangle$, $\nu_{ESR} = 9.26$ GHz, $T = 17$ K. Adapted from P. Studzinski, "Paramagnetische Ionen zur Untersuchung struktureller Phasenübergänge-Eine ENDOR Untersuchung," doctoral dissertation, Universität-GH-Paderborn, 1985.

the ESR spectrum of Fe^{3+} in $RbCdF_3$ in the low-temperature tetragonal phase. A superhyperfine structure with the six nearest ^{19}F neighbors is rather well resolved; Fe^{3+} substitutes for Cd^{2+}. All five fine-structure transitions expected for a $3d^5$ ($S = \frac{5}{2}$) configuration are seen. The transitions $-\frac{3}{2} \rightarrow -\frac{1}{2}$ and $+\frac{3}{2} \rightarrow \frac{1}{2}$ for the tetragonal defect axis parallel to B_0 (0°) are superimposed on those with perpendicular axes (90°), which are marked in Figure 6.5. Not all transitions for perpendicular axes are labeled with their spin quantum numbers in Figure 6.5 [10].

The fine-structure interaction results in a zero-field splitting. Whether a fine-structure splitting is observed depends on the specific configuration of the defect and the size of the splitting relative to the ESR line width. Therefore, it is not always easy to judge the spin state of a defect and thus its charge state from the ESR spectra. Figure 6.6 shows the ESR spectrum for Ni^{3+} in GaP [11, 12]; Ni^{3+} occupies a Ga site and has the configuration $3d^7$. There is no fine-structure splitting being resolved, and the spectrum appears to arise from a defect with $S = \frac{1}{2}$; in fact, it was shown by ENDOR that $S = \frac{3}{2}$ (see Section 4). The superhyperfine interaction with the four nearest ^{31}P neighbors is partly resolved for $B \parallel \langle 100 \rangle$.

For $S = \frac{1}{2}$ ESR lines are split by the hyperfine interaction. This splitting gives the most information on the microscopic nature of the defect in ESR.

The interaction is basically a magnetic dipole–dipole interaction, and it is described by the hyperfine tensor $\tilde{A}$ in the spin Hamiltonian

$$\mathcal{H} = g\mu_B \mathbf{B}_0 \mathbf{S} + \mathbf{I}\tilde{A}\mathbf{S} - g_I \mu_n \mathbf{B}_0 \mathbf{I} \tag{9}$$

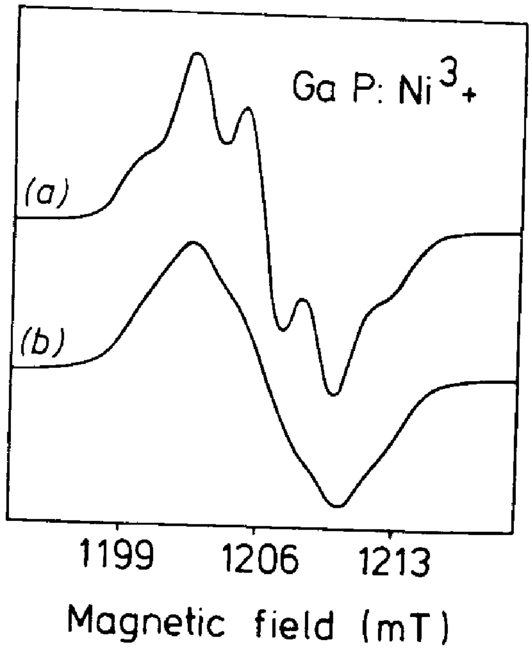

Figure 6.6 The ESR spectrum of Ni^{3+} ($3d^7$, $S = \frac{3}{2}$) on Ga sites in GaP: (*a*) $B_0 \parallel \langle 100 \rangle$, (*b*) $B_0 \parallel \langle 110 \rangle$. There is no fine-structure splitting observable. The partly resolved structure for $B_0 \parallel \langle 100 \rangle$ is caused by the superhyperfine interaction with four equivalent nearest ^{31}P neighbors. Reprinted with permission from *Solid State Commun.*, **25**, U. Kaufmann and J. Schneider, "ESR Assessment of $3d^7$ Transition Metal Impurity States in GaP, GaAs and InP," Copyright 1978, Pergamon Journals Ltd.

where μ_n is the nuclear magneton ($\mu_n = m_e/m_p\mu_B$), m_p is the proton mass, and g_I is the nuclear g-factor. For simplicity an isotropic electronic g-factor is assumed. In first-order perturbation theory one obtains the energy

$$E = g\mu_B B_0 m_s + A(\theta) m_I m_s \tag{10}$$

and the resonance frequency for $S = \frac{1}{2}$ is

$$h\nu_{ESR} = g_e \mu_B B_{res} + m_I A(\theta) \tag{11}$$

For $I = \frac{1}{2}$ there are two values of the nuclear spin quantum number $m_I = \pm\frac{1}{2}$. Since ν_{ESR} is kept constant, there are two resonance fields, which are separated by $A(\theta)/g_e\mu_B$ (see Figure 6.7).

Figure 6.8 shows how a hyperfine interaction can be used to identify a defect for the example of Te^+ defects in Si [7]. Ninety-two percent of the Te isotopes are diamagnetic and give rise to the central ESR line near 350 mT (measured in X band) corresponding to $g = 2$. The two magnetic isotopes ^{125}Te (7% abundant) and ^{123}Te (0.9% abundant) have $I = \frac{1}{2}$ and, according to (11), a doublet splitting. The ESR line intensities follow the isotope abundance, and the relative splittings are in the ratio of the respective nuclear moments [see (17) and (18)]. Therefore the defect is unambiguously identified as being caused by Te impurities. However, no further structure caused by the superhyperfine interactions is resolved. Therefore, the site of Te^+ in the lattice cannot be determined

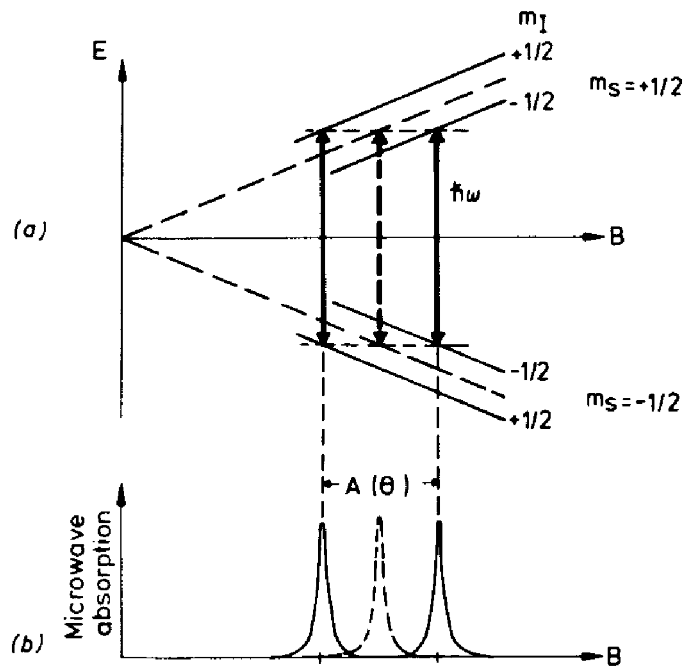

Figure 6.7 Electron Zeeman levels for an electron spin $S = \frac{1}{2}$ hyperfine coupled to a nuclear spin $I = \frac{1}{2}$ and the resulting ESR transitions with hyperfine splitting. The selection rule for the ESR transition is $\Delta m_s = \pm 1$, $\Delta m_I = 0$.

from ESR. The defect Te^+ has an isotropic hyperfine interaction. In general, the hyperfine interaction is anisotropic, and the spectrum is angular dependent as indicated in (11). In first order and for axial symmetry of the defect the resonance fields are given by

$$h\nu_{\text{ESR}} = g\mu_{\text{B}}B_{\text{res}} + m_I[a + b(3\cos^2\theta - 1)] \tag{12}$$

where a is the isotropic hyperfine constant, b is the anisotropic hyperfine constant, θ is the angle between the magnetic field B_0 and the principal axis z of

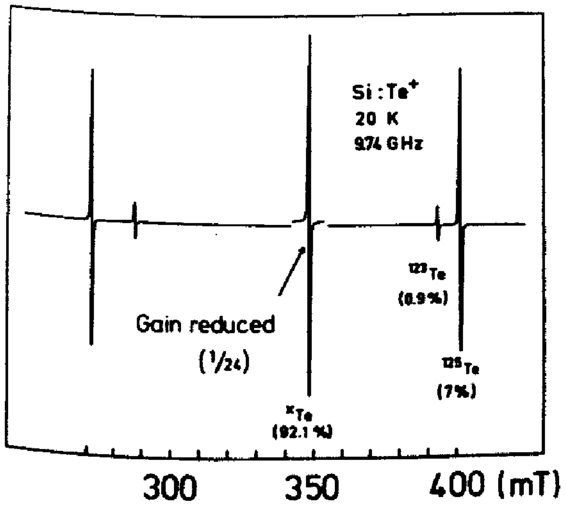

Figure 6.8 An ESR spectrum of Te^+ centers in Si. The g-factor is isotropic. The hyperfine splittings are caused by the two magnetic isotopes ^{125}Te and ^{123}Te with $I = \frac{1}{2}$. Reprinted with permission from H. G. Grimmeiss, E. Janzen, H. Ennen, O. Schirmer, *Phys. Rev. B*, **24**, 4571 (1981).

the hyperfine tensor. In general, the interaction constants a and b and b' are related to the principal values of the hyperfine tensor by

$$\tilde{A} = (a \cdot \tilde{I} + \tilde{B}) \tag{13}$$

$$b = \tfrac{1}{2}B_z \tag{14}$$

$$b' = \tfrac{1}{2}(B_x - B_y) \tag{15}$$

where b' describes the deviation from axial symmetry.

Figure 6.9a shows the ESR lines of Tl°(1) centers in KCl (and some other simultaneously produced defects by X irradiation of the Tl doped KCl crystal at

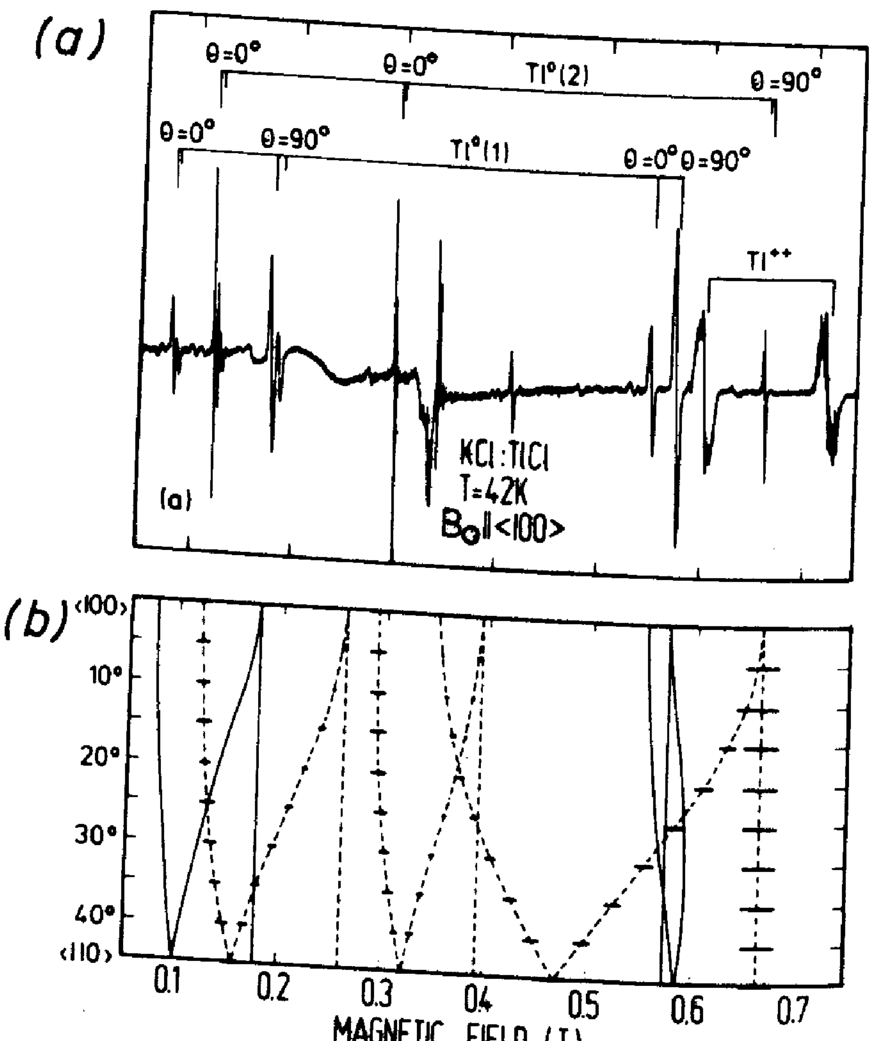

Figure 6.9 (a) ESR spectrum of Tl°(1) and Tl°(2) centers in KCL: Tl for $B_0 \| \langle 100 \rangle$ ($T = 4.2$ K). Tl°(1) centers are Tl° atoms next to a Cl-vacancy along a ⟨100⟩ direction, Tl°(2) centers are Tl° atoms located between two Cl⁻ vacancies along a ⟨100⟩ direction. (b) The calculated angular variation of the spectra in a (100) plane. Solid lines are caused by Tl°(1) centers; broken lines are caused by Tl°(2) centers. The horizontal bars indicate the transition probabilities for Tl°(2) centers. Reprinted with permission from E. Goovaerts, J. A. Andriessen, S. V. Nistor, and D. Schoemaker, *Phys. Rev. B*, **24**, 29 (1981).

room temperature). Again, since both Tl isotopes ^{203}Tl and ^{205}Tl have $I = \frac{1}{2}$, the spectra consist of doublets. The splitting is, however, angular dependent. The angular dependence in Figure 6.9*b* for rotation of the magnetic field in a (100)-plane shows this as well as the distribution of the centers in the crystal with respect to their axes. They have axial symmetry about a $\langle 100 \rangle$ direction. The Tl^0(1) centers are Tl^0 atoms next to an anion vacancy, while Tl^0(2) centers have two anion vacancies, one on each side of the atom [13]. The angular dependence (i.e., symmetry) and isotope splittings lead here to structural models. Electron spin resonance cannot reveal, however, whether Tl^0 resides precisely on a cation lattice site or whether it is relaxed toward the vacancy. Also, whether the vacancy is filled with another impurity is unknown since the angular dependence reflects only the tetragonal symmetry of the defect and no further superhyperfine structure is resolved. The distinction between Tl^0(1) and Tl^0(2) also requires a theoretical interpretation of the spin Hamiltonian parameters.

Figure 6.9*a* shows another feature of conventional ESR spectroscopy. Since the ionizing radiation producing these centers creates many defects simultaneously, it is not easy to assign unambiguously all the ESR lines to particular centers and then to follow their angular dependence. On what follows we show that with optical detection of the ESR each defect can be measured selectively, which greatly facilitates the analysis.

Figure 6.10 shows the ESR spectrum of atomic hydrogen on interstitial sites and on cation and anion vacancy sites in KCl [14]. The central hyperfine splitting with the proton ($I = \frac{1}{2}$) in the three cases is practically the same and nearly that of the free hydrogen atom. Only for the interstitial site is a superhyperfine interaction with nearest neighbors [14] resolved. The substitutional sites cannot be inferred from the ESR spectrum. They can be established only by resolving the superhyperfine interactions with ENDOR experiments [15].

If there is a superhyperfine interaction as in Figure 6.10*a*, the spin Hamiltonian of (9) must be extended to include all interacting nuclei

$$\mathscr{H} = g\mu_B \mathbf{B}_0 \mathbf{S} + \sum_i (\mathbf{I}_i \tilde{A}_i \mathbf{S} - g_{I,i}\mu_n \mathbf{B}_0 \mathbf{I}_i) \tag{16}$$

The sum runs over all nuclei with which a superhyperfine (hyperfine) interaction is measured. The intensity ratio of the superhyperfine lines is a characteristic feature and can be used to determine the number of interacting nuclei and their spins. This information is usually difficult to obtain from the analysis of ENDOR spectra. Therefore it is often useful or even necessary to simulate the ESR spectrum using the superhyperfine data obtained from the analysis of the ENDOR spectra to obtain the number of interacting nuclei. Especially, if there are several nuclei with the same superhyperfine interaction, which can occur for a specific orientation of the magnetic field, one can define a total nuclear spin $N \cdot I$, which leads to a $(2N \cdot I + 1)$-fold splitting of the ESR spectrum. Figure 6.11 shows the level scheme and the transitions of $N = 1$, 2, and 3 for $I = \frac{1}{2}$. The

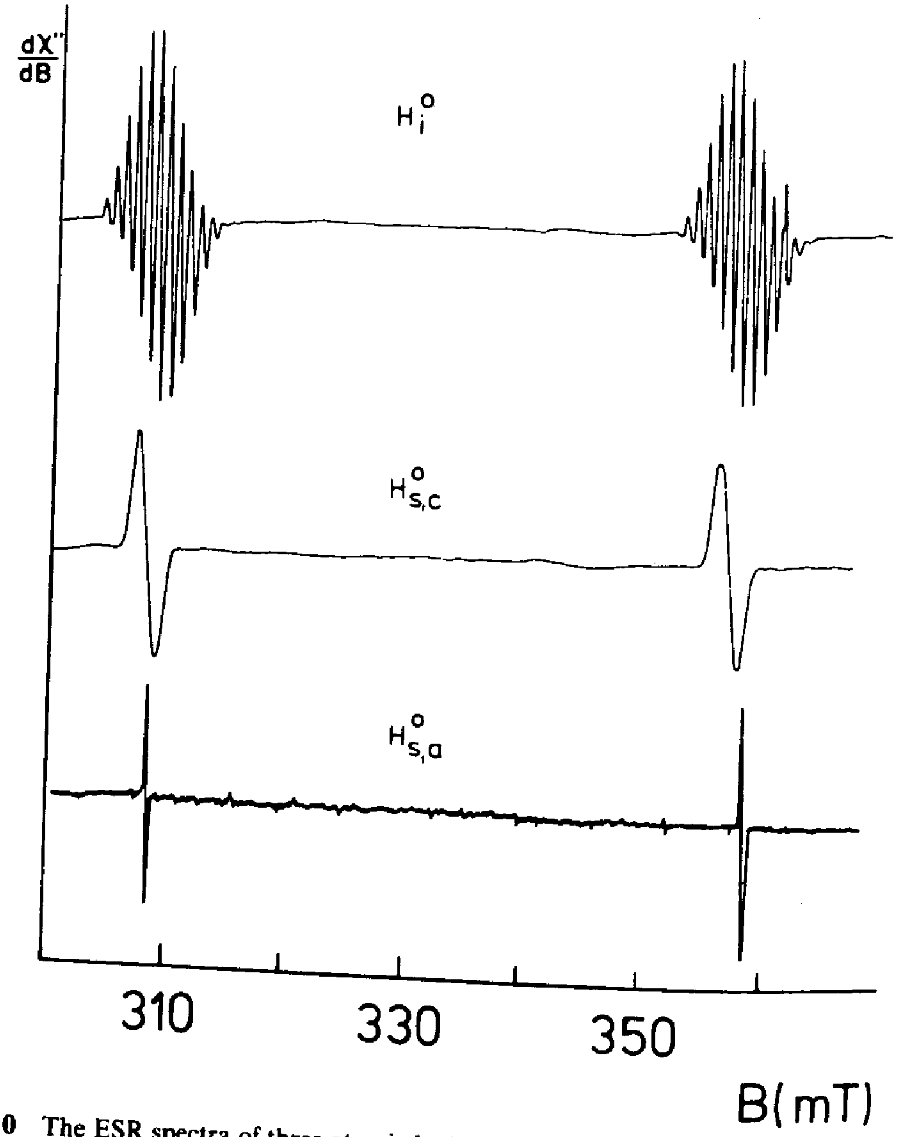

Figure 6.10 The ESR spectra of three atomic hydrogen centers in KCl. $B_0 \parallel \langle 100 \rangle$, $T = 77$ K. The hydrogen atoms occupy interstitial sites (H_i^0 centers), cation vacancy sites ($H_{s,c}^0$ centers), and anion vacancy sites ($H_{s,a}^0$ centers). The splitting caused by the hyperfine interaction with the proton is almost that of the free hydrogen atom. Reprinted with permission from J.-M. Spaeth, "Atomic Hydrogen as a Model Defect in Alkali Halides," in V. M. Tuchkevich and K. K. Shvarts, Eds., *Defects in Insulating Crystals*, Springer, New York, 1981, p. 232.

relative ESR signal height is given by the statistical weights or degeneracy of the levels. For $N = 3$ they are 1:3:3:1 for the four equidistant superhyperfine lines.

Tables 6.1 and 6.2 give the statistical weights of the states M_I for N equivalent nuclei with $I = \frac{1}{2}$ and $\frac{3}{2}$. From Table 6.2 one finds for four equivalent nuclei of $I = \frac{3}{2}$ the weights 1:4:10:20:31:40:44:40:31:20:10:4:1 for the 13 superhyperfine lines. This is observed in Figure 6.10*a* for the interstitial atomic hydrogen in KCl, which interacts predominantly with four nearest ^{35}Cl nuclei that have $I = \frac{3}{2}$.

In Section 6 the interpretation of the superhyperfine (hyperfine) and quadrupole (superhyperfine) interaction constants is discussed briefly. Here are some introductory remarks that may help to understand the forthcoming sections.

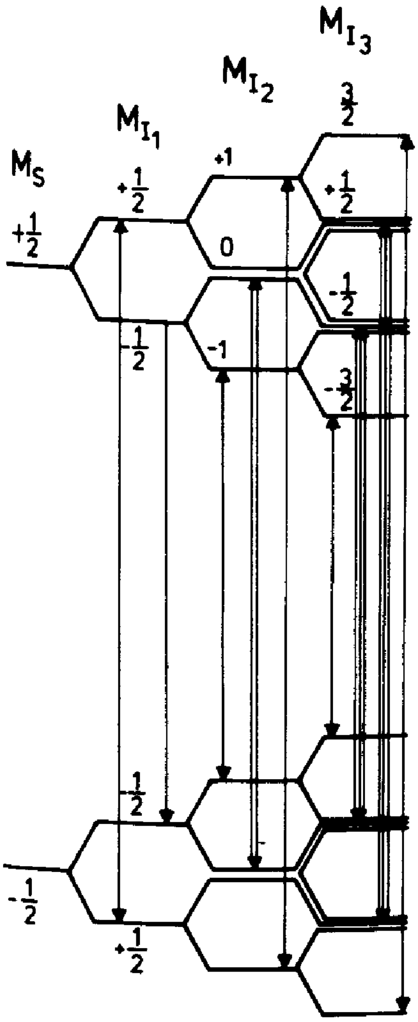

Figure 6.11 Electron Zeeman level scheme for an electron with superhyperfine coupling to three equivalent nuclei with $I = \frac{1}{2}$ and the resulting ESR transitions.

Table 6.1 Statistical Weights of the M_I States for N Equivalent Nuclei With Spin $\frac{1}{2}$

	M_I						
N	0	$\frac{1}{2}$	1	$\frac{3}{2}$	2	$\frac{5}{2}$	3
1		1					
2	2		1				
3		3		1			
4	6		4		1		
5		10		5		1	
6	20		15		6		1

Table 6.2 Statistical Weights of the M_I States for N Equivalent Nuclei With Spin $\frac{3}{2}$

N	M_I																		
	0	$\frac{1}{2}$	1	$\frac{3}{2}$	2	$\frac{5}{2}$	3	$\frac{7}{2}$	4	$\frac{9}{2}$	5	$\frac{11}{2}$	6	$\frac{13}{2}$	7	$\frac{15}{2}$	8	$\frac{17}{2}$	9
1		1		1															
2	4		3		2		1												
3		12		10		6		3		1									
4	44		40		31		20		10		4		1						
5		155		135		101		65		35		15		5		1			
6	580		546		456		336		216		120		56		21		6		1

The hyperfine interaction constants are determined by the electronic wave function of the defects and the nuclear moments of the nuclei. In a simple one-particle approximation the isotropic constant a is given by [4]

$$a_l = \tfrac{2}{3}\mu_0 g\mu_{\mathrm{B}} g_I \mu_{\mathrm{n}} |\psi(r_l)|^2 \tag{17}$$

where $\psi(r)$ is the wave function of the defect and $\psi(r_l)$ is its amplitude at the site r_l of a particular nucleus. The anisotropic tensor elements are given by

$$B_{ik} = \frac{\mu_0}{4\pi} g\mu_{\mathrm{B}} g_I \mu_{\mathrm{n}} \int \left(\tfrac{3}{5} x_i x_k - \frac{1}{r^3}\delta_{ik} \right) |\psi(r)|^2 \, dV \tag{18}$$

where r is the radius vector from the nuclear site of concern (origin) and the origin is spared in the integral of (18). Thus, the hyperfine constants are proportional to g_I; therefore, the interaction constants of different isotopes must be in the ratio of their respective g_I factors [4, 5]. This was used for their identification.

4 ELECTRON NUCLEAR DOUBLE RESONANCE

4.1 Stationary Electron Nuclear Double Resonance

In solids the superhyperfine structure of defects is usually not or only partly resolved by ESR. This is not because it is too small, but because the ESR spectrum is a superposition of too many superhyperfine lines with splittings that are very similar. In Figure 6.12 this is shown schematically for a $S = \frac{1}{2}$ defect and interactions with two shells of equivalent nuclei, each of which contains n_1 and n_2 nuclei with the spins I_1 and I_2, respectively. For both electron Zeeman levels there are $N = (2n_1 \cdot I_1 + 1)(2n_2 \cdot I_2 + 1)$ sublevels; therefore, there are up to N ESR transitions. If there is no quadrupole interaction, there are, however, only four ENDOR transitions, two for each shell of equivalent nuclei, which follows from the ENDOR selection rules as NMR transitions (see Section 4.2). If we consider more interactions, the result is an exponential increase of the number of superimposed ESR lines that are not resolved any more. For solid-state defects the interactions with up to 10 shells of neighbor nuclei are not unusual. The ESR shows only the envelope of all the superhyperfine transitions yielding an *inhomogeneously* broadened ESR line. Figure 6.3 is an example of the width of the ESR lines that is caused by unresolved superhyperfine interactions with several shells of ^{29}Si nuclei. In ENDOR there are only two lines for each superhyperfine-coupled nucleus distinguishable by their superhyperfine interactions. Therefore in ENDOR there is an excellent resolution of superhyperfine interactions.

There are two methods to measure ENDOR, without including spin–echo techniques: the dispersion method, which is suited for especially long spin–lattice relaxation times T_1. This method was introduced by Feher [1]. The other

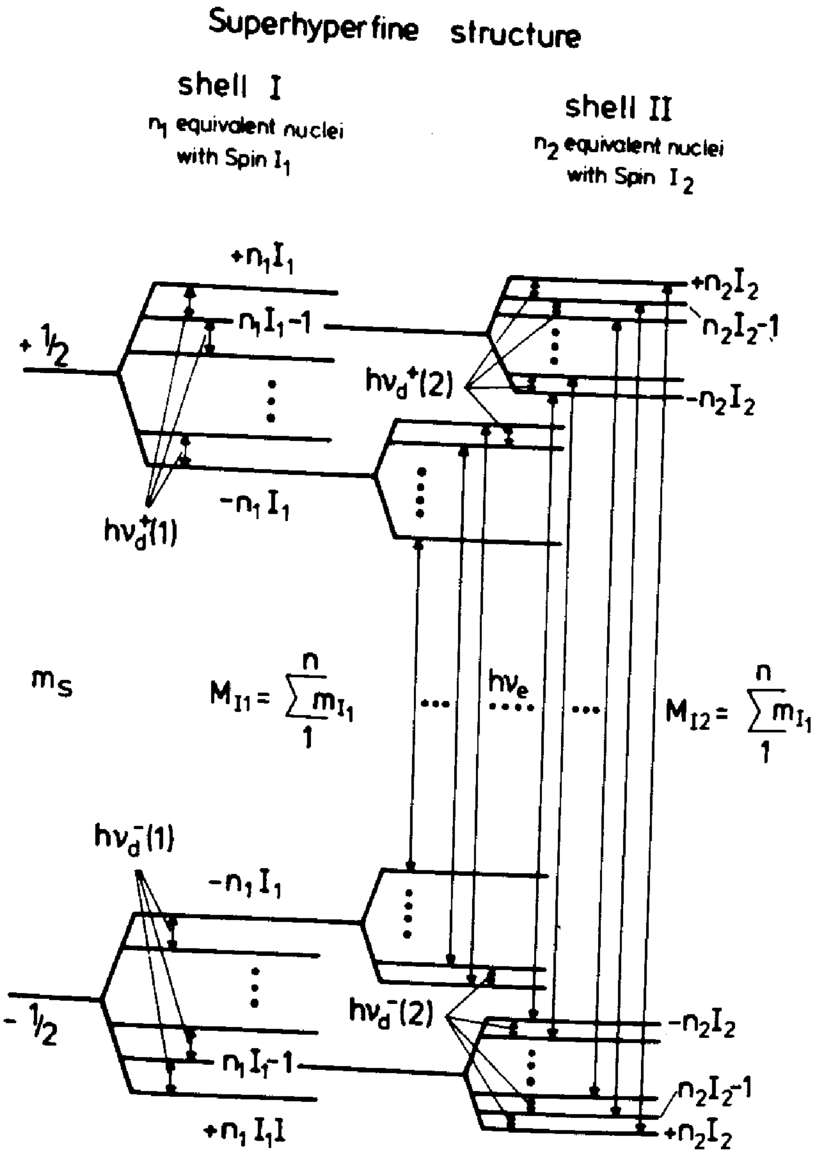

Figure 6.12 Energy-level scheme for an electron with superhyperfine coupling to several shells of equivalent nuclei. The ESR line is an envelope over all superhyperfine lines, which usually are not resolved because of the high number of superimposed lines.

one introduced by Seidel [16] is the stationary ENDOR method, which is more versatile. A quantitative description of both methods is difficult, since for solid-state defects the situation is so complicated by the relaxation paths and couplings that there is not yet a good, general understanding of the ENDOR effect. Since the purpose of this chapter is to show the application of ENDOR to the determination of defect structures, only the more commonly used stationary ENDOR technique is discussed by means of a simple working model to illustrate the experiments done.

Figure 6.13 shows schematically the allowed ESR transitions with resolved superhyperfine structure for $S = \frac{1}{2}$ and for one nucleus with $I = \frac{3}{2}$. In an ENDOR experiment one of the allowed ESR transitions is partially saturated; that is, one chooses the microwave power high enough so that the transition

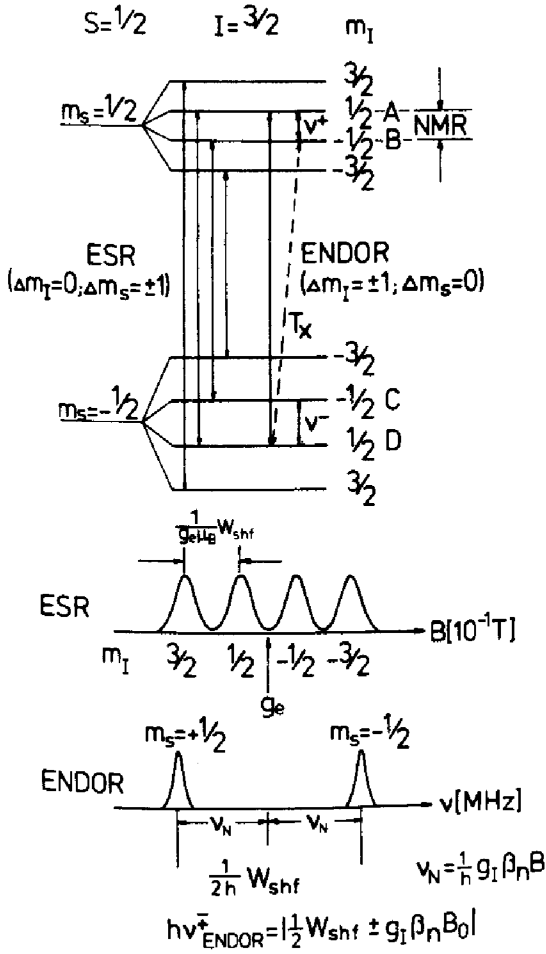

Figure 6.13 Energy-level diagram to explain stationary electron nuclear double resonance (ENDOR).

probability $R_{MW} = \gamma B_1^2$ is of the order or larger than the spin lattice relaxation rate $R_{REL} = 1/T_1$; γ is the gyromagnetic ratio of the electron, and B_1 is the microwave field amplitude. If that is the case, then the spin population of the levels connected by the microwave transitions deviates from the Boltzmann equilibrium distribution. If $R_{MW} \gg R_{REL}$, then these levels become equally populated. This results in a decrease of the observable microwave absorption, since microwave absorption and emission probabilities are equal. The levels unconnected by the microwave transitions are not affected. Therefore, for example, the level population $m_s = +\frac{1}{2}$, $m_I = +\frac{1}{2}$ becomes inverted with respect to the level $m_s = +\frac{1}{2}$, $m_I = -\frac{1}{2}$ (see Figure 6.13). If the two levels are connected by an NMR transition, the level populations can be equalized, which results in a population decrease of the level $m_s = +\frac{1}{2}$, $m_I = +\frac{1}{2}$ leading to desaturation of the (partially) saturated transition $m_s = -\frac{1}{2}$, $m_I = +\frac{1}{2}$ to $m_s = +\frac{1}{2}$, $m_I = +\frac{1}{2}$. This desaturation is monitored. It occurs for two NMR frequencies in the example of Figure 6.13, since the NMR frequencies for $m_s = +\frac{1}{2}$ and $m_s = -\frac{1}{2}$ are different (see Section 4.2). Thus, each nucleus gives rise to two ENDOR lines (for $S = \frac{1}{2}$). A cross relaxation T_x (see Figure 6.13) allows the stationary observation of the desaturation (stationary ENDOR) [16]. If several nuclei with the same or similar interactions are coupled to the unpaired electron, then the ESR pattern becomes complicated and the superhyperfine structure is usually

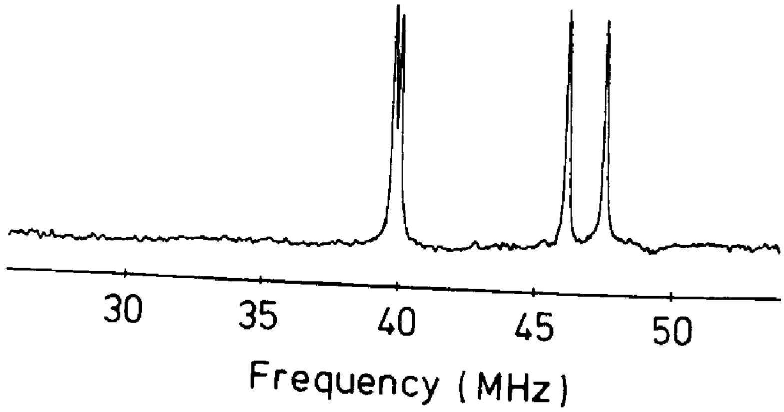

Figure 6.14 The ENDOR lines due to the nearest ^{19}F neighbors of $F(\mathrm{Cl}^-)$ centers in SrFCl; $F(\mathrm{Cl}^-)$ centers are electrons trapped at Cl^- vacancies in SrFCl.

not resolved. In ENDOR all nuclei with the same interaction give rise only to two (for $S = \frac{1}{2}$) ENDOR lines, which greatly enhances the resolution. Electron nuclear double resonance lines, as NMR lines, are typically 10–100 kHz wide, which is about three orders of magnitude narrower than homogeneous ESR lines. Thus, in ENDOR one uses the sensitivity enhancement caused by a quantum shift from frequencies of about megahertz to the microwave frequencies of about gigahertz and the increased resolution power caused by the smaller NMR line width and the reduction of the number of lines.

Figure 6.14 shows as an example ENDOR lines (ESR desaturation) of the nearest ^{19}F neighbors of $F(\mathrm{Cl}^-)$ centers in SrFCl (for $m_s = -\frac{1}{2}$), where the unpaired electron occupies a Cl^- vacancy. The structure model of BaFCl, which has the same structure, is shown in Figure 6.30 (see Section 5).

4.2 Analysis of Electron Nuclear Double Resonance Spectra

Generally, in addition to the superhyperfine interaction, there is a quadrupole interaction if $I > \frac{1}{2}$ for the interacting nuclei. This interaction is caused by the interaction between the electrical field gradient at the site of a nucleus and its nuclear quadrupole moment [4]. Therefore, the spin Hamiltonian describing the ENDOR spectra is

$$\mathscr{H} = g\mu_B B_0 S + \sum_l (\mathbf{S}\tilde{A}_l \mathbf{I}_l - g_l \beta_l B_0 \mathbf{I}_l + \mathbf{I}_l \tilde{Q}_l \mathbf{I}_l) \qquad (19)$$

The sum runs over all nuclei interacting with the unpaired electron. For simplicity it is assumed that g is isotropic (which is generally not the case); $\tilde{Q}$ is the traceless quadrupole interaction tensor with the elements

$$Q_{ik} = \frac{eQ}{2I(2I-1)} \frac{\partial^2 V}{\partial x_i \partial x_k}\bigg|_{r=0} \qquad (20)$$

where Q is the quadrupole moment and V is the electrical potential. The spectra are usually analyzed in terms of the quadrupole interaction constants:

$$q = \tfrac{1}{2}Q_z$$
$$q' = \tfrac{1}{2}(Q_x - Q_y) \tag{21}$$

The selection rule for ENDOR transitions as NMR transitions is

$$\Delta m_s = 0$$
$$\Delta m_I = \pm 1 \tag{22}$$

If the superhyperfine and quadrupole interactions are small compared to the electron Zeeman term, then the quantization of the electron spin is not influenced by these interactions and the nuclei are independent of each other. They can be treated separately, and the sum in (19) can be omitted. In first-order perturbation theory, that is, with the conditions

$$|B_{ik}|,\ |Q_{ik}| \ll \left| a \pm \frac{1}{m_s} g_I \mu_n B_0 \right| \tag{23}$$

$$\nu^{\pm}_{\mathrm{ENDOR}} = \left| \frac{1}{h} m_s W_{\mathrm{shf}} \pm \nu_n \pm \frac{1}{h} m_q W_Q \right| \tag{24}$$

with the following abbreviations:

$$W_{\mathrm{shf}} = a + b(3\cos^2\theta - 1) + b' \sin^2\theta \cos 2\delta \tag{25}$$

$$W_Q = 3\{q(3\cos^2\theta' - 1) + q' \sin^2\theta' \cos 2\delta'\} \tag{26}$$

θ, δ and θ', δ' are the polar angles of B_0 in the principal superhyperfine and quadrupole axis system, respectively.

$$\nu_n = \frac{1}{h} g_I \mu_n B_0 \tag{27}$$

where ν_n is the Larmor frequency of a free nucleus in the magnetic field B_0.

$$m_q = m_I + m_I' \tag{28}$$

where m_q is the average between the two nuclear spin quantum numbers, which are connected by the transition [16].

The basic concepts for the analysis of ENDOR spectra is described assuming that (24) holds for the frequency positions of the ENDOR lines. This is generally not the case, since both the anisotropic and quadrupole interactions can become

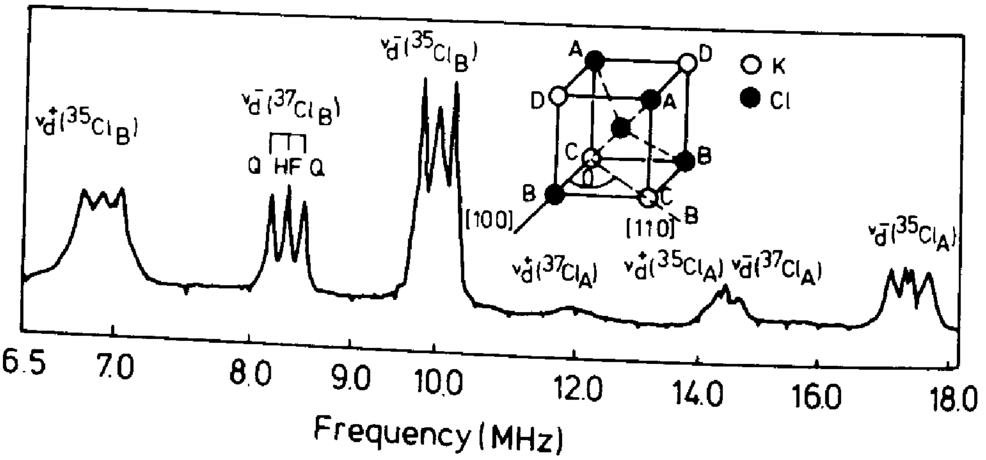

Figure 6.15 The ENDOR spectrum of nearest halogen neighbors of interstitial atomic hydrogen centers in KCl. $B_0 \| \langle 110 \rangle$. Reprinted with permission from J.-M. Spaeth, "Atomic Hydrogen as a Model Defect in Alkali Halides," in V. M. Tuchkevich and K. K. Shvarts, Eds., *Defects in Insulating Crystals*, Springer, New York, 1981, p. 232.

too large with respect to the isotropic term and g-anisotropies, and the fine-structure interaction can influence the spectra. A detailed discussion of the complications is beyond the scope of this chapter. Some particularly important consequences of higher order contributions to the frequency positions will, however, be discussed where appropriate.

Figure 6.15 shows an ENDOR spectrum of interstitial atomic hydrogen in KCl for $B_0 \| \langle 110 \rangle$, the ESR spectrum of which is shown in Figure 6.10*a* [for $B_0 \| \langle 100 \rangle$]. The ENDOR spectrum contains the interaction with the nearest Cl neighbors [15]. The identification of the chemical nature of nuclei can be achieved in various ways. According to (24), for $S = \frac{1}{2}$ and no quadrupole interactions, each nucleus gives a pair of lines separated by $2\nu_n$ if $\frac{1}{2}W_{\mathrm{shf}} > h\nu_n$ and by W_{shf} if $h\nu_n > \frac{1}{2}W_{\mathrm{shf}}$. Since ν_n can be calculated according to (27), the nuclei can be identified either from the line pairs separated by $2\nu_n$ or by symmetric line patterns about ν_n.

If there are several magnetic isotopes present (as ^{37}Cl and ^{35}Cl in Figure 6.15), then their line positions must be in the ratio of their respective nuclear moments (if $Q = 0$). The line intensity roughly reflects the isotope abundance. Unfortunately, the ENDOR line intensity is very little understood quantitatively in solids because of the many and complicated relaxation paths. Therefore, according to (24) the two lines of each nucleus cannot always be observed, particularly for low frequencies in stationary ENDOR. However, upon shifting the magnetic field through the ESR line the ENDOR line positions are also shifted according to (24) and (27). The ENDOR line shift is caused by the shift of ν_n and is thus proportional to g_I, which is characteristic for a particular nucleus. If the ESR line width is too small to detect an ENDOR line shift (which depends on the ENDOR line width), then one can either perform additional experiments with a different ESR band (e.g., K band or Q band) or change the resonant frequency of the cavity by inserting a material of suitable dielectric constant and changing the microwave source frequency accordingly.

If there is a quadrupole splitting, then each *hyperfine* ENDOR line is split into a characteristic multiplet; for example, for $I = \frac{3}{2}$ it is split into a triplet. This is easily recognized in Figure 6.15 as a triplet structure of each ENDOR line. The additional structure indicated in the ENDOR lines is due to second-order superhyperfine structure [14].

To determine the defect structure and the interaction parameters, the dependence of the ENDOR line positions on variation of the magnetic field with respect to the crystal orientation must be measured and analyzed. This is the major problem in an ENDOR analysis and the essential tool for the determination of the defect structure.

Figures 6.16*a–c* show such an angular dependence for a cubic crystal, such as an alkali halide, calculated according to (24) for the first three neighbor shells of a defect on a lattice site. The patterns are characteristic for (100), (110), and (111) *symmetry* of the neighbor nuclei. For each m_s value such a pattern is observed. From the number of such patterns according to (24) one can infer the electron spin of the defect and thus often its charge state.

Each nucleus has its own principal axis system for the superhyperfine and quadrupole tensors. Often, their orientation in a crystal is determined by symmetry. Otherwise, they must be determined from the analysis of the angular dependence of the ENDOR spectra. If the defect center (impurity) and the respective nucleus are in a mirror plane, then two principal axes must be in this mirror plane. If the connection line between the nucleus and the center is a threefold or higher symmetry axis, then the tensor is axially symmetric with its axis along this symmetry axis.

If the angular patterns are separated in frequency, they are easily recognized and the analysis is fairly straightforward.

Figure 6.17 shows such an angular dependence for substitutional Te^+ in Si (see Figure 6.8 for the ESR spectrum). In practice, one proceeds as follows: Assume a center model and then calculate the expected angular dependence according to the appropriate spin Hamiltonian making use of the symmetry properties of the assumed model. Comparison with the experimental angular dependence then verifies or falsifies the assumption. If the first-order solution of the spin Hamiltonian is not sufficient, the symmetry patterns of the neighbor shells may not be easily recognized. For the tetrahedral symmetry of a substitutional point defect in a diamond lattice or zincblende lattice the superhyperfine interactions of nearest neighbors should give the simple pattern of Figure 6.18*a*. If $I = \frac{3}{2}$ for the nearest neighbors and a small quadrupole interaction is present, the pattern looks like Figure 6.18*b*, where the quadrupole triplet splitting of the ENDOR lines is easily recognized. However, for larger values of the quadrupole interaction constant q after diagonalization of the spin Hamiltonian the pattern changes considerably (Figure 6.18*c*) and its origin is not so easily recognized. This complication through quadrupole interactions often makes the analysis difficult.

A diamond or zincblende structure (silicon or III–V compounds) presents the particular difficulty that the symmetry of the substitutional site and tetrahedral

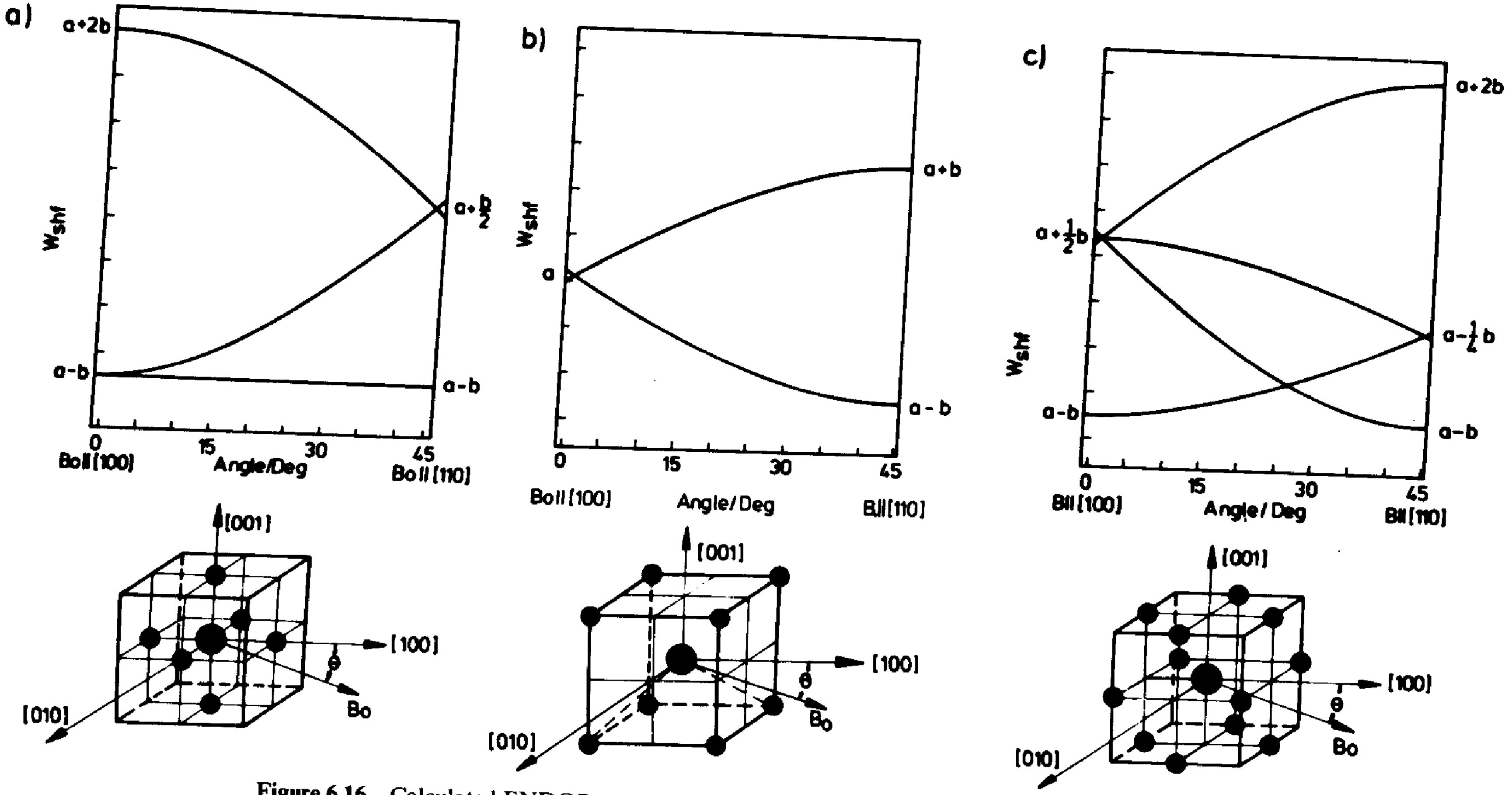

Figure 6.16 Calculated ENDOR angular dependence for a defect on a cation substitutional site in an alkali halide. (*a*) (100) neighbors (anions), (*b*) (111) neighbors (anions), (*c*) (110) neighbors (cations). The magnetic field is rotated in the (001) plane.

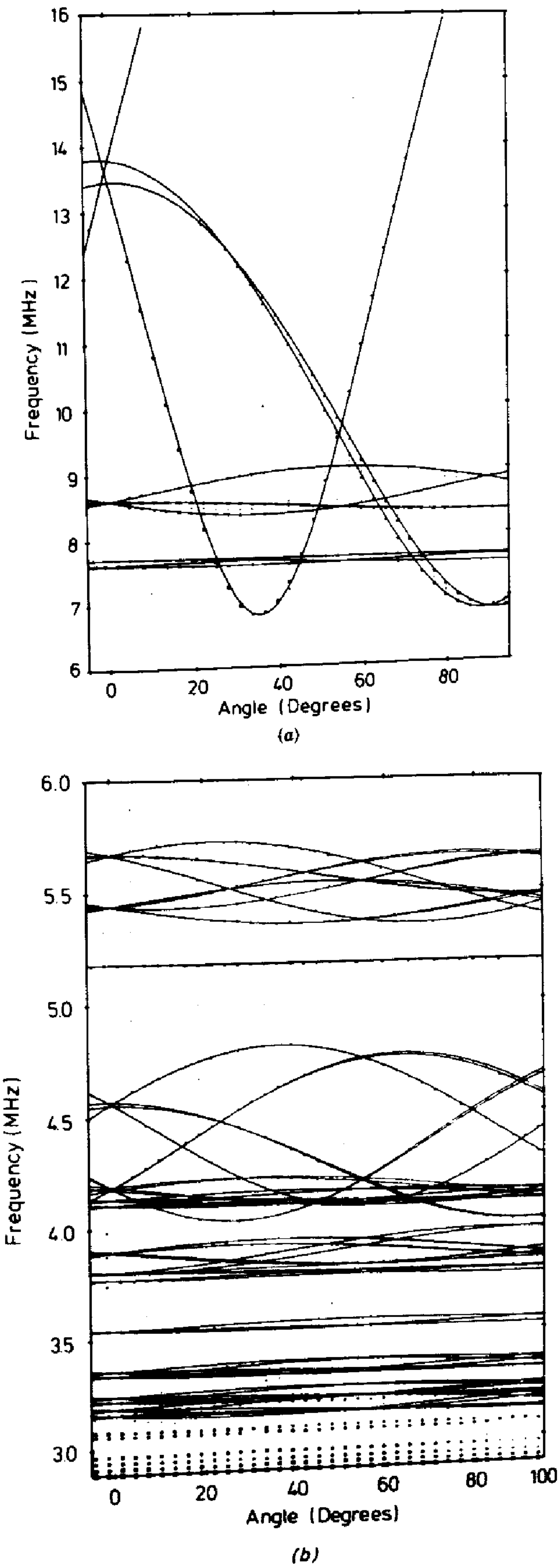

Figure 6.17 Angular dependence of ^{29}Si ENDOR lines of Te$^+$ defects in Si for rotation of the magnetic field in a (110) plane; 0° = ⟨100⟩. The solid lines are the calculated angular dependencies with the parameters of Table 6.4. Reprinted with permission from *Solid State Commun.*, **46**, J. R. Niklas and J.-M. Spaeth, "ENDOR Investigation of Tellurium Donors in Silicon," Copyright 1983, Pergamon Journals, Ltd.

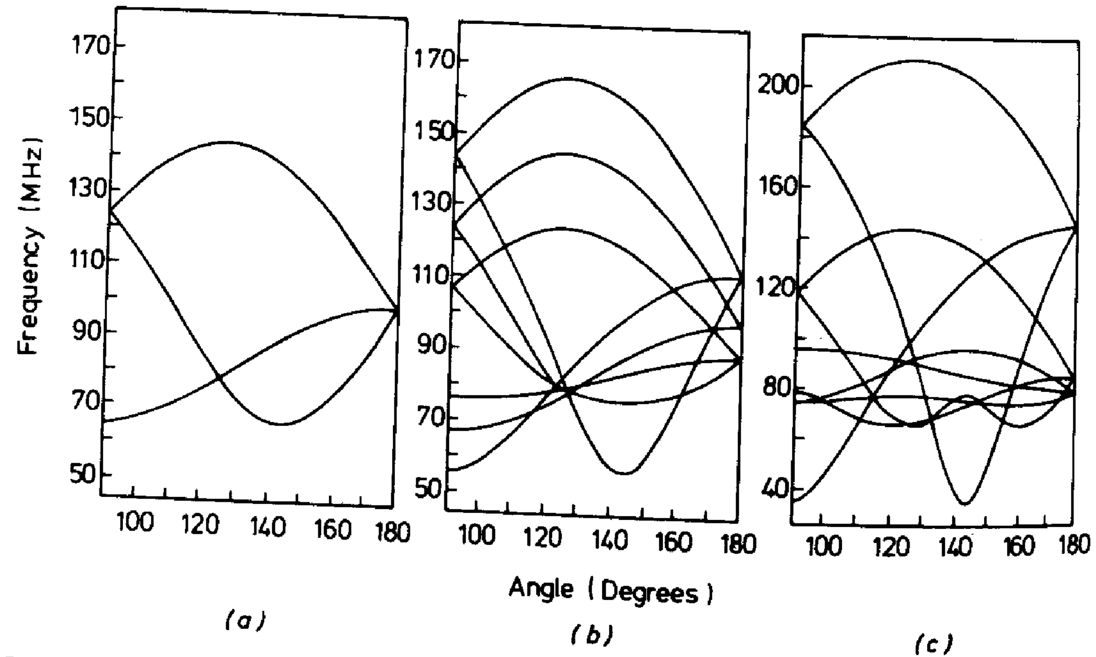

(a) (b) (c)

Figure 6.18 Calculated ENDOR angular dependence of an assumed $AsAs_4$ antisite defect in GaAs due to four equivalent nearest ^{75}As neighbors for $m_s = -\frac{1}{2}$ and rotation of the crystal in a (110) plane from $\langle 110 \rangle = 90°$ to $\langle 100 \rangle = 180°$. The simulation is for the following ligand hyperfine and quadrupole constants (tensor axes $\parallel \langle 111 \rangle$ directions): (*a*) $a/h = 198$ MHZ, $b/h = 53$ MHz, $q/h = 0$; (*b*) $a/h = 198$ MHz, $b/h = 53$ MHz, $q/h = 3.5$ MHz; (*c*) $a/h = 198$ MHz, $b/h = 53$ MHz, $q/h = 11.1$ MHz.

interstitial site cannot be distinguished as to the symmetry type of neighbor nuclei with respect to both defects. There are neighbors with (100), (110), and (111) symmetry of their tensors; however, only the sequence is different on both cases. From experiment only the symmetry type of nuclei can be determined, not the distance of the nuclei from the defect core. Here theoretical arguments about the site of the defect or the character of the wave function must be considered before a definite model is established.

If the agreement between the calculated angular dependence and the experimental one is good, the analysis is unambiguously correct. There are many more experimental data than parameters to be extracted from them. As an example of the result of such an analysis Table 6.3 gives the superhyperfine and quadrupole interaction constants of atomic hydrogen on anion sites in KCl ($H^0_{s,}$ centers) [15]. The analysis unambiguously determines the site for the hydrogen atom from the symmetry of the neighbor nuclei. The superhyperfine and quadrupole interaction constants can be determined down to very small interactions with high precision. The spin Hamiltonian had to be diagonalized numerically [15, 17]. Another example is Te^+ in Si (Table 6.4). Here the sequence of Si neighbors is classified according to their symmetry types. Again, only theoretical arguments lead finally to an unambiguous assignment of the Te^+ to the substitutional site [18, 19].

In a straight ENDOR analysis only the relative signs of the superhyperfine constants *a*, *b*, *b′* can be determined. The signs of the quadrupole interaction

Table 6.3 Superhyperfine and Quadrupole Constants of $H^0_{s,a}$ Centers in KCl (in kHz) ($T = 40$ K)[a]

Shell[b]	*Constant*	$H^0_{s,a}$
$^{39}K^{I}$	a	253
	b	219
	q	198
$^{35}Cl^{II}$	a	57
	b	312
	b'	-3
	q	-88
	q'	-94
$^{35}Cl^{IV}$	a	37
	b	54
	q	± 45
$^{39}K^{V}$	a	4
	b	11
	b'	ca. 0
	ϕ_B	$26.0^0 \pm 0.2^0$
	q	± 39
	q'	± 17
	ϕ_Q	$13.5^0 \pm 0.2^0$

[a] Adapted from G. Heder, J. R. Niklas, and J.-M. Spaeth, *Phys. Status Solidi B*, **100**, 567 (1980).

[b] The Roman numeral superscripts denote the shell numbers. They are the sums of the squares of the Miller indices to describe the position of the nuclei with the defect at the center (000).

constants with respect to the superhyperfine interaction constants cannot be determined either. With ENDOR-induced ESR and double-ENDOR more about the signs of the interactions can be extracted from experiment.

In solids a particular situation is met when there are superhyperfine (and quadrupole) interactions with several neighbor nuclei that have exactly the same interactions and tensor orientations with respect to the magnetic field orientation B_0; in this case the nuclei are precisely equivalent. An additional line splitting can occur, which can be very confusing if it is not recognized as such (second-order superhyperfine splitting). The splitting pattern can be quite complicated. If there is only an isotropic superhyperfine interaction (or $b \ll a$), then the splitting between the ENDOR lines is about $a^2/2g_e\mu_B B_0$. For small interaction constants it is hardly visible, but it is clearly visible for large

Table 6.4 Superhyperfine Interactions of the Te$^+$ and S$^+$ Centers With ^{29}Si[a,b]

	Si:Te$^+$				Si:S$^+$	
Type	*a*/MHz	*b*/MHz	*b'*/MHz	θ_{shf}[c]	*a*/MHz	*b*/MHz
111	17.7	9.8			32.7	12.0
	11.4	0.47			9.0	0.62
	1.3	0.03			2.94	0.02
					1.35	0.09
100	4.6	<0.005	<0.005		2.04	0.05
	1.8	0.02	<0.005			
110	2.83	0.51	−0.08	53.1	8.94	0.47
	5.26	0.21	0.12	67.1	3.84	0.42
	9.52	−0.09	−0.03	0	4.77	0.03
	1.95	0.1	0.02	−5		
	2.46	0.04	<0.005	50.9		
	0.9	0.04	<0.005	47.6		
	0.67	0.04	−0.01	47.2		

[a] Adapted with permission from *Solid State Communications*, **46**, J. R. Niklas and J.-M. Spaeth, "ENDOR Investigation of Tellurium Donors in Silicon," Copyright © 1983, Pergamon Press PLC.
[b] Experimental error is about ±0.1 MHz.
[c] θ_{shf} is given with respect to a ⟨110⟩ axis.

interactions (for $a/h = 100$ MHz, the splitting is about 500 kHz in X band) [20]. In particular, if b and q are not small with respect to a, rather large splittings and a complicated pattern can occur. A recent example shows this in the ENDOR spectrum for the Ga vacancy in GaP (Figure 6.19). For the particular orientation of $B_0 \parallel [111]$ one would expect without this superhyperfine structure of second order only four ENDOR lines due to the four nearest ^{31}P neighbors, since for each m_s value B_0 is parallel to the superhyperfine axes of one neighbor, the other three nuclei have the same angle with respect to B_0, thus yielding only two ENDOR lines for each value. In the frequency range of Figure 6.19 there should be only two lines observed because of the four equivalent ^{31}P neighbors for $m_s = \pm\frac{3}{2}$. However, there are nine lines observed with large splittings of the order of several megahertz. Initially, whether the vacancy is distorted was unclear. The distortion can also give rise to splittings. However, double-ENDOR experiments showed that this splitting is caused by the second-order superhyperfine structure. A full diagonalization of the spin Hamiltonian for the case of four equivalent nuclei confirmed that the splitting is caused by the second-order effects [21].

In practice, another fact renders the ENDOR analysis rather difficult. If there are many lines caused by one defect within a narrow frequency range, as for the atomic hydrogen centers on anion sites, then an analysis is only feasible by employing computer-aided methods. Figure 6.20*a* shows the angular de-

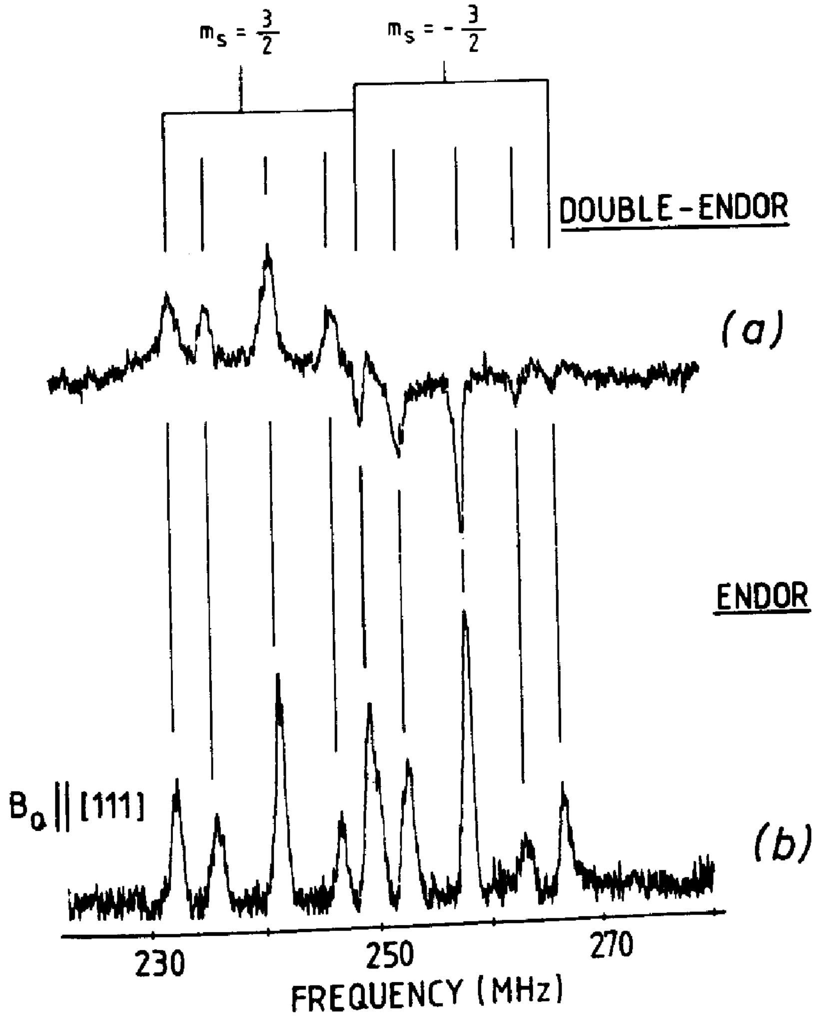

Figure 6.19 (*a*) Double-ENDOR lines. (*b*) ENDOR lines of ^{31}P nearest neighbors of the gallium vacancy (V_{Ga}) in GaP. B_0 approximately parallel to [111]. Reprinted with permission from J. Hage, J. R. Niklas, and J.-M. Spaeth, *Mater. Sci. Forum*, **10–12**, 259 (1986).

pendence of these centers. Another example is that of Ni^{3+} in GaP, where for each magnetic field orientation over 600 ENDOR lines were observed [22]. The angular pattern can also become complicated because of the many center orientations of low-symmetry defects and because the angular dependence must be described by a complete diagonalization of the spin Hamiltonian. The result of this for hydrogen centers is shown in Figure 6.20*b* using the superhyperfine and quadrupole constants of Table 6.3.

Hence, with conventional ENDOR spectrometers only comparatively simple problems can be solved. In complicated cases the angular dependence must be measured in small angular steps, and because of a low signal-to-noise (S/N) ratio observed the experiments must be repeated many times. In recent years considerable progress was made by setting up computer-controlled ENDOR spectrometers and by using computers for the data processing and analysis of the spectra.

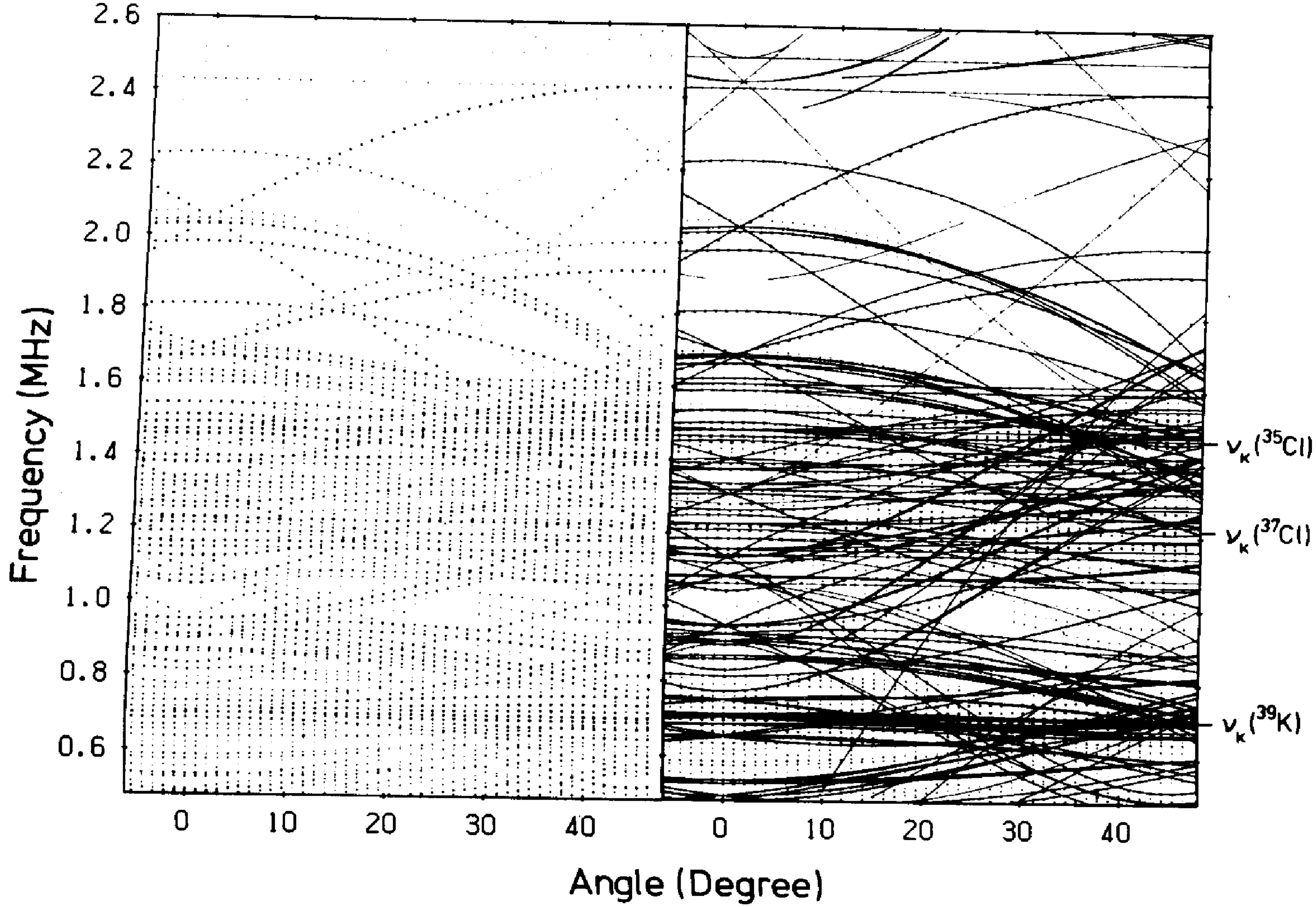

Figure 6.20 Angular dependence of the ENDOR lines of atomic hydrogen centers on anion sites in KCl for rotation of the magnetic field in a (100) plane between ⟨100⟩ (0°) and ⟨110⟩ (45°). Left: experimental results. Right: calculated angular dependence with the superhyperfine and quadrupole constants given in Table 6.3. Reprinted with permission from G. Heder, J. R. Niklas, and J.-M. Spaeth, *Phys. Status Solidi B*, **100**, 567 (1980).

4.3 Experimental Aspects

Observation of a stationary ENDOR effect from solid-state defects depends mainly on two essential parts of the spectrometer: (1) a suitable ENDOR cavity, which allows the generation of a strong enough radio frequency amplitude B_2 without unduly affecting the quality factor Q of the cavity, since the microwave amplitude B_1 must be high enough to partially saturate the ESR signal; (2) a cryosystem, which allows one to vary the sample temperature in a wide range, preferably between 1.5 K and room temperature. If the radio frequency field is produced by a coil, in which radio frequency current flows, one needs a TM-mode cavity [23, 24]. A particularly useful cavity construction is that of Figure 6.21, where the radio frequency current flows through solid rods in a TE_{011} resonator [25, 26]. The sample temperature must be varied in a wide range because to observe the stationary ENDOR effect the electron spin–lattice relaxation rate $1/T_1$, the electron cross-relaxation rate $1/T_x$, and the microwave-transition rate must all be of the same order of magnitude and they must be in certain relations with respect to each other. Since there is a complex relaxation scheme in solids, the optimum experimental conditions cannot be predicted. The best approach is to be able to vary both microwave power and temperature and

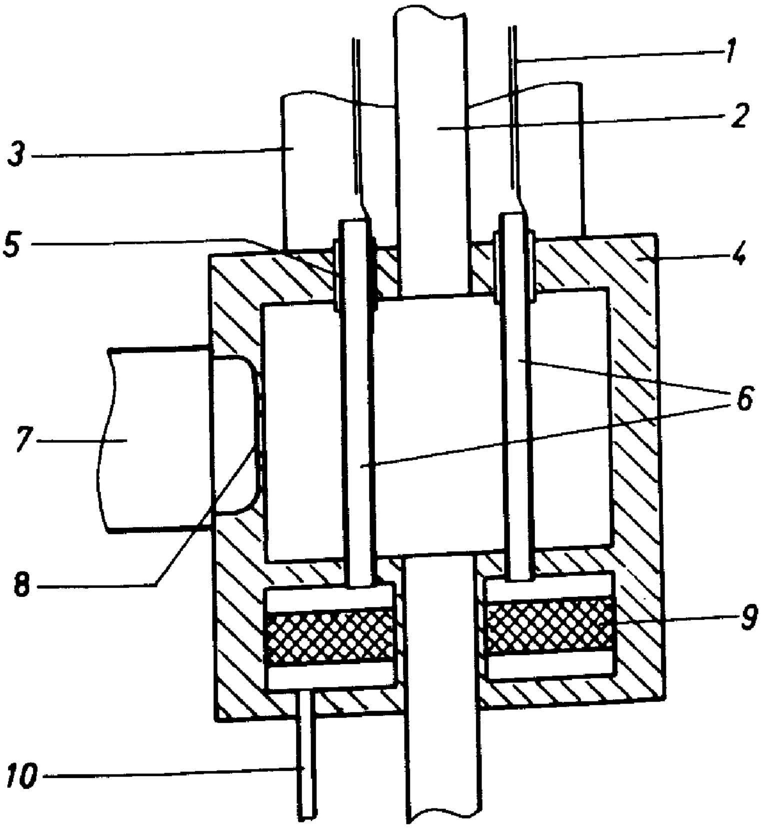

Figure 6.21 The ESR–ENDOR resonator for variable temperature measurements between 3 and 300 K. The cylindrical resonator works in the TE_{011} mode: (1) radio frequency connection, (2) tube to insert sample, (3) tube for helium exhaust gas, (4) resonator wall, (5) Teflon insulating rings, (6) four silver tubes, (7) microwave guides, (8) iris, (9) heat exchange, (10) liquid helium supply.

to find experimentally the optimum conditions. Experience teaches us that ENDOR measurements are often possible only in a very narrow temperature range. The temperature must be neither too high nor too low, and this temperature range varies with the defect system. As a general rule, *s*-type electron ground states require higher temperatures (typically 30–70 K), and *p*-type ground states (hole centers, acceptors in semiconductors) require rather low temperatures. The unavailability of suitable cavity–cryostat combinations for solid-state investigations is the most serious deficiency of commercial ENDOR spectrometers.

At low temperatures the nuclear spin–lattice relaxation times are long; hence, one cannot use fast modulation of the radio frequency fields. Therefore, it was suggested that superheterodyne spectrometers be built that were also sensitive for low-modulation frequencies (20–1000 Hz). However, low-noise microwave amplifiers are available and were used to preamplify the signal before the microwave diode, and this proved to be approximately as sensitive as a superheterodyne setup with the advantage of being able to use the more simple and carefree homodyne spectrometers [27].

In practical cases of interest many ENDOR lines appear, and the angular dependence of the ENDOR lines must be measured in small angular steps, which means taking continuous measurements for several weeks. This procedure required computer-aided techniques, for both the experiment and the analysis of the spectra.

In the computer-controlled ENDOR spectrometer the computer controls the following experimental parameters: radio frequency (NMR frequencies), magnetic field, crystal orientation, sample temperature, and cavity matching. Thus, the angular dependence can be measured automatically, also as a function of temperature. A full angular dependence can take up to several weeks of continuous measurement. The ENDOR lines are stored in the computer and with a specially developed software their positions can be determined automatically and a computer plot (see Figure 6.20*a*) of the angular dependence can be made.

The application of digital methods to the processing of the experimental data is summarized in Figure 6.22 for the example of interstitial Fe^0 centers in Si [28]. Figure 6.22*a* shows the ENDOR lines of interest between 6 and 8 MHz, which are very weak compared to those from the *distant ENDOR* that are caused by the ^{29}Si nuclei with very low interaction and strong background signal. The latter and the distant ENDOR must be subtracted to deal more clearly with the lines of interest. With a special algorithm the background is subtracted. The algorithm does not assume a particular form of the background. It *eliminates* the sharp peaks from the rest, which then is subtracted from the total spectrum [26, 29]. The resulting spectrum is that of Figure 6.22*c*, which contains several ENDOR lines and, of course, noise. The S/N ratio of ENDOR spectra is usually not too good. The ENDOR effect in solid-state defects is mostly below 1% of the ESR signal. Low defect concentration and the limited ENDOR effect are the major reasons for the poor S/N ratio. Here the use of digital filtering has proved

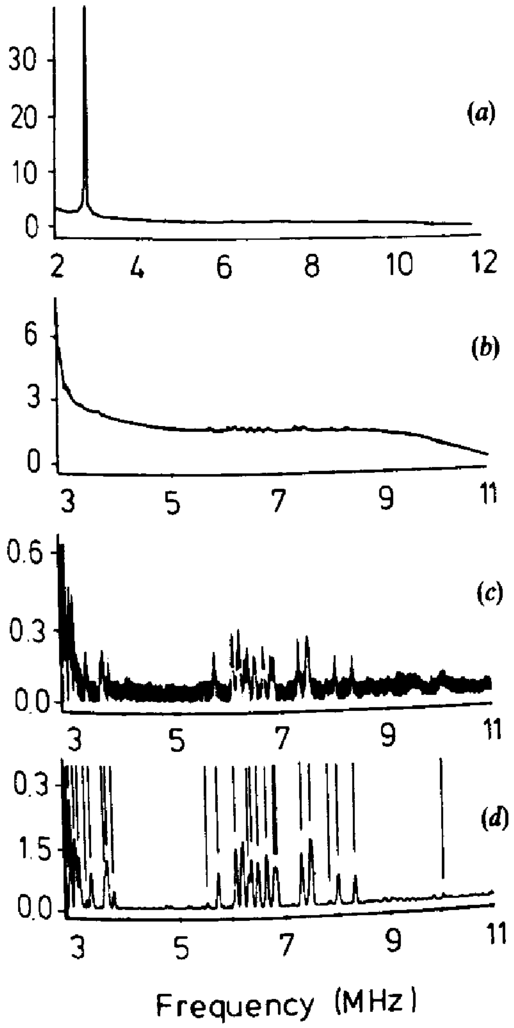

Figure 6.22 Digital data processing for an ENDOR spectrum of interstitial Fe^0 centers in Si: (*a*) spectrum as measured, (*b*) subtraction of the strong ENDOR signal at ν_n (^{29}Si) that is caused by distant nuclei, (*c*) subtraction of a smooth background line, and (*d*) digital filtering and application of the peak search algorithm. Reprinted with permission from S. Greulich-Weber, J. R. Niklas, E. Weber, and J.-M. Spaeth, *Phys. Rev. B*, **30**, 6292 (1984).

to be very advantageous. The major ideas behind this follow. Primarily, one needs to smooth the spectra without disturbing the signals. Conventional resistor capacitor filters give a poor trade-off among noise reduction, signal distortion, and speed of measurement. A simple digital method is a running average algorithm, which replaces a data point by the average of the original data points and its unfiltered left and right neighbor points. This symmetric average over $(2N + 1)$ data points produces the classic noise reduction of any averaging process of uncorrelated data. This idea can be improved by assigning different weights to the neighboring data points.

$$f[K] = \sum_{i=-N}^{N} a[i] \cdot Y[K - i] \qquad (29)$$

Here Y and f denote the unfiltered and the filtered data points, respectively. The weights $a[i]$ describe the digital filter used. For a simple running average one has

$$a[i] = 1/(2N + 1) \qquad (30)$$

If one requests that the filtering process conserves additive constants, linear slopes, parabolic peaks, area, second and third moments, and minimizes noise under these constraints, it can be shown that the weight function

$$a[i] = 3[(3N^2 + 3N - 1) - 5i^2]/[(2N - 1)(2N + 1)(2N + 3)] \qquad (31)$$

is optimal for any line shape [30]. Such a filter is called a *DISPO filter* (digital smoothing with polynomial coefficient) [31]. Compared to a resistor capacitor filter it typically decreases the signal distortion by a factor of 20. For small signal distortion (1%) and equal scan speed this filter reduces noise by an additional factor of 5 compared to the resistor capacitor filter [32, 33].

Figure 6.22*d* shows the application of such a filter to the spectrum of Figure 6.22*c*. The line positions are determined by a special peak-search algorithm, in which the second derivative of the smoothed spectrum is calculated. A peak is resolved where this has a local minimum [26]. This is exact for symmetrical ENDOR lines of Gaussian or Lorentzian shape. The measurement must make sure that the line shape remains symmetrical for this to be applied. Therefore, for this kind of ENDOR spectroscopy, the method of transient ENDOR originally introduced by Feher [1] is not applicable, since in transient ENDOR the line shapes are nonsymmetrical.

When too many ENDOR lines overlap, the application of the peak-search algorithm is not sufficient. An improvement can be reached by applying a deconvolution algorithm, which decomposes the spectra in an iterative process, since the exact shape and width of the single ENDOR lines are not known beforehand.

Figure 6.23*a* shows a section of a spectrum; Figure 6.23*b* is obtained after the application of the deconvolution procedure. In Figure 6.24*a* and *b* the ENDOR angular dependence of $H^0_{s,a}$ centers in KCl, with and without application of the deconvolution, is compared. The advantages of this procedure are clearly visible in the sections between 1.45 and 1.50 and 1.20 and 1.25 MHz. The angular dependence can be followed more efficiently and it can be analyzed. The analysis yields the H^0 atom at the site of the anion vacancy and the values of the superhyperfine and quadrupole interaction constants given in Table 6.3 as an example of typical ENDOR results and their precision. The spin Hamiltonian was diagonalized numerically [15, 17].

4.4 Defect Reactions and Dynamical Effects Studied by Electron Nuclear Double Resonance

Electron nuclear double resonance is not only used to study the structure of defects *given* in a certain crystal, but also to study defect reactions in solids. The transformation of a particular defect into another species can be followed on an atomic microscopic scale.

For example, the conversion of *F* centers in KCl into $F_H(F^-)$ centers by bleaching the optical *F* center absorption band in KCl doped with F^- at a

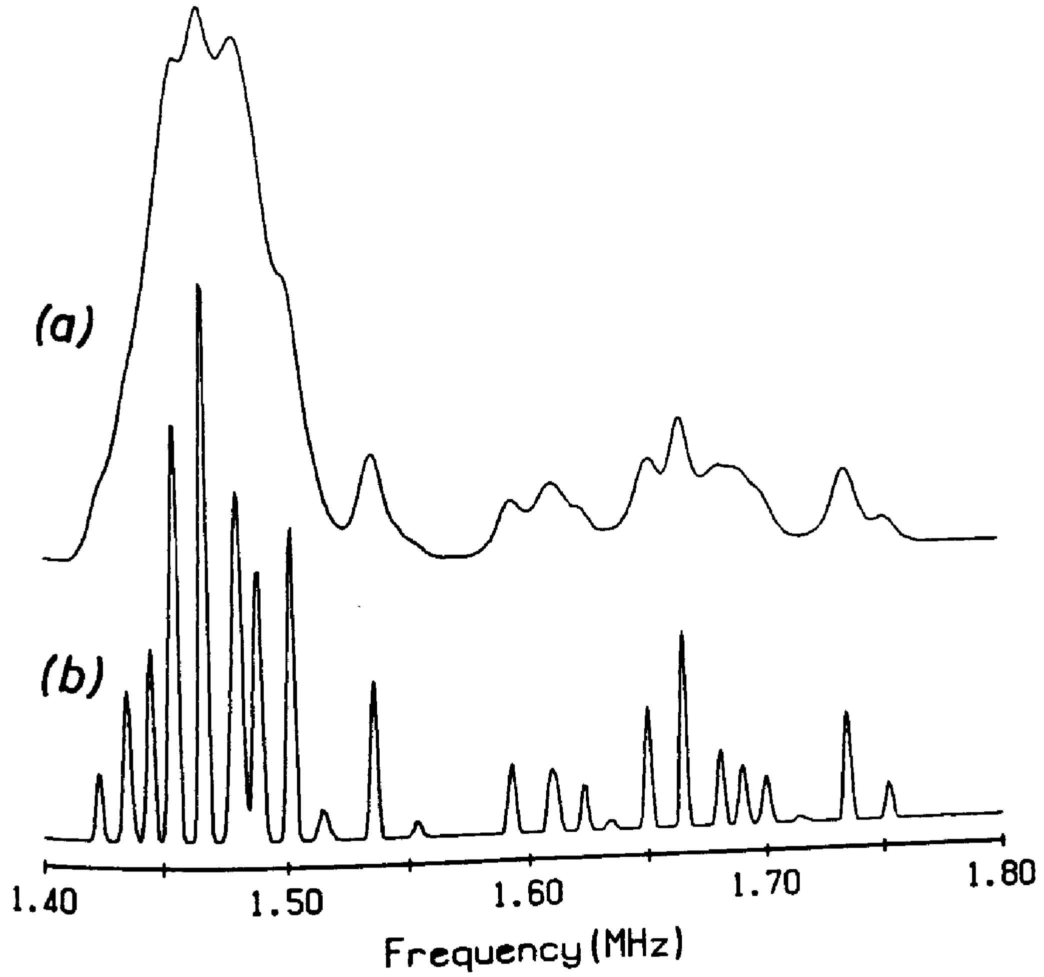

Figure 6.23 Deconvolution of spectra to enhance the resolution of ENDOR: (*a*) spectrum as measured and (*b*) after application of the deconvolution algorithm. Adapted from J. R. Niklas, "Elektronen-Kern-Doppelresonanz-Spektroskopie zur Strukturuntersuchung von Festkörperstörstellen," Habilitationsschrift, Universität-GH-Paderborn, 1983.

temperature where the anion vacancies are mobile is shown in Figure 6.25. The *F* centers in alkali halides are anion vacancies that have trapped an electron; F_H centers are *F* centers aggregated with an impurity halogen ion into an *F* impurity halogen pair center. Thus, $F_H(F^-)$ centers in KCl are Cl^- vacancies with a trapped electron next to F^- impurity halogen. In the lower trace a section of the second shell Cl ENDOR spectrum of the *F* centers before the conversion is shown, above the same section after conversion of about 50% of the *F* centers into $F_H(F^-)$ centers. New ENDOR lines appear between the original ones. In ESR the new centers cannot be distinguished from the *F* centers. Figure 6.26 shows the structure model derived from the analysis of the $F_H(F^-)$ spectrum [34]; F^- occupies a fourth shell position, not a second shell position as may have been assumed. A separation of the ENDOR spectra can be difficult if the "old" spectrum is only partially converted and overlaps strongly the "new" one. There are, however, methods to separate these ENDOR spectra, as will be shown in the Section 5.

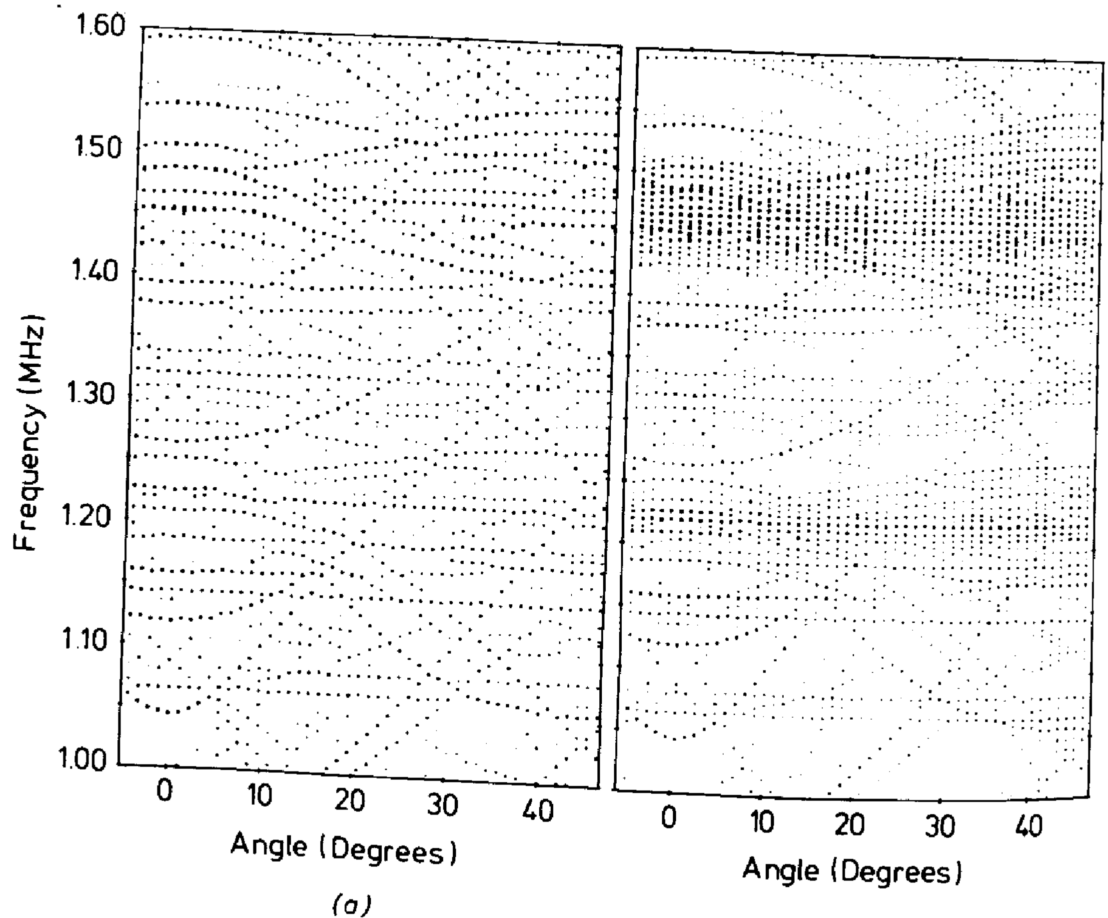

Figure 6.24 (*a*) Section of the ENDOR angular dependence of Figure 6.20 (atomic hydrogen on anion sites in KCl) obtained after digital filtering of the experimental lines and application of the peak-search algorithm. (*b*) The same section after the additional application of the deconvolution algorithm. Adapted from J. R. Niklas, "Elektronen-Kern-Doppelresonanz-Spektroskopie zur Strukturuntersuchung von Festkörperstörstellen," Habilitationsschrift, Universität-GH-Paderborn, 1983.

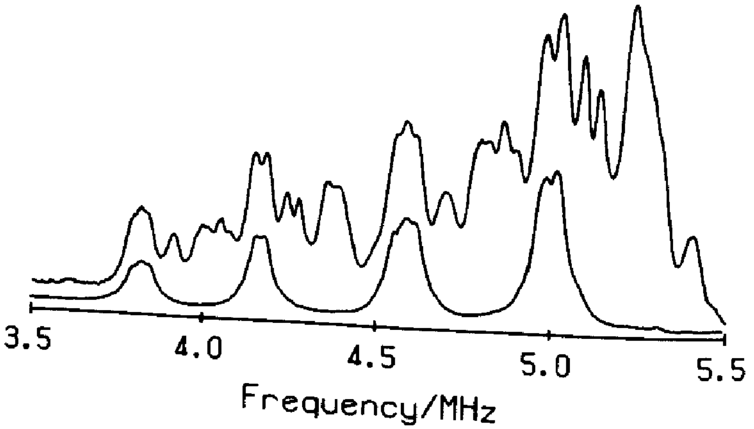

Figure 6.25 Conversion of *F* centers into $F_H(F^-)$ centers in KCl as measured by ENDOR. Lower trace: section of the ENDOR spectrum of *F* centers in KCl:F$^-$ prior to conversion. The lines are caused by second-shell ^{35}Cl and ^{37}Cl neighbors. Upper trace: The same section after conversion of about 50% of the *F* centers into $F_H(F^-)$ centers. The (F$^-$) model is shown in Figure 6.26. Adapted with permission from H. Söthe, P. Studzinski, and J.-M. Spaeth, *Phys. Status Solidi B*, **130**, 339 (1985).

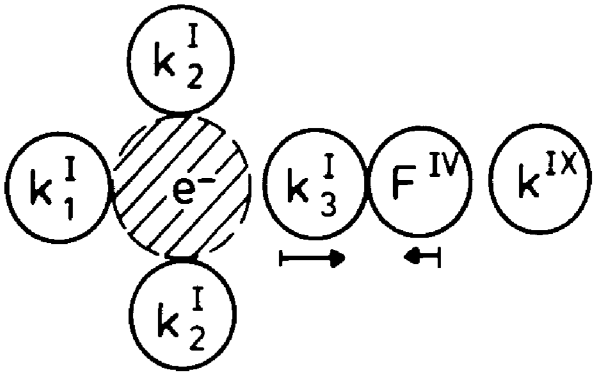

Figure 6.26 Model of the $F_H(F^-)$ centers in KCl as derived from the ENDOR analysis. The superscripts I, IV, and IX are the shell numbers of the neighbor ions. They are the squares of the Miller indices describing the position of the neighbors with respect to the F center at (0, 0, 0).

Another recent example is the formation of thermal donors in silicon (see Section 3), which are electrically active shallow donors. They are formed when Czochralski-grown, oxygen-rich Si (containing $10^{18}\,\mathrm{cm}^{-3}$ interstitial oxygen) is annealed at about 450°C. By their infrared absorption bands they were identified to consist of about nine defects, which grow one after the other starting from an electrically active smallest one by adding atoms to this aggregate center as the annealing time is increased [35].

Interstitial oxygen in Si is not electrically active. Oxygen was thought to be involved in this structure of thermal donors, but it could not be proven. The ESR spectrum of the singly ionized species was already shown in Figure 6.3. By measuring a sample into which the magnetic ^{17}O ($I = \frac{5}{2}$) was diffused [36], ENDOR experiments not only proved the incorporation of oxygen into the thermal donors, but, interestingly for the present discussion, also the way the thermal donors grow. Very decisive results were obtained.

Figure 6.27 shows a section of the ^{29}Si ENDOR spectrum for several annealing times. Five different thermal donors are distinguishable and labeled (A)–(E). They are superimposed in the ESR line (see Figure 6.3), and in the ENDOR spectrum (lowest trace) five species are also present simultaneously. Interestingly, on further annealing only the relative intensities of the ENDOR lines change (Figure 6.27), not their positions; that is, the inner part of the defect structure is not changed when further atoms are added. Since the absolute ENDOR line intensities are not well understood, it is the change of the relative intensities that reflects the change of the numbers of the different thermal donor species upon annealing. The analysis of the angular dependence shows that the superhyperfine tensor orientations are the same for all species; and they are only distinguished by the magnitude of the interaction constants, which decrease upon thermal donor growth. The fact that no symmetries are changed upon growth shows that the growth occurs under full conservation of symmetry; that is, because of C_{2v} the growth must occur under addition of an even number (at least two) of atoms. Thus, ENDOR can make very precise statements about defect reactions, even in such a complicated case as an aggregate center [36, 37].

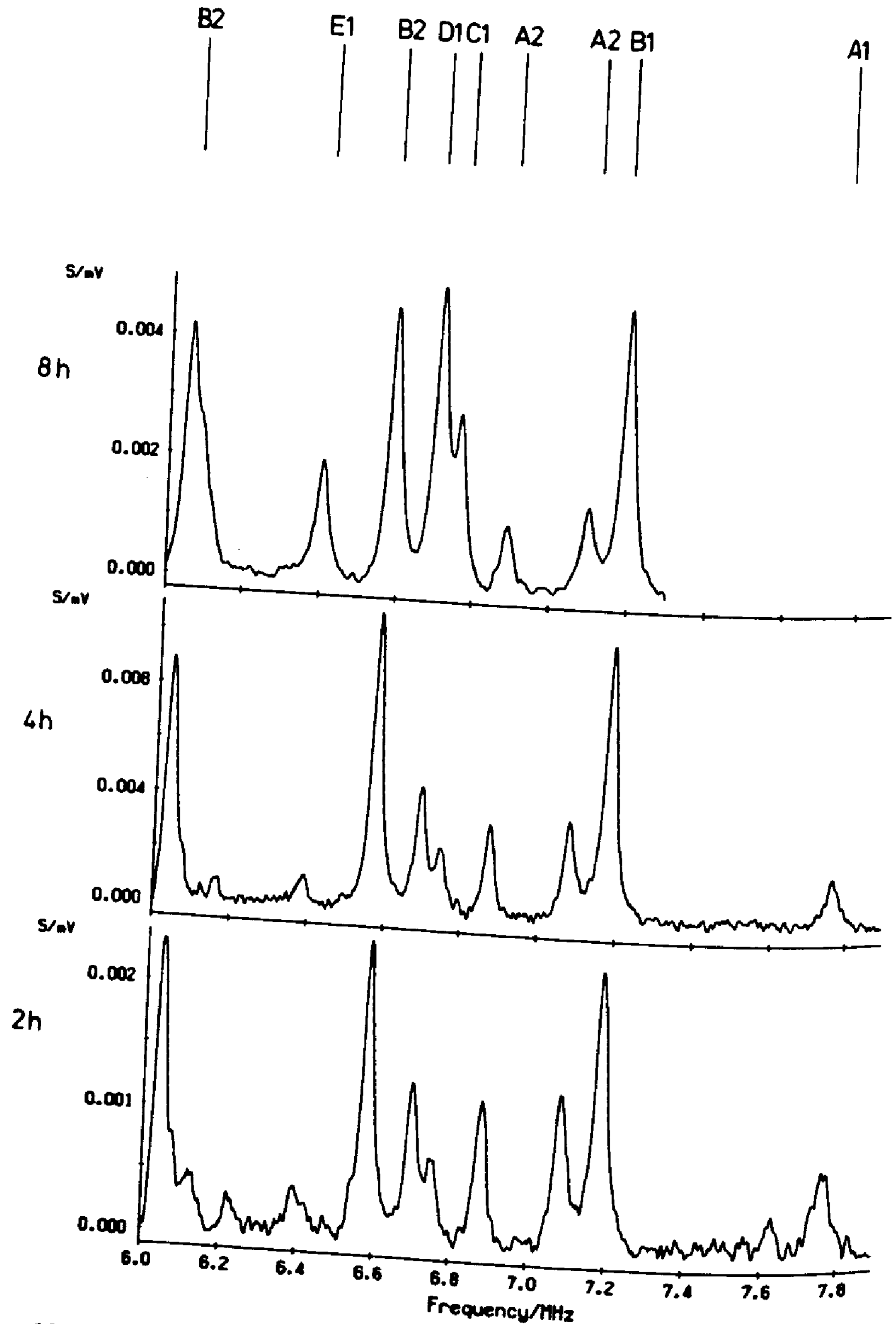

Figure 6.27 Section of the ^{29}Si ENDOR spectrum of thermal donors (NL8) in silicon. Shown is the effect of annealing at 460°C on the ^{29}Si ENDOR spectrum. Upon annealing the relative ENDOR signal intensities change because of the gradual formation of different species of the thermal donors, the ENDOR lines of which are superimposed: (A)–(E) denote the different thermal donors; (1)–(2) are the different ^{29} Si shells. Reprinted with permission from J. Michel, J. R. Niklas, J.-M. Spaeth, and C. Weinert, *Phys. Rev. Lett.*, 57, 611 (1986).

With ENDOR dynamical properties of defects can also be studied by measuring the temperature dependence of the ENDOR line positions. Since each ENDOR line position can be determined with high precision (to 1–10 kHz, depending on the line width), comparatively small effects can also be seen. In Figure 6.28 the temperature dependence of the isotropic superhyperfine interaction constant of K_3^I and F^{IV} neighbors of $F_H(F^-)$ centers (see Figure 6.26) and of the corresponding K^I and Cl^{IV} neighbors in F centers is plotted between 77 and 300 K [38]. The strong temperature dependence of K_3^I of $F_H(F^-)$ centers reflects that K_3^I, which is displaced by 11% toward F^-, has more room compared to K^I in the F center; and it experiences a large local mode vibration, while F^{IV} is knocked farther away through these vibrations.

Another example is the strong temperature dependence of the superhyperfine interaction observed for atomic hydrogen centers on anion or cation sites [14, 39, 40], which have local vibrational modes with very high amplitudes caused by the light hydrogen mass.

In crystals with structural phase transitions the lattice changes its symmetry at T_c. This can be *seen* by a paramagnetic probe, which therefore can be used to study such transitions. A recent example is the investigation of Mn^{2+} in $RbCdF_3$, which goes from a cubic to a tetragonal phase at 124 K. With ENDOR it was possible to study the order parameter as a function of temperature, which is directly reflected in the splitting of the ENDOR lines with temperature on going through T_c for suitable field orientations. It turned out that the order parameter measured is smaller than the intrinsic value, since the lattice relaxes around the probe, and this *decouples* it from the lattice somewhat [41, 42].

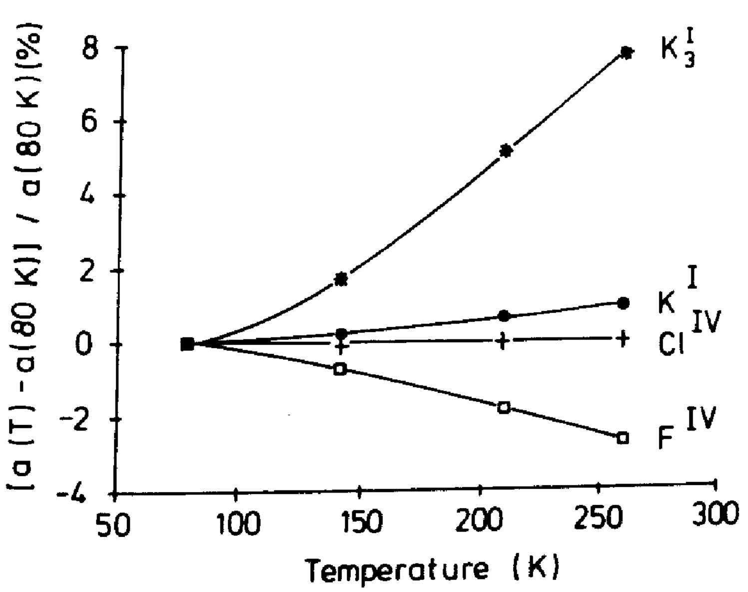

Figure 6.28 Temperature dependence of the isotropic superhyperfine constant a of the K_3^I and F^{IV} neighbors of $F_H(F^-)$ centers in KCl (see Figure 6.26) compared to the corresponding temperature dependence of K^I and Cl^{IV} neighbors of F centers in KCl.

4.5 Photo-Electron Nuclear Double Resonance

Particularly in semiconductor physics a correlation between the determination of a defect structure and other properties, like the energy levels associated with them, is very important to understand and improve the materials. In general, the energy levels are determined by *deep level transient spectroscopy* (DLTS) or related techniques (see, e.g., [43]), which, however, cannot identify the microscopic nature of the defect, while ESR (or) ENDOR alone can only determine the defect structure. A correlation between the energy levels and the defect structure can be achieved by measuring two kinds of crystals: one, where the level of the defects in question is occupied by an unpaired electron and another, where the Fermi energy is lower (e.g., by pinning the Fermi level at shallow impurities) so that the level in question is empty. In the former the ESR-ENDOR analysis is performed. The latter does not show ESR or ENDOR signals unless it is illuminated with light of sufficient energy such that electrons are raised from the valence band to occupy the level. Figure 6.29 shows such a

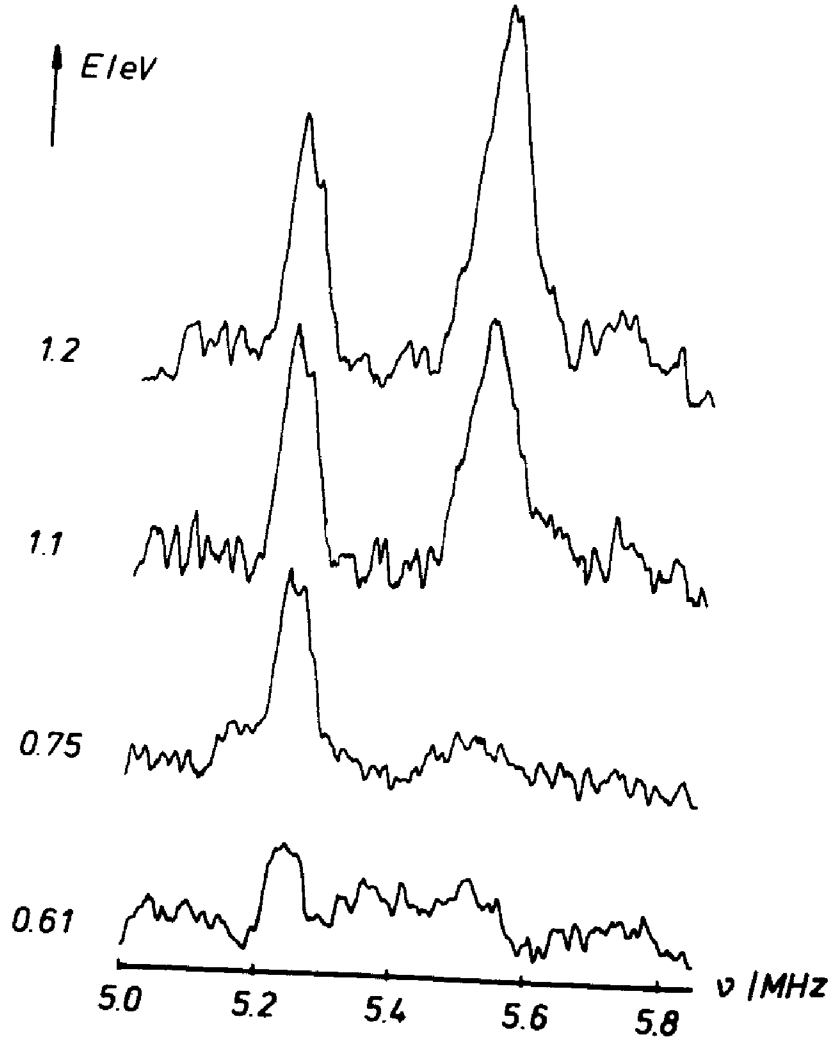

Figure 6.29 Photo-ENDOR of S^+ and $(S—S)^+$ defects in silicon. Adapted from S. Greulich-Weber, "ENDOR-Untersuchungen an Chalkogenen in Silizium," doctoral dissertation, Universität-GH-Paderborn, 1987.

photo-ENDOR experiment in Si doped with S (and codoped with B to lower the Fermi level to be nearer to the valence band). The crystal contained two paramagnetic defects: S^+ and $(S{-}S)^+$ pairs. The ESR-ENDOR signals of S^+ began to appear with light of $h\nu > 0.58$ eV, while those of the $(S{-}S)^+$ pair defects appeared only for $h\nu > 0.8$ eV. In Figure 6.29, for example, at $h\nu = 0.75$ eV, only ENDOR lines of the S^+ appear [44]. The two levels identified at $E_v \pm (0.59 \pm 0.05)$eV and $E_c - (0.37 \pm 0.05)$eV in this way agree well with those determined by optical spectroscopy and DLTS [45]. Apart from the correlation between energy levels and defect structures the method can be used to separate the ENDOR spectra of different defect species, whose spectra overlap in the same frequency range. Their analysis can be very difficult without being able to identify and correlate the ENDOR lines to one particular defect species. Similarly, optical ionization of occupied levels can be used to change the ENDOR line intensity of a specific defect and thus identify its lines from other defect lines present simultaneously. For example, this was applied successfully to the investigation of thermal donors in Si [37].

5 ADVANCED ELECTRON NUCLEAR DOUBLE RESONANCE METHODS

5.1 Electron Nuclear Double Resonance-Induced Electron Spin Resonance

Overlapping ESR spectra of different defects cause overlapping ENDOR spectra. It can be very difficult of not impossible to analyze their angular dependence, especially if many ENDOR lines occur in a narrow frequency range. Furthermore, there may be weaker ESR spectra buried under stronger ones having observable ENDOR lines, which can be analyzed, but the ESR spectrum cannot be measured. The two types of *F* centers possible in BaFCl, for example, are produced simultaneously. Their ESR spectra overlap strongly (see Figure 6.30). Here one can measure a kind of excitation spectrum of a particular ENDOR line that belongs to one defect, which gives an image of the corresponding ESR spectrum that belongs to the same defect (ENDOR-induced ESR spectrum). This can be seen from Figure 6.13. The ENDOR transitions can be measured by setting B_0 to any one of the four superhyperfine ESR transitions for $m_I = \frac{3}{2}, \frac{1}{2}, -\frac{1}{2}$, and $-\frac{3}{2}$; thus the ENDOR line intensity measured should follow the ESR line pattern in the middle of Figure 6.13. However, according to (24), the frequency of an ENDOR line depends on ν_n and hence on B_0. Because of this one must "correct" the ENDOR frequency for the variation of B_0 when varying B_0 through the ESR spectrum. This can be done easily with the computer-controlled spectrometer or in other ways when the corresponding nuclear g_I factor is known. In measuring the ENDOR-induced ESR spectrum one monitors the ENDOR line intensity of a particular ENDOR line while varying the magnetic field through the ESR spectrum and correcting the frequency position according to (24). The resulting spectrum is an image of the

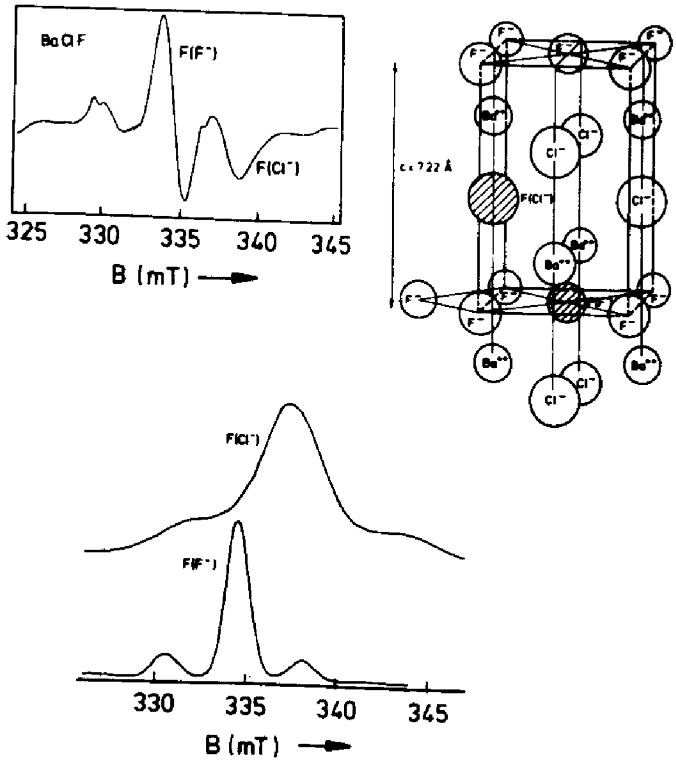

Figure 6.30 Model of two F centers in BaFCl [$F(\mathrm{Cl}^-)$ and $F(\mathrm{F}^-)$ centers], their superimposed ESR spectra (derivative), and the ENDOR-induced ESR spectra of both centers measured using a ^{19}F ENDOR line of each center. Reprinted with permission from J. R. Niklas, R. U. Bauer, and J.-M. Spaeth, *Phys. Status Solidi B*, **119**, 171 (1983).

(integrated) ESR spectrum of that defect, to which the ENDOR line (nucleus) belongs. In this way the ESR spectrum of different defects can be separated.

Figure 6.30 shows this for the two F centers in BaFCl. The two ENDOR-induced ESR spectra were measured using ^{19}F ENDOR lines of both centers. When $S = \frac{1}{2}$ and no quadrupole interaction is experienced by the nucleus, the ENDOR-induced ESR spectrum corresponds to the true ESR line shape if the cross relaxation does not depend on m_I and is not the dominating electron spin relaxation process. The true line shape was observed in several cases [46].

The line shape of the ENDOR-induced ESR spectrum is not necessarily identical with that of the ESR spectrum. To discuss this let us consider Figure 6.31, where the level scheme for the simplified case $S = \frac{1}{2}$, $I = \frac{3}{2}$, W_{shf} and $W_q > 0$ is assumed. If one uses the ENDOR transitions between levels A and B for the ENDOR-induced ESR experiment, only the two ESR transitions between levels B and C and A and D are affected. For instance, the partially saturated ESR transition D–A is desaturated by the NMR transition A–B. Similarly the ESR transition C–B is experiencing a population change because of the NMR transition A–B. The other two possible ENDOR transitions are not affected. Thus, using any of the three quadrupole ENDOR lines, only for two ESR transitions, the m_I states of which are connected to the ENDOR transition, one fulfills the double resonance condition. They can be seen as an ENDOR-induced ESR spectrum only if the following holds: (1) only the simple type of cross-

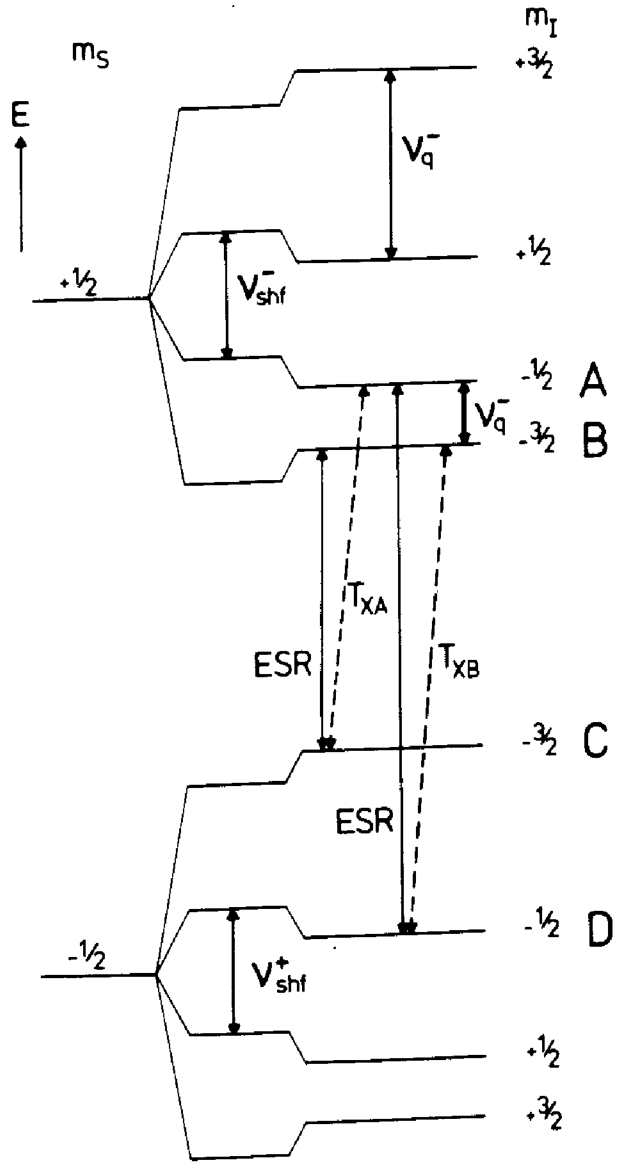

Figure 6.31 Schematic representation of the energy levels for the system $S = \frac{1}{2}$, $I = \frac{3}{2}$ with superhyperfine and quadrupole interactions. The arrows denote ESR–ENDOR and cross-relaxation transitions.

relaxation process $(m_s m_I) \rightarrow (m_s - 1, m_I \pm 1)$ occurs, and (2) no significant relaxation takes place between different m_I states within a given m_s state.

An example of this is shown in Figure 6.32, where the two-line ENDOR-induced ESR spectrum was measured by locking the ENDOR frequencies successively to the three ENDOR lines of the Ba^{2+} quadrupole triplet of $F(Cl^-)$ centers in BaFCl. The assumption seems to hold quite well, although not perfectly, as the small intensity of the two further lines in the ENDOR-induced ESR spectra indicates.

The true line shape of the full ESR spectrum is observed when there is no quadrupole interaction and the relaxation times T_x do not depend on the nuclear spin states.

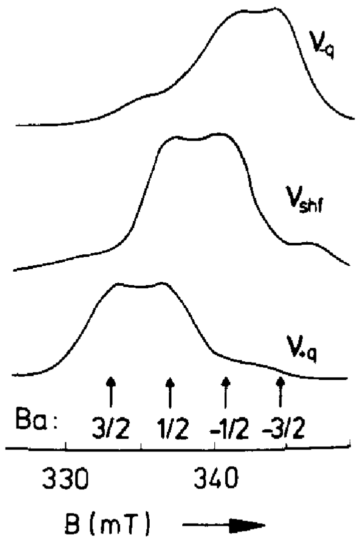

Figure 6.32 An ENDOR-induced ESR spectra of $F(\mathrm{Cl}^-)$ centers in BaFCl using the ^{137}Ba quadrupole triplet ENDOR lines ν_q^-, ν_{shf}, and ν_q^+. Reprinted with permission from J. R. Niklas and J.-M. Spaeth, *Phys. Status Solidi B*, **101**, 221 (1980).

Neglecting isotope mixture, one can apply the preceding arguments for one neighbor also to a nucleus, labeled 1, out of many neighbors, the ENDOR line of which is taken for the ENDOR-induced ESR measurement. Nucleus 1 only experiences another effective magnetic field as in the case of a single neighbor because of the superhyperfine interactions of the other nuclei. To clarify this let us assume that nucleus 1 has the largest superhyperfine interaction. Then the ESR spectrum is split because the W_{shf} of each line is inhomogeneously broadened.

$$B = \frac{1}{g_c \mu_n} h\nu - W_{\mathrm{shf}}^{(1)} \cdot m_I^{(1)} - \sum_{\substack{i=1 \\ i \neq 1}}^{N} W_{\mathrm{shf}}^{(i)} m_I^{(i)} \tag{32}$$

The ESR signal for a given $m_I^{(i)}$ value and particular field B within the $m_I^{(1)}$-superhyperfine line is given by the total number of combinations of the $m_I^{(i)}$ of the other nuclei that lead to this value of B. The line width of the $m_I^{(i)}$-superhyperfine line is determined by the last term in (32).

If nucleus 1 has no quadrupole interaction, the whole ESR spectrum is observed with ENDOR-induced ESR. If nucleus 1 has quadrupole interaction, then only those ESR transitions leading to the two $m_I^{(1)}$ levels that are connected by the ENDOR transition chosen for the experiment are desaturated. Thus, all the lines of the ENDOR-induced ESR spectrum appear at fields B in (32), for which $-I^{(i)} \leqslant m_I^{(i)} \leqslant I^{(i)}, i \neq 1$, and $m_I^{(1)} = \bar{m}_I^{(1)}$ or $m_I^{(1)} = \bar{m}_I^{(1)} + 1$ with $m_I(1)$ having one of the values $-I^{(1)}$, $-I^{(1)} + 1, \cdots, I^{(1)} - 1$ determined by the ENDOR transition chosen. Therefore, if a quadrupole interaction is present, the ENDOR–ESR spectrum is never a true ESR spectrum because of the necessary selection of nuclear spin states.

Figure 6.33 illustrates the ENDOR-induced ESR experiment when a quadrupole ENDOR line ν_{-q}^{+} is taken of a nucleus with a very small superhyperfine interaction (I_2). The superhyperfine splitting of the ESR line is determined by

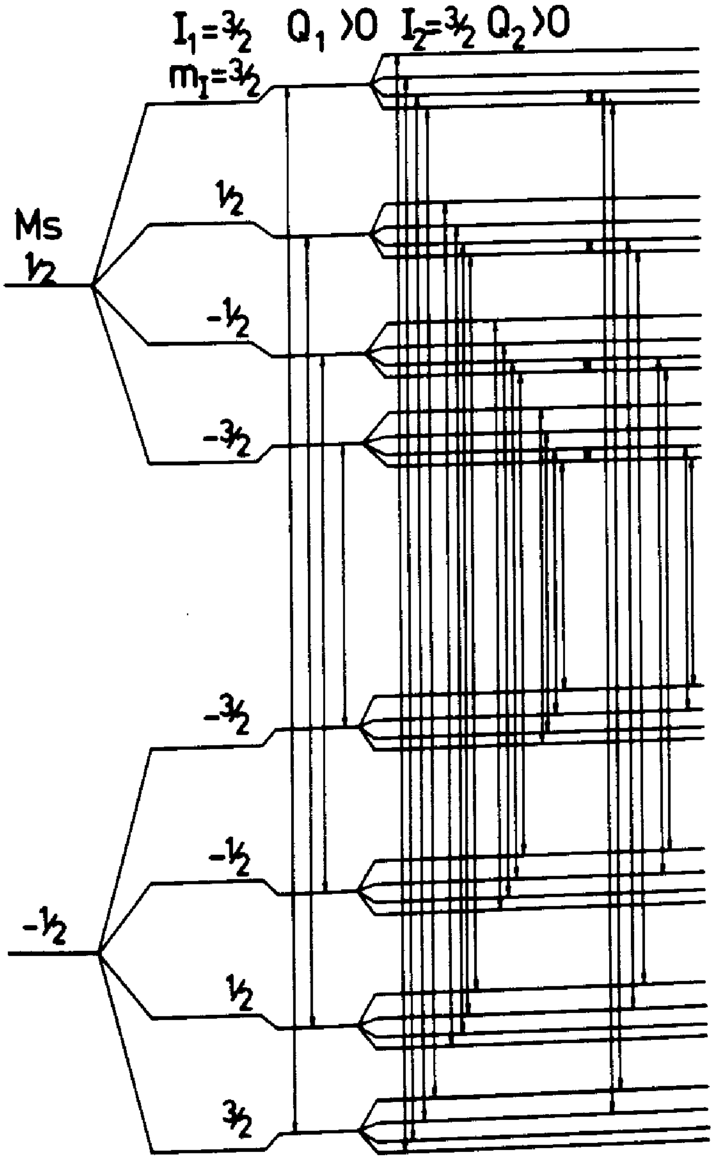

Figure 6.33 Schematic representation of ESR- and ENDOR-induced ESR transitions for a system of one unpaired electron and two nuclei having different superhyperfine and quadrupole interactions. The ENDOR-induced ESR transitions are measured using the nucleus I_2 with the smaller interactions.

another nucleus with a larger interaction (I_1). The ENDOR-induced ESR spectrum represents all superhyperfine lines caused by the larger interaction of I_1 but not the full spectrum, since some lines are missing because of the selection of nuclear spin states of I_2. The line width of the ENDOR-induced ESR lines is smaller, and the whole spectrum is shifted in field. If I_2 has only a very small interaction, then the difference of the ENDOR-induced ESR spectrum and the true ESR spectrum is only small. For details about line width and line position see [46, 47].

The selection of spin states allows one to determine the relative signs of W_q and W_{shf}. Figure 6.31 assumes that both W_{shf} and W_q have the same sign. The observation in Figure 6.32 is explained with the level scheme of Figure 6.31, that is, with the same sign for W_{shf} and W_q.

Certain complications arise when different isotopes are present. Suppose there is only one nucleus with different isotopes, for example, ^{37}Cl and ^{35}Cl, and a superhyperfine-ENDOR line of one isotope is used for ENDOR-induced ESR; then the line shape is not the true ESR line shape. To obtain this, one must add the ENDOR-induced ESR spectra caused by all the corresponding ENDOR lines of the different isotopes to form the total spectrum. The intensity ratio of the different ENDOR-induced ESR spectra should correspond to the abundancy of the different isotopes. If this is not so, then the cross-relaxation rates are different for the isotopes. To obtain the true line shape in this case requires a knowledge of this latter effect to correct the superposition of the isotope ENDOR-induced ESR spectra.

If there are more nuclei of a type with different isotopes, similar arguments apply. One has to add the isotope ENDOR-induced ESR spectra of the nuclei used for the measurement.

More serious complications arise if several strongly coupled nuclei show effects of second-order superhyperfine splitting [20, 21]. One then must work in the total spin representation, and the understanding of the ENDOR-induced ESR spectra is less straightforward. A detailed discussion of this problem is beyond the scope of this chapter. Results we obtained for F^+ centers in Na-β-alumina where two Al nuclei are strongly coupled are described in [48].

For systems with $S > \frac{1}{2}$ there is usually a fine structure interaction splitting of the electron Zeeman levels. In this case with ENDOR-induced ESR one selects spin states in a way analogous to the way one uses to select m_I states because of the quadrupole interaction discussed previously. One measures only some of the possible ESR transition.

This is demonstrated for Fe^{3+} centers in KMgF$_3$, which were produced by X irradiation of KMgF$_3$ doped with Fe^{2+}. In Figure 6.34*a* the integrated ESR spectrum of the five ESR transitions is reproduced with partly resolved superhyperfine structure with six nearest ^{19}F neighbors. Figure 6.34*b* shows the ENDOR-induced ESR spectrum measured with a ^{19}F ENDOR line at 42.5 MHz displaying two of the five Fe^{3+} ESR transitions, while Figure 6.34*c* shows the ENDOR-induced ESR spectrum measured with a ^{19}F ENDOR line at 21.0 MHz. Clearly, another ESR spectrum appears. It was buried under the Fe^{3+} spectrum beyond recognition and turned out to be caused by simultaneously produced *F* centers [49]. A detailed analysis also allows the determination of the relative signs of quadrupole interaction constants, superhyperfine interaction constants, and fine structure constants [46, 47].

5.2 Double-Electron Nuclear Double Resonance

Although with ENDOR-induced ESR experiments each ENDOR line can be *labeled* to a particular defect when there is the simultaneous presence of several defects, this can be a tedious task, especially if one must follow a complicated angular dependence. Therefore, a method is called for with which the ENDOR spectra of different defects can be measured separately. This can be done by

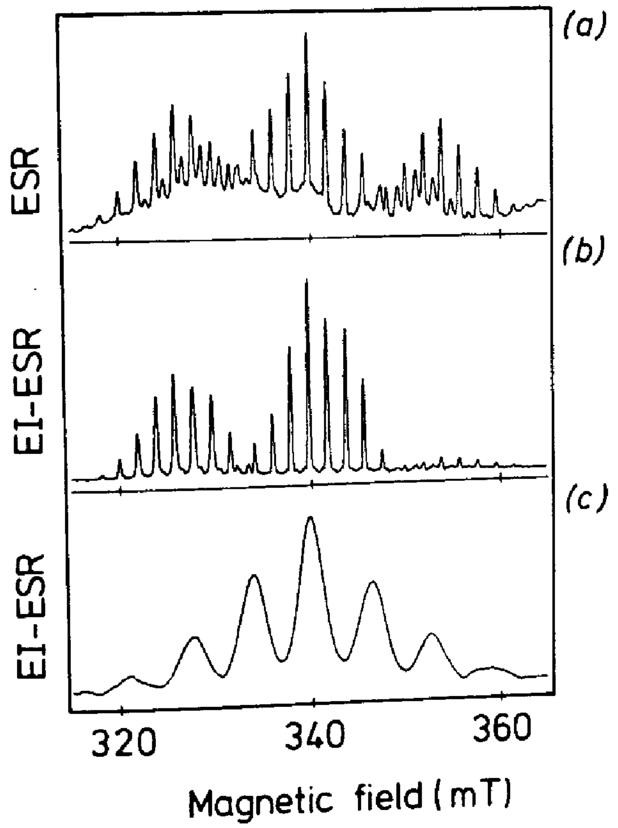

Figure 6.34 The ESR- and ENDOR-induced ESR spectra of X-irradiated $KMgF_3$ doped with Fe^{2+}: (*a*) Integrated ESR spectrum after X irradiation at room temperature. $B_0 \parallel \langle 100 \rangle$. (*b*) The ENDOR-induced ESR spectrum for the ^{19}F-ENDOR lines at 42.5 MHz. The spectrum is caused by Fe^{3+}. (*c*) An ENDOR-induced ESR spectrum for the ^{19}F-ENDOR line at 21.0 MHz. The spectrum is caused by *F* centers. Reprinted with permission from R. C. DuVarney, J. R. Niklas, and J.-M. Spaeth, *Phys. Status Solidi B*, **97**, 135 (1980).

measuring a triple resonance where two NMR frequencies are applied simultaneously together with the microwaves.

In an ENDOR experiment the radio frequency-induced NMR transitions between the nuclear Zeeman levels of a neighbor nucleus coupled to the unpaired electron by a superhyperfine interaction change somewhat the polarization of the electron spin in the partially saturated situation. This coupling between neighbor nucleus and unpaired electron is indicated schematically by a "spring" in Figure 6.35. If a second NMR transition is induced simultaneously with a second radio frequency at another nucleus coupled to the same unpaired electron, then the induced change of the electron spin polarization is different from what it would be if the first NMR transition does not occur simultaneously. Thus, the polarization change caused by the second NMR transition is dependent on the occurrence of the first NMR transition. The total electron desaturation (ENDOR effect) is a function of the product of the effects of the two NMR transitions. Thus, when modulating the two NMR transitions with different frequencies and using double lock-in techniques, one can, for example, induce one particular ENDOR transition of a particular neighbor nucleus and

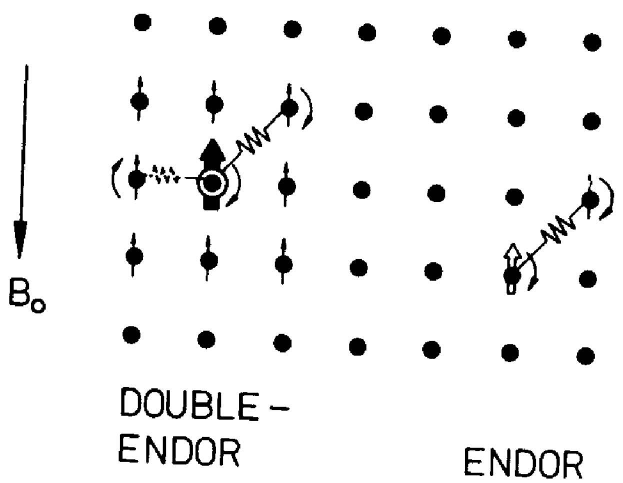

Figure 6.35 Schematic representation of ENDOR and double-ENDOR.

monitor the change of the ENDOR signal height as a function of the simultaneous second ENDOR transition. One observes changes of the NMR line intensity as a function of the second frequency swept radio frequency source. A change is observed when a second ENDOR transition is induced at a nucleus, which is also coupled to the same electron, but not if the nucleus belongs to a different center. The ESR of this different center may also be saturated if the ESR spectra of the different centers overlap. Therefore, this triple resonance experiment can be used to separate the ENDOR spectra of different defects if their ESR spectra overlap. Such a separation may well be impossible otherwise if the centers have many ENDOR lines with complicated angular dependencies. However, the method functions well only when the neighbors have a high abundance of magnetic nuclei. In Si, for example, where only 4.7% nuclei are magnetic (^{29}Si), the probability to have simultaneously two magnetic nuclei as defect neighbors is too low to allow for double-ENDOR experiments.

The simplest experiment, the so-called *special triple resonance* (special double-ENDOR) is shown schematically in Figure 6.36 for the simple case of

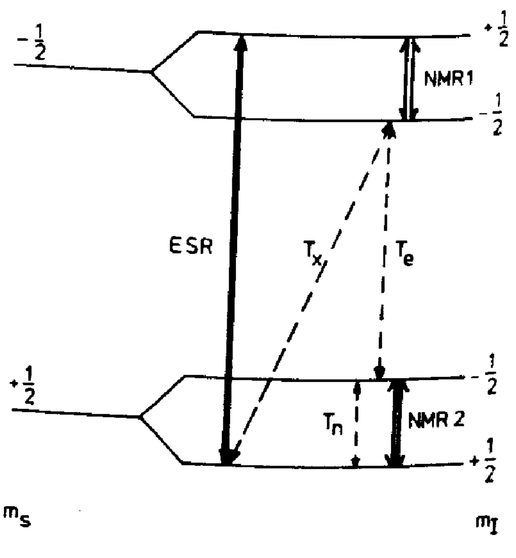

Figure 6.36 Level scheme to explain the special triple-resonance experiments (double-ENDOR).

$S = \frac{1}{2}$, $I = \frac{1}{2}$. If stationary ENDOR is measured for the transition *NMR1* between $m_s = -\frac{1}{2}$, $m_I = \frac{1}{2}$ and $-\frac{1}{2}$, then the signal height is determined by the ESR transition probability (i.e., by B_1^2), the NMR1 transition probability [i.e., B_{rf}^2(NMR1)], and the cross-relaxation time T_x. It is assumed (and a condition for the experiment) that T_x is greater than T_e, the electron spin lattice relaxation time, because of the comparatively long nuclear spin lattice relaxation time T_n. If then a second radio frequency is applied between the levels $m_s = \frac{1}{2}$, $m_I = \frac{1}{2}$ and $-\frac{1}{2}$(NMR2), then T_n is effectively shortened by this transition and therefore T_x is also shortened, which results in an enhancement of the monitored ENDOR signal at the frequency NMR1. In the experiment one irradiates with the fixed ENDOR frequency NMR1, monitors the ENDOR line intensity of the line at NMR1, and sweeps the second radio frequency. When the transition NMR2 is induced the ENDOR line intensity NMR1 increases. The increase is the double-ENDOR signal, and it is detected with a double lock-in technique.

In the stationary double-ENDOR spectrum positive and negative signals are observed [50, 51]. Negative signals occur if the second NMR frequency is induced between nuclear states belonging to the same m_s quantum number. Figure 6.37 shows the double-ENDOR spectrum for the two *F* centers in BaFCl. In Figure 6.37*a* the ENDOR lines of both *F* centers are superimposed; hence, a full analysis was not possible. In Figure 6.37*b* the fixed ENDOR frequency NMR1 was set to one ENDOR line belonging to $F(\mathrm{Cl}^-)$ centers, and NMR2 was swept between 1 and 9 MHz and the double-ENDOR effect was recorded. In Figure 6.37*c* the analogous experiment was made for an $F(\mathrm{F}^-)$ ENDOR line. Both double-ENDOR spectra show only lines caused by the $F(\mathrm{Cl}^-)$ or $F(\mathrm{F}^-)$ centers alone. Especially around 5 MHz both centers have many ENDOR lines, which otherwise could not have been separated [52].

Figure 6.19*a* shows as another example the double-ENDOR spectrum measured for the Ga vacancy in GaP for $B_0 \parallel \langle 111 \rangle$. Comparison of Figure 6.19*a* with Figure 6.14*b* demonstrates that all the lines measured in single ENDOR also appear in double-ENDOR. This proves that all ENDOR lines belong indeed to one defect and that the vacancy is not distorted, with the consequence that the ENDOR spectrum may be a superposition of several vacancy configurations. The occurrence of so many ENDOR lines, at first unexpected for a simple tetrahedral surrounding of four equivalent ^{31}P neighbors, is indeed caused by a large and hitherto undescribed effect of second-order superhyperfine structure [21].

Double-electron nuclear double resonance is also very important when analyzing low-symmetry defects. The defects are distributed over several orientations in the crystal. The ESR and ENDOR spectra of these orientations overlap. In a sense each defect orientation is equivalent to a new defect species. With double-ENDOR the spectra of one particular defect orientation can be measured separately, which greatly facilitates the analysis or makes it possible. In a recent investigation of O^- centers in α-$\mathrm{Al_2O_3}$, which had very low symmetry (that is *no* symmetry), a definite assignment of the quadrupole ENDOR lines to their corresponding ***hyperfine*** ENDOR lines was only possible after one particular center orientation could be measured separately [53].

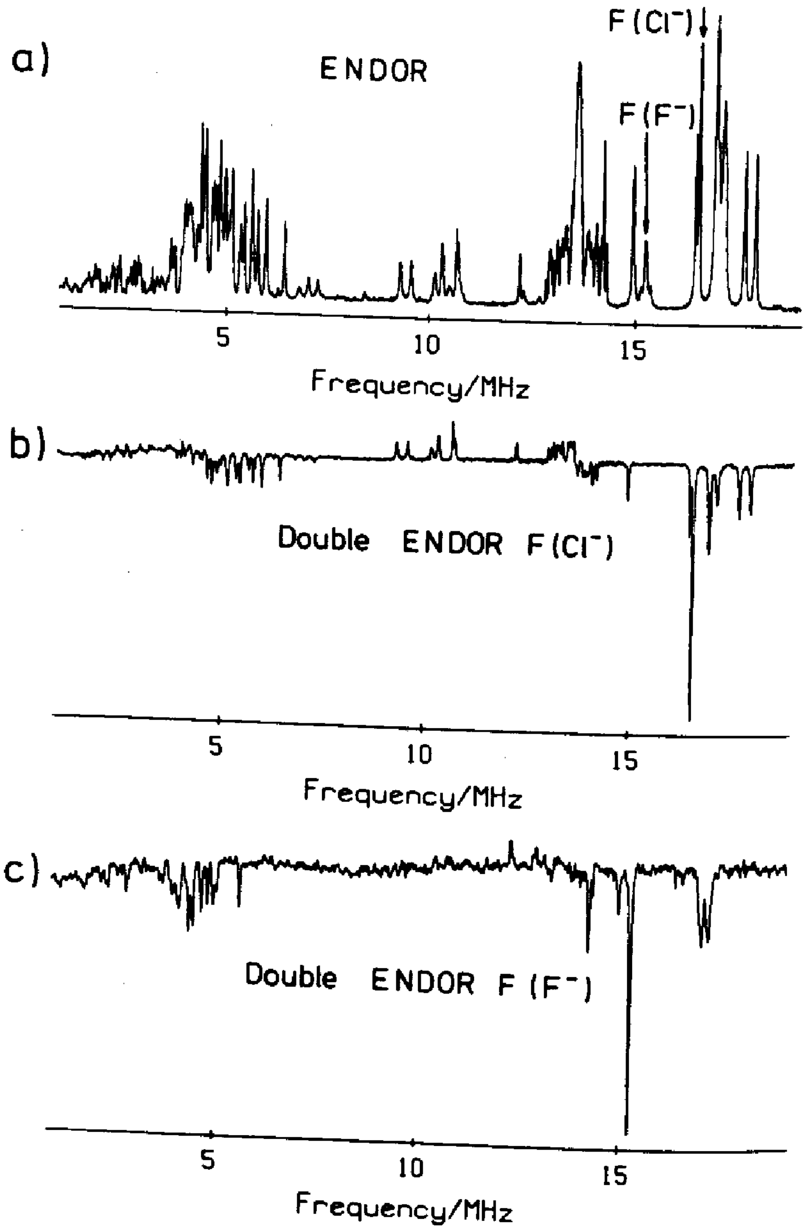

Figure 6.37 (*a*) Part of the ENDOR spectrum of $F(\mathrm{Cl}^-)$ and $F(\mathrm{F}^-)$ centers simultaneously present in BaFCl. (*b*) Double-ENDOR spectrum obtained for setting one frequency to an ENDOR line of $F(\mathrm{Cl}^-)$ centers (see arrow in Figure 6.37*a*) and sweeping the second radio frequency. (*c*) Double-ENDOR spectrum for setting one radio frequency to an $F(\mathrm{F}^-)$-ENDOR line (see arrow in Figure 6.37*a*). Reprinted with permission from J. R. Niklas, R. U. Bauer, and J.-M. Spaeth, *Phys. Status Solidi B*, **119**, 171 (1983).

6 OPTICALLY DETECTED ELECTRON SPIN RESONANCE AND ELECTRON NUCLEAR DOUBLE RESONANCE

6.1 Introductory Remarks

There are several ways to detect ESR optically. Selection of a technique depends on the system to be studied and on the kind of question to be answered. Compared to *conventional* ESR the optical detection, if possible, has several advantages about the identification of defects: (1) higher sensitivity, (2) higher selectivity, (3) direct correlation between structural and bulk properties of a crystal, (4) possibility to investigate optical excited states, (5) possibility to investigate ESR and ENDOR with high spatial resolution.

Sensitivity enhancement can be up to 10^4-10^5, compared to the conventional ESR, depending on the method used and the physical parameters of the system. The high selectivity results from the use of single absorption or emission bands for the detection. The bands of different defects usually do not overlap entirely; hence, spectra from these defects can be measured separately. A correlation of optical properties with structural property is based on the same argument. Relaxed excited states of sufficient radiative lifetimes can be studied. The condition is that the microwave transition rate is of the same order or bigger than the reciprocal radiation lifetime. If this condition is not fulfilled, during the lifetime of the state no occupation changes of the Zeeman levels can be induced by the microwaves. Electron spin resonance spectra of excited states with lifetimes of about microseconds were detected several times. The actual technical limit, which is given mainly by the microwave amplitude to be fed into the cavity at low temperature, is probably at lifetimes of about 100 ns.

The optical detection of ESR is based on either the observation of a microwave-induced intensity change in luminescence or the observation of microwave-induced changes of the degree of polarization of absorption or emission. The Zeeman levels involved must be occupied differently, and the radiative transitions must differ in polarization properties. It should be noted that the Zeeman splitting of the levels is only about 10^{-4} eV, while the phonon broadening of the levels caused by electron phonon coupling is three orders of magnitude greater. Fortunately, the polarization of the optical absorption or emission transitions is usually only affected slightly by the phonons, so that microwave-induced population changes within the Zeeman levels can be observed.

The examples and methods following are chosen mainly with respect to defect identification. For example, interesting studies like radiative–nonradiative transitions or electron transfer in excited states for which ODMR is an excellent tool and the study of relaxed excited states are not mentioned if the defect model is known from ground-state ESR.

Optical detection of ESR using the polarization change of absorption bands was recently proven to be more sensitive than the simple population transfer picture predicts. In particular, the observed high signal intensity for ENDOR was quite surprising and is not yet understood. Its use, however, is very valuable in various areas of materials science.

There is a great interest in being able to measure ESR and ENDOR with spatial resolution, especially in semiconductor physics, where homogeneous wafers are needed for device applications. Methods modeled after the successful NMR tomography are less suitable, since with the large Bohr magneton the necessary magnetic field gradients are too high compared to the nuclear magneton. However, the optical detection of ESR and ENDOR easily achieves a rather good spatial resolution, which is limited by the diameter of the optical beam used and, of course, the S/N ratio, since with too little light intensity the signal becomes very weak. First experiments of this kind are discussed in Section 6.7.

6.2 Basic Features of Optical Transitions of Defects in Solids

In ionic and semiconductor crystals many defects have localized energy states within the band gap and possess optical absorption with energies below the band gap energy. Figure 6.38*a* shows this schematically for the transition from the defect ground state to the first excited state. The absorption is then observed within the *optical window* of the crystal, where no band-gap transitions ($h\nu < E_g$) and no transitions caused by lattice vibrations occur. This window ranges from several to about 0.1 eV.

The correlation of such a defect-induced optical absorption with a particular defect is usually a difficult task. This is demonstrated, for example, by the long history of the research on color centers in alkali halides [54]. Assignments are usually attempted by variation of the irradiation time, if the defect is intrinsic like a vacancy or electron or hole center formed as a consequence of radiation damage. However, this is not always unambiguous. Several defects can be produced simultaneously with overlapping absorption bands. Often there is one characteristic luminescence band. The measurement of its excitation spectrum can be used to identify the associated absorption band provided no other defect luminescence band overlaps it strongly.

In ionic and semiconductor crystals most defect states are sensitive to the positions of the nearby atoms or ions so that the form of the absorption and the form and the energy position of the emission depend on the vibrations of the

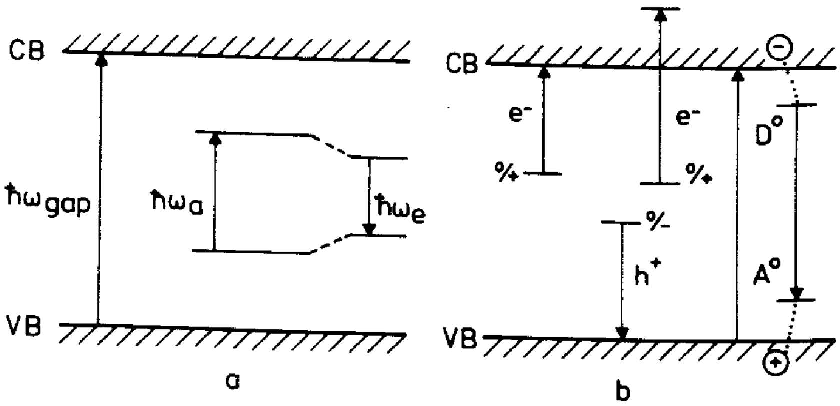

Figure 6.38 Schematic representation of several optical transitions in solids. (*a*) Intracenter absorption and emission with Stokes shift. Such transitions mostly occur in wide band-gap materials such as insulators. (*b*) Ionizing transitions to the conduction band and valence band, intracenter transitions into resonant states in the conduction band and D^0–A^0 donor–acceptor pair recombination luminescence after creating an electron-hole pair by band-gap illumination and capturing of electrons and holes by the D^+ donors and A^- acceptors.

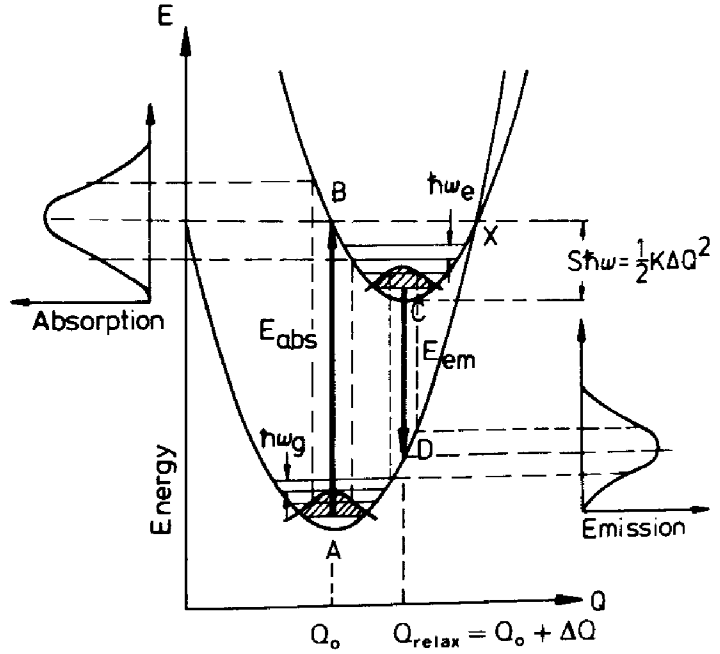

Figure 6.39 Configurational coordinate (CC) diagram of optical absorption and emission.

surrounding ions. This is conveniently discussed in the approximation of the configuration coordinate diagram (CC diagram), where the lattice vibrations are represented by a single localized mode with a configuration coordinate Q and linear coupling is assumed for the vibrational energy, which results in a parabolic energy curve for both the ground and excited states (see Figure 6.39). They have the form

$$E = \tfrac{1}{2}KQ^2 \tag{33}$$

where K is a force constant. Absorption and emission are vertical transitions (Born–Oppenheimer approximation). After the electrical dipole transition of the absorption has occurred, the electron distribution is changed and accordingly the lattice will relax and adjust to a new equilibrium position represented by $Q_0 + \Delta Q$ in Figure 6.39. From the vibrational ground state of the excited state parabola the emission takes the form of a transition to a ground-state configuration, which must relax back into the original configuration. The relaxation process involves phonon emission, which is the reason for the observed Stokes shift ΔE between the energies of absorption and emission ($\Delta E = E_{\text{abs}} - E_{\text{em}}$); ΔQ is directly related to the strength of the electron phonon coupling, which is characterized by the Huang–Rhys factor S

$$S \cdot \hbar\omega = \tfrac{1}{2}K \cdot \Delta Q^2 \tag{34}$$

where ω is the vibrational frequency (assumed to be equal in ground and excited states in the simplest approximation).

For large electron phonon coupling ($S > 10$) the shapes of the absorption and emission bands are approximately Gaussian with a half-width proportional to $\hbar\omega\sqrt{S}$. This is indicated in Figure 6.39. Typical half-widths are several tenths of an electron volt.

If the coupling is weak ($S < 1$), both ground- and excited-state parabolas are hardly displaced against each other and the dominant feature is the *zero phonon line* (ZPL). The transition involves no vibrational energies. Typical examples are transitions within the $4f^n$ configuration in rare earth ions in solids or for $3d^n$ configurations of transition metals in semiconductors (see Section 6.6).

In intermediate coupling ($1 < S < 6$) the ZPL is resolved, but the multiphonon structure is the dominant feature of the spectrum. The intensity of the ZPL relative to the whole band is given by $\exp(-S)$. It becomes undetectable for high values of S.

When a ZPL can be measured, the application of uniaxial stress and magnetic and electrical fields can cause a splitting of the ZPL, from which structural information such as the defect symmetry can be derived (e.g., [54] Chapters 5 and 6 and further references therein for ionic crystals).

Defects with a strong electron phonon coupling may not show a luminescence or may show only a very weak one. In the simple framework of the CC diagram a nonradiative deexcitation occurs, when the excited-state energy reached in a Franck–Condon absorption transition (point B in Figure 6.39) lies above the intersection of ground- and excited-state potential energy curves (point C in Figure 6.39). Here the system can be deexcited through the intersection directly into the ground state under phonon emission. In the approximation of linear coupling and equal vibration frequencies for ground and excited states this occurs when $E_{\mathrm{em}} < \frac{1}{2}E_{\mathrm{abs}}$ (Dexter–Klick–Russel rule) [55, 56].

In semiconductors the excited states of intracenter transitions can also be resonant states in the conduction band. Upon excitation with light of energy exceeding the band-gap energy electron hole pairs are created in the conduction and valence band and a donor–acceptor pair recombination luminescence can occur. An ionized donor D^+ captures an electron from the valence band to form D^0, and an ionized acceptor A^- captures a hole to form A^0. The paramagnetic pair D^0–A^0 recombines; that is, its electron and holes recombine and emit a fluorescence light. Its photon energy depends on the energy levels of the donors and acceptors and on their Coulomb energy [57] (Figure 6.38*c*). Defects in semiconductors can also be ionized by irradiation with light. Both electron emission into the conduction band and hole emission into the valence band occur. The photon energy at the onset of this process is determined by the energy levels. The ionization cross sections are usually smooth functions of the photon energy and look like broad absorption regions. They can be measured until the band edge is reached.

6.3 Optical Detection of Electron Spin Resonance by Optical Emission

6.3.1 Triplet-State Optically Detected Electron Spin Resonance

Optically detected electron spin resonance measured in the optical emission has been a standard tool in the study of organic crystals and molecules within the properties of excited triplet states. A recent review by Lynch and Pratt [58] lists specific reviews on ODMR of triplet states in many areas together with ODMR or inorganic and semiconductor crystals. To illustrate the method an example is described for a two-electron center in CaO.

Defects with two valence electrons, for example, in a ns^2 configuration, often have relaxed excited triplet states, in which the two electrons have parallel spins, $S = 1$. The optical absorption leads first to a singlet excited state with $S = 0$, which then relaxes into the triplet state by intersystem crossing. The two electrons then possess a fine structure interaction (e.g., caused by dipole–dipole interaction), so that in first-order perturbation theory the energy is given for an axially symmetric fine structure tensor and B_0 parallel to its principal z axis

$$E = g_z \mu_B B_0 m_s + D_z[m_s^2 - S(S+1)] \tag{35}$$

Figure 6.40 shows the level scheme as a function of the magnetic field of the spin Hamiltonian containing fine structure and the electron Zeeman interaction ($D = D_z$). The three levels are all occupied as a result of relaxation from a higher singlet state. Radiative transitions from the triplet states into the singlet ground states are forbidden. However, the states $|+1\rangle$ and $|-1\rangle$ can mix with excited singlet states by the spin–orbit interaction; therefore, a finite radiative transition probability into the ground state is observed for these levels, while $|0\rangle$ cannot decay by radiative transitions. The radiative lifetimes of the $|+1\rangle$ and $|-1\rangle$ levels depend on the size of the spin–orbit interaction and the energy separation of excited singlet states from the triplet state.

Because of the radiative decay of the $|+1\rangle$ and $|-1\rangle$ levels, these levels are less populated in a stationary state compared to the level $|0\rangle$, where population is accumulated (see Figure 6.40). It is assumed that the spin lattice relaxation time T_1 is large compared to the radiative lifetime. Therefore, the microwave transition $|0\rangle \to |+1\rangle$ and $|0\rangle \to |-1\rangle$ shift population into the radiative levels, upon which the luminescence intensity is enhanced. This can easily be observed. On the other hand, one can also observe the magnetic circular polarization of the emission $(I_+ - I_-)$(MCPE), where for the low-field transition there is an enhancement, and for the high-field transition a decrease is observed (see Figure 6.40, where $D > 0$ is assumed).

The F centers in CaO, where an O^{2-} vacancy is occupied by two electrons, do have such relaxed excited triplet states, and their ODESR was observed in such a way [59, 60]. Figure 6.41 shows as an example the ODESR spectrum of

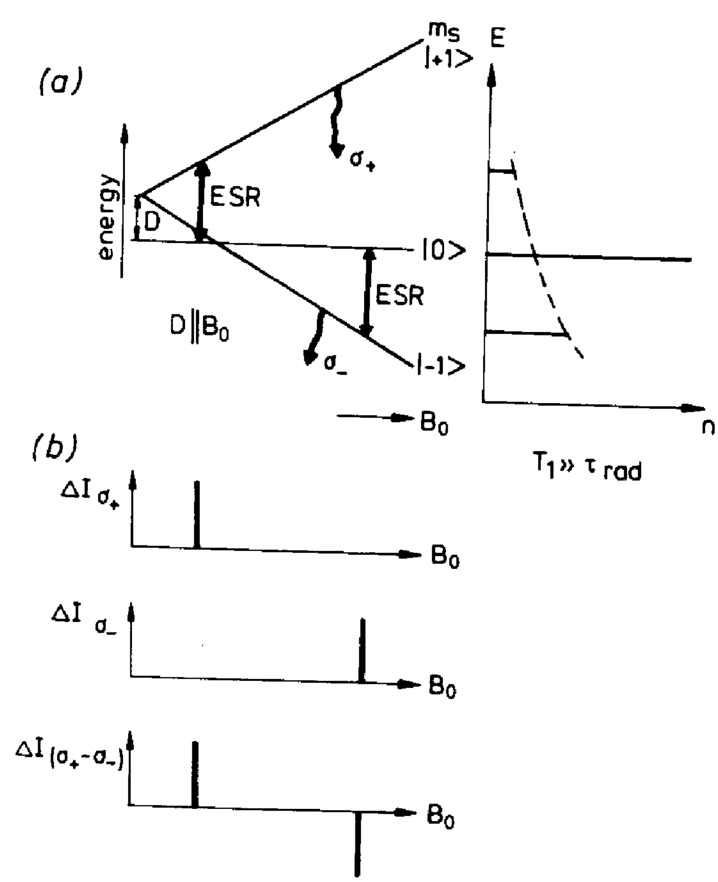

Figure 6.40 (*a*) Level scheme of triplet states to illustrate the optical detection of ESR by microwave-induced change in the luminescence intensity or by the magnetic circular polarization of the emission (MCPE). It is assumed that $B_0 \| D_z$, $T_1 \gg \tau_{rad}$. (*b*) Schematic representation of the microwave-induced intensity changes of circularly polarized light.

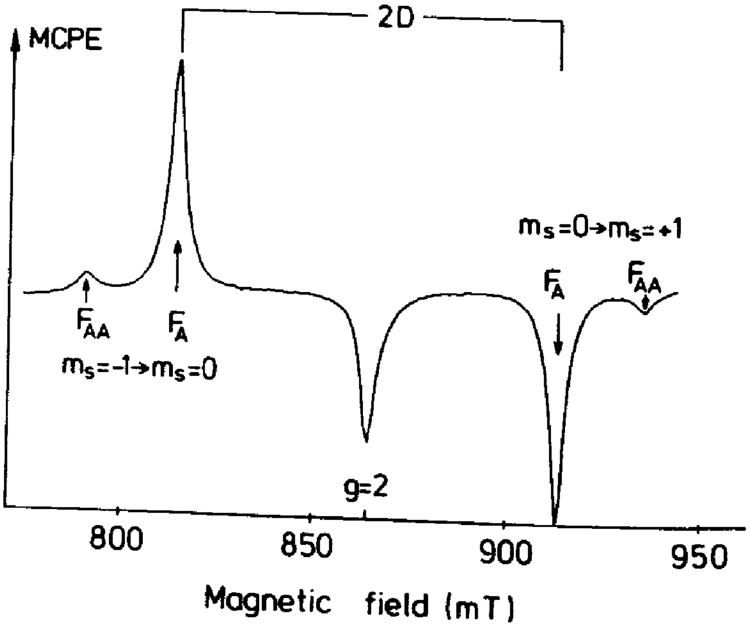

Figure 6.41 Magnetic circular polarization of the emission (MCPE) recorded at $\lambda > 700$ nm under microwave irradiation (24 GHz) as a function of the magnetic field ($B_0 \| \langle 100 \rangle$) in CaO containing F_A(Mg) and F_{AA}(Mg) centers. The F_A(Mg) centers are two electrons trapped at an oxygen vacancy next to a Mg^{2+} impurity. The F_{AA}(Mg) centers have two Mg^{2+} impurities opposite each other along a $\langle 100 \rangle$ direction next to the trapped electron; $T = 1.6$ K. Adapted with permission from *Solid State Commun.*, **43**, F. J. Ahlers, F. Lohse, and J.-M.Spaeth, "Application of Magnetic Resonance Techniques to the Study of Defects in Solids," Copyright 1982, Pergamon Journals, Ltd.

F_A and F_{AA} centers in CaO doped with Mg^{2+} that is observed at 700 nm. Both centers differ slightly in their fine structure constant D. Measurements with higher resolution show a superhyperfine interaction with the 10% abundant $^{25}Mg(I = \frac{5}{2})$. Six equidistant superhyperfine lines can be resolved [60, 61]. In the F_A center there is one Mg^{2+} next to the O^{2-} vacancy; in the F_{AA} center, two Mg^{2+} are opposite to each other along a ⟨100⟩ axis.

6.3.2 Optically Detected Electron Spin Resonance by Donor–Acceptor Pair Recombination Luminescence

Until recently, in semiconductor physics the usual way to observe ODESR has been by donor–acceptor pair recombination luminescence. There are many results in II–VI semiconductors, such as ZnS and ZnSe, and also a great deal in III–V semiconductors, such as GaP. The reader is referred to the review by Cavenett [62].

The fundamental process is illustrated in Figure 6.42. After a band–band

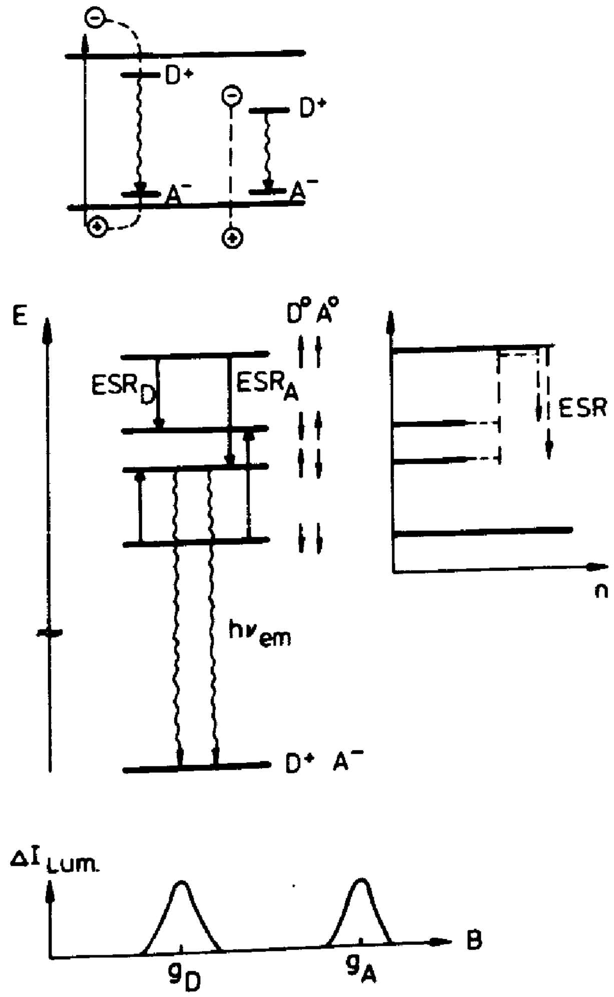

Figure 6.42 Schematic representation of donor–acceptor recombination in semiconductors and of the mechanism to observe the ESR as microwave-induced change in intensity of the donor–acceptor recombination luminescence.

excitation according to

$$D^{+} + A^{-} + e^{-} + h^{+} \rightarrow D^{0} + A^{0} \tag{36}$$

paramagnetic donors D^0 and acceptors A^0 are formed.

The unpaired electron at the donor and the unpaired hole at the acceptor can recombine with the emission of a luminescence radiation

$$D^{0} + A^{0} \rightarrow D^{+} + A^{-} + h\nu \tag{37}$$

The level scheme of D^0 and A^0 in a magnetic field is shown in Figure 6.42. The two spins are assumed to be very weakly coupled [62, 63]. Therefore, the energy positions of the levels are determined only by their respective g–factors and the magnetic field. Since a radiative decay from the two triplet states into the singlet ground state is forbidden, a luminescence is observed only from the two singlet states, where the two spins are antiparallel. Therefore, in a stationary state, the population of the two triplet states is higher compared to the two singlet states, similar, as previously discussed, to the state $|0\rangle$ in the highly coupled triplet system.

Upon the microwave transitions indicated in Figure 6.42 the recombination luminescence is increased, and in principle one can observe the ESR lines of both the donor and acceptor provided their g-factors are different enough. Usually, one observes only the donor resonance since the p-type hole states of the acceptors experience a dynamical Jahn–Teller effect, which makes the resonance very difficult to observe. The resonance can be observed on application of uniaxial stress that is large enough to suppress the dynamical Jahn–Teller effect.

With this technique the ODESR of anion antisite defects in GaP:Zn (p type) were recently observed. After band–band excitation two strongly overlapping luminescence bands can be observed, one peaking at 0.95 eV and the other at 1.20 eV. In the 0.95-eV luminescence a doublet ODESR spectrum is observed, which is caused by a P atom on a Ga site (*antisite*) with one unpaired electron. The doublet splitting is caused by the hyperfine interaction with the ^{31}P nucleus ($I = \frac{1}{2}$) [64, 65]. Using a specific modulation technique one can also resolve the superhyperfine interaction with four nearest ^{31}P neighbors from which the structure model can be inferred [64]. The acceptor resonance was not seen.

Figure 6.43 shows the ODESR spectrum measured in the 1.20-eV luminescence, which is caused by an antisite defect (however, in a triplet state) and which also contains the ESR line of the acceptor that is participating in the luminescence process. The two low- and high-field lines are caused by the antisite; the splitting between the two lines of each doublet is caused by the ^{31}P hyperfine interaction, while the separation of the centers of the two doublets (between ca. 240 and 400 mT) corresponds to the separation of the lines in Figure 6.41 and is caused by the fine-structure interaction. It was concluded that

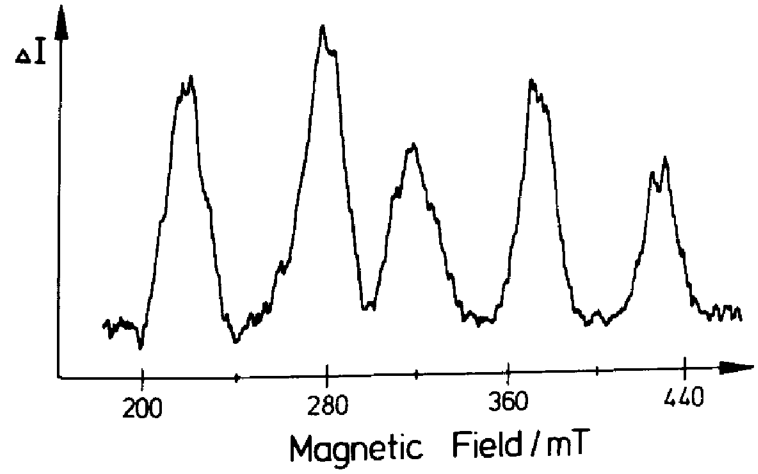

Figure 6.43 X-band ODESR spectrum observed as a microwave-induced change of the donor–acceptor recombination luminescence in GaP:Zn (excitation wavelength 514 nm). The spectrum shows the P-antisite donor $P_{Ga}P_3Y_P$ in a triplet state and the acceptor (central line), which is probably an interstitial Fe^{3+}. $B_0 \parallel \langle 111 \rangle$. Reprinted with permission from B. K. Meyer, Th. Hangleiter, J.-M. Spaeth, G. Strauch, Th. Zell, A. Winnacker, and R. H. Bartram, *J. Phys. C*, **18**, 1503 (1985).

the structure model is a PP_3Y_p defect with an unknown atom on one of the four nearest-neighbor P sites and that the acceptor may be a nearby interstitial Fe^{3+} impurity [66]. The level of the defect is at $E_v + 1.5$ eV, where E_v is the energy of the valence band. The PP_3Y_p defect can be excited into its triplet state by direct excitation from the valence band with subband gap light, a possibility also indicated schematically in Figure 6.42. This excitation enhances the luminescence, since the defects can be excited in the bulk of the crystal and not only in a thin surface layer, as is usually the case for band–band transitions caused by the high absorption constant.

When measuring the ODESR by recombination luminescence a common difficulty is that there is a spatial distribution between donors and acceptors and that the exchange interaction between them can be large and varying according to distances. It is especially large for shallow donors and acceptors. This results in a broadening of the ESR lines. Therefore, in most cases the donor resonances show no hyperfine or superhyperfine structures, and a defect identification can be based only on the g-factors.

There are many resonances known from which the defect cannot be identified. The broadening effect is less important for *deep level* defects. One way to overcome this difficulty is to measure the ODESR spectrum with time resolution. It was shown for shallow In-donors in ZnO that the resolution can be greatly enhanced by exciting the luminescence with pulsed light and by taking only the long lifetime tails of the luminescence for the ODESR measurement, which comes from the distant donor–acceptor pairs for which the exchange interaction is only small [67]. Little work has been done so far with time-resolved ODESR for solid-state defects.

6.4 Absorption-Detected Electron Spin Resonance (Magnetic Circular Dichroism Method)

The detection of ground-state ESR by measuring the microwave-induced change of the magnetic circular dichroism (MCD) is long known from color center physics [68], but it was not applied to materials science until very recently. It was originally devised to study excited states of *F* centers in alkali halides. Its recent use for ground-state ESR proved particularly useful in both semiconductor physics and inorganic systems like crystals with laser-active defects.

In Figure 6.44 the idea of the method is schematically indicated for the simplification of an *atomic* optical *s*–*p* transition.

The allowed optical absorption transitions for right and left circular polarized light are indicated along with the relative matrix elements. The absorptions for both polarizations are split in energy by the spin–orbit splitting of the excited state. If this splitting is smaller compared to the phonon width of

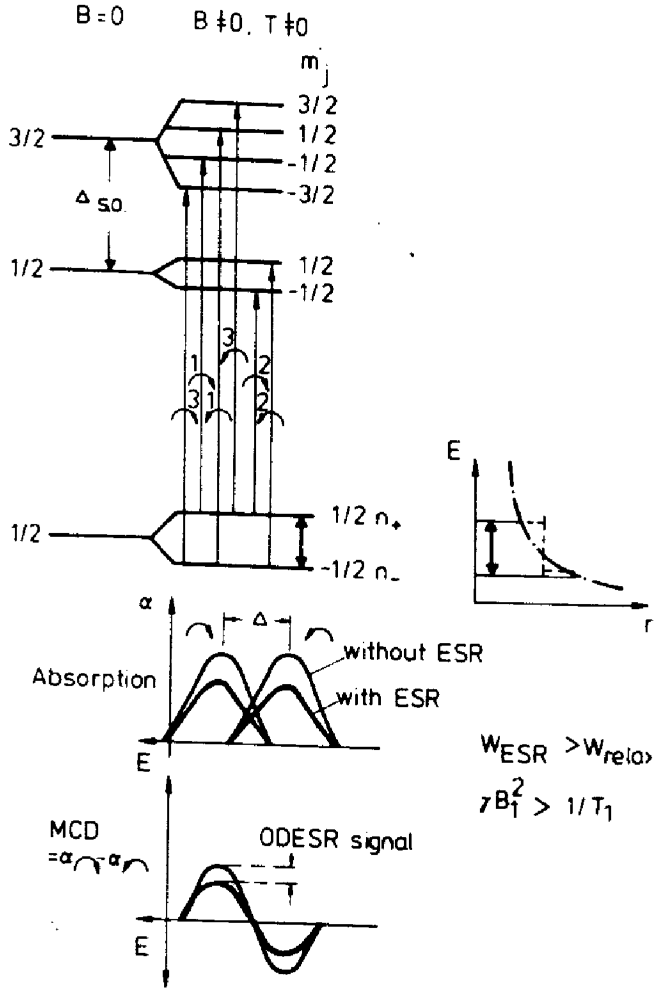

Figure 6.44 Simple *atomic* model to explain the magnetic circular dichroism (MCD) of the absorption and its microwave-induced decrease to detect ESR transitions.

the absorption bands the measurement of the MCD as a function of photon energy yields a derivative structure.

The MCD is defined as

$$\mathrm{MCD} = \frac{d}{4}(\alpha^+ - \alpha^-) \tag{38}$$

where d is the crystal thickness and α^+, α^- are the absorption constants for right and left circular polarized light, respectively. If the absorption comes from a Kramers doublet with $S = \frac{1}{2}$, one obtains [68]

$$\mathrm{MCD} = \tfrac{1}{2}\alpha_0 d \frac{\sigma^+ - \sigma^-}{\sigma^+ + \sigma^-} \frac{n_- - n_+}{n_- + n_+} \tag{39}$$

where α_0 is the absorption constant for unpolarized light, σ^+ and σ^- are the cross sections for right and left polarized light, respectively, and n_- and n_+ are the occupation numbers for the $m_s = \pm\frac{1}{2}$ states. The MCD is thus proportional to the occupation difference $n_+ - n_-$ and the cross-section difference $\sigma^+ - \sigma^-$.

The occupation difference $n_+ - n_-$ can be decreased by a microwave transition, provided the microwave transition rate is about the same as or larger than the spin–lattice relaxation rate $1/T_1$. Such an ESR transition thus results in a decrease of the MCD, which is monitored (see Figure 6.44). One measures the MCD as a function of the magnetic field under microwave irradiation. The decrease caused by the resonance is observed on the variation of the MCD as a function of the magnetic field according to

$$\mathrm{MCD} \sim \tanh(g\mu_B B_0/2kT) \tag{40}$$

For low temperatures and the usual field variation this is practically a linear function of B_0.

Figure 6.45*a* shows the absorption spectrum of a Tl-doped KCl crystal after X irradiation at −40°C; Figure 6.45*b* is the MCD spectrum of this crystal after bleaching the *F* centers generated simultaneously. There are many centers created, partly diamagnetic, partly paramagnetic. Figure 6.46 shows the ODESR spectrum measured in the absorption band at 1040 nm of the laser-active $\mathrm{Tl}^0(1)$ centers [69]. The absorption at 1040 nm has a negative paramagnetic MCD. Comparison with the ESR spectrum of $\mathrm{Tl}^0(1)$ centers identified in Figure 6.9 [13] shows that the spectrum is identical if one allows for the two different microwave bands used (*X* band for conventional ESR, *K* band for ODESR). However, in ODESR, a direct correlation with an optical absorption band at 1040 nm was possible (see also Section 6.6.2). The centers consist of a Tl^0 atom next to an anion vacancy along ⟨100⟩ [13]. The ODESR spectrum contains allowed transitions of centers with their ⟨100⟩ axes parallel and perpendicular to the magnetic field orientation (indicated in Figure 6.46) as well as forbidden transitions, in which the Tl nuclear quantum numbers ($m_I = \frac{1}{2}$) also

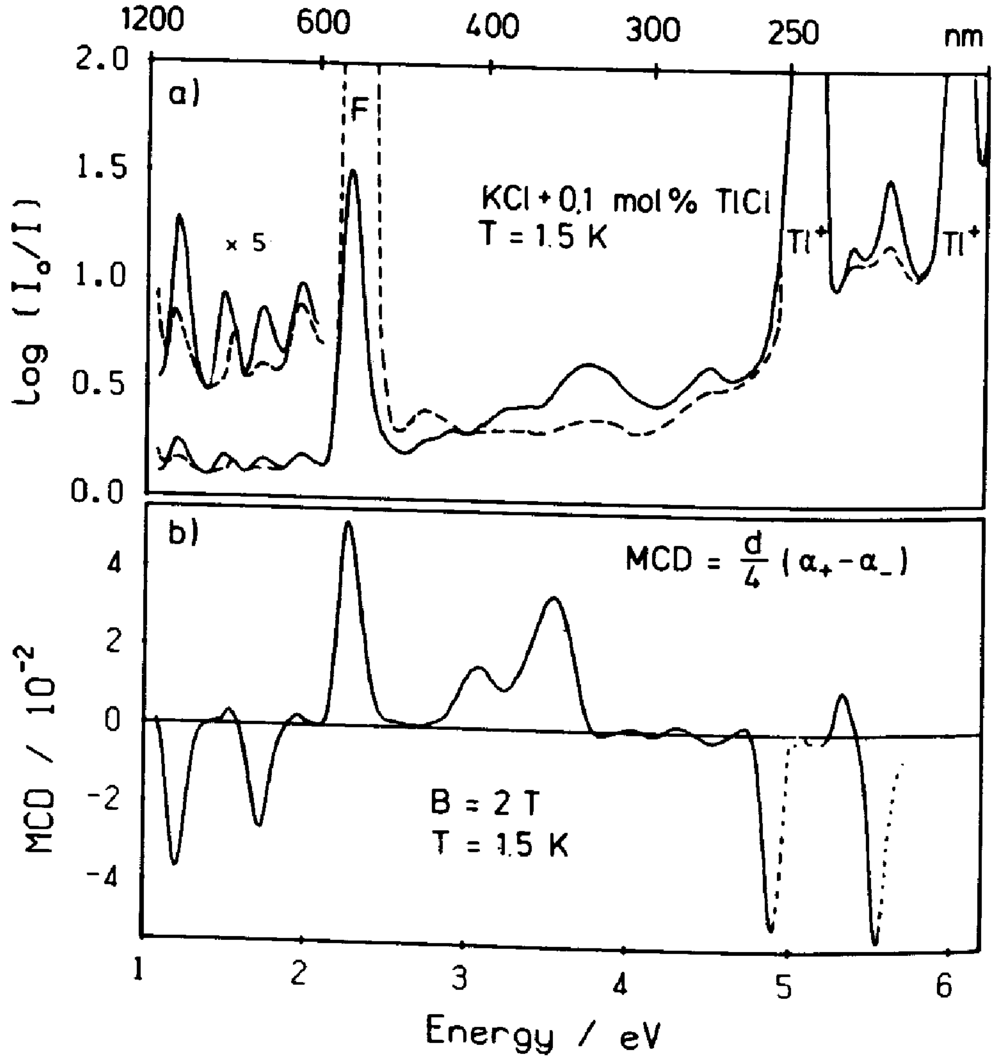

Figure 6.45 (*a*) Optical absorption spectrum of KCl–Tl after X irradiation at −40°C (dashed line) and after *F*-center bleaching (solid line). (*b*) Magnetic circular dichroism (MCD) after *F*-center bleaching. Reprinted with permission from F. J. Ahlers, F. Lohse, J.-M. Spaeth, and L. F. Mollenauer, *Phys. Rev. B*, **28**, 1249 (1983).

change. Their intensity decreases with decreasing microwave power (Figure 6.46*a* and *b*) [69].

Figure 6.47 shows the optical absorption of the MCD in *as-grown*, undoped GaAs, which was grown by the liquid encapsulated Czochralski (LEC) method. In the absorption below the gap energy of 1.52 eV only a very weak band at 1.18 eV caused by an intracenter transition of the diamagnetic mid-gap defect EL2 is detectable. However, the MCD reveals the existence of further intracenter absorption bands caused by paramagnetic defects, which turned out to be the singly ionized state of the EL2 defects [70]. In direct measurement their optical absorption is not detectable. The sensitivity enhancement that is evident when measuring the MCD is a consequence of the applied form of modulation spectroscopy. The optical transitions are caused by transitions into two resonant states in the conduction band [71].

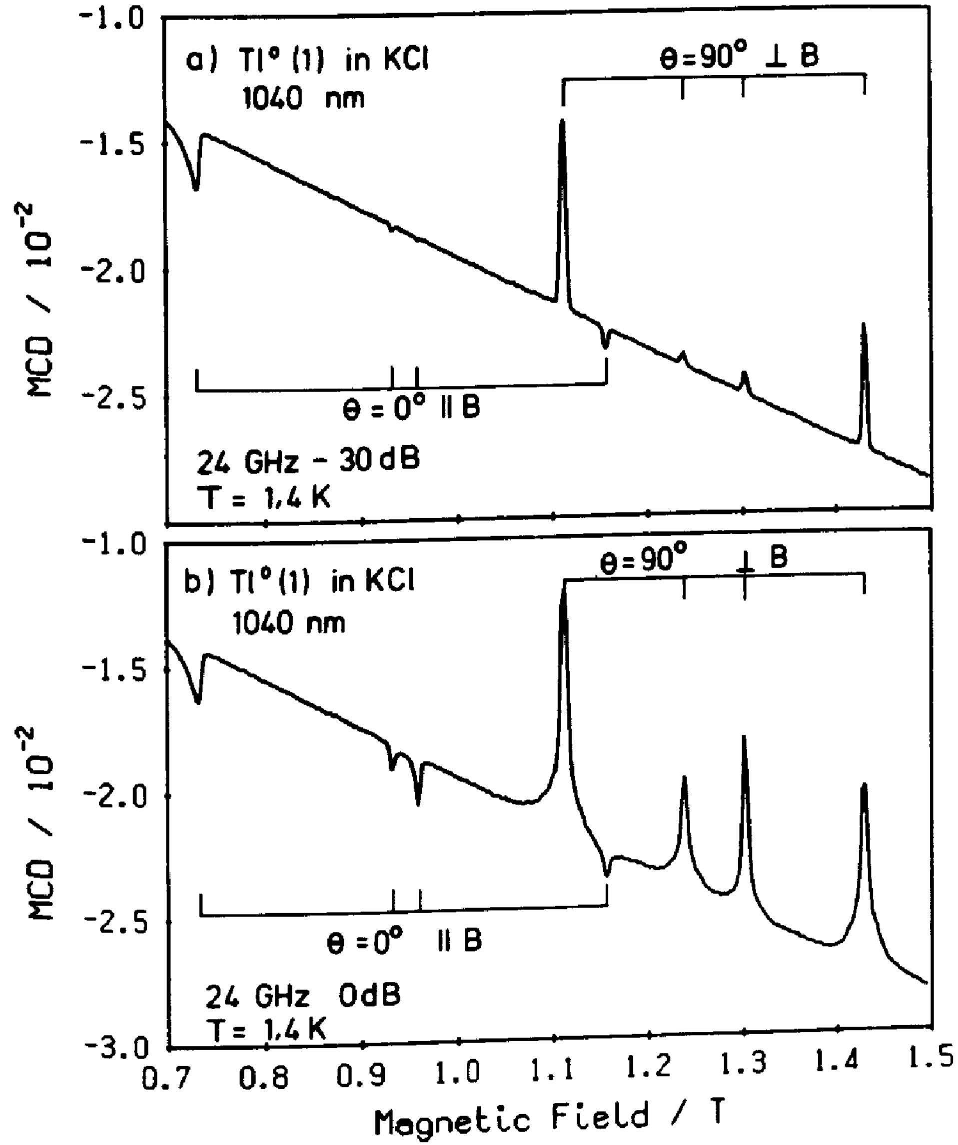

Figure 6.46 (*a*) An ODESR spectrum of $Tl^0(1)$ centers in KCl detected as a microwave-induced change of the MCD of the absorption band at 1040 nm, measured at low microwave power (24 GHz, 1.5 K). (*b*) Same for high microwave power.

When measuring the ODESR in this MCD, for example, at 1350 nm, the spectrum of Figure 6.48, which is due to paramagnetic EL2 defects, is observed. The defect structure was revealed by ODENDOR (see Section 6.5) to be an As antisite–As interstitial pair defect. The ESR spectrum shows the central hyperfine interaction between the unpaired electron with the ^{75}As nucleus ($I = \frac{3}{2}$). The conventional ESR of this defect in as-grown material is very weak; the S/N ratio is about 2:4 (the concentration of paramagnetic EL2 is ca. $10^{16} cm^{-3}$). In ODESR there is a gain in S/N of about two orders of magnitude.

Other examples of ODESR spectra measured recently are those of Pb^+ ions on cation sites next to an F^- vacancy in CaF_2, CrF_2 and BaF_2 [72, 73], which are analogous to the laser-active Tl defects previously discussed. Also Fe^{3+} in InP [74] and V^{2+} and V^{3+} on Ga sites in GaAs [74–76] can be measured. In

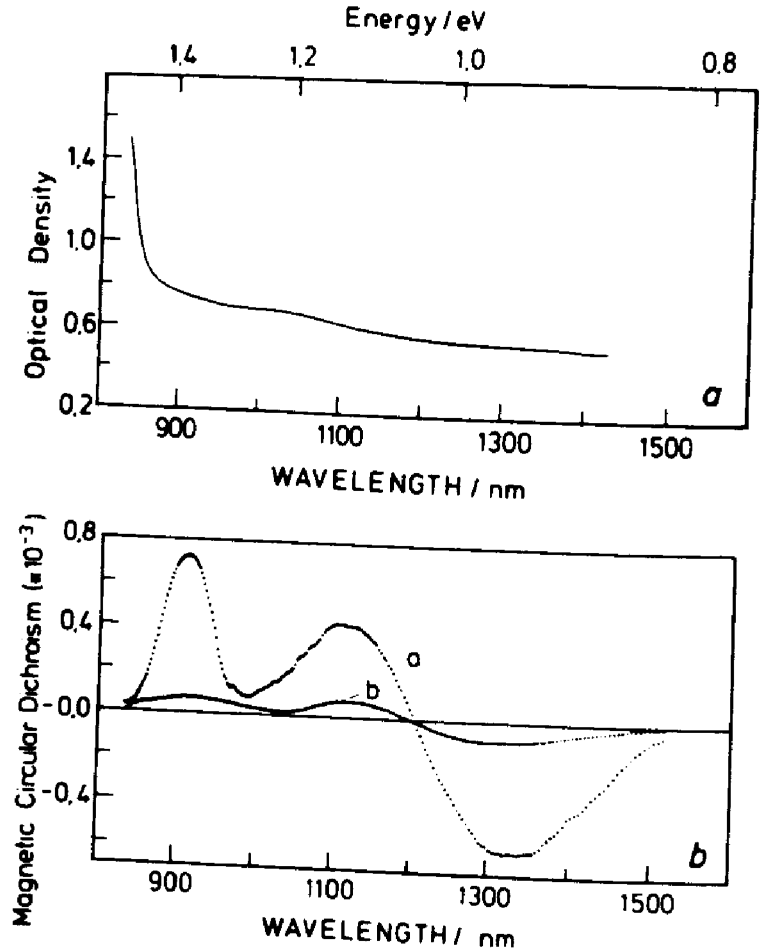

Figure 6.47 (*a*): Optical absorption of *as-grown* semi-insulating GaAs at 1.4 K (crystal thickness 0.3 mm). (*b*): curve a, MCD of the same sample. $T = 4.2$ K, $B = 2$ T; curve b, excitation spectrum of the ODESR lines of the paramagnetic EL2 defects (MCD tagged by the EL2 ESR lines). Reprinted with permission from B. K. Meyer, J.-M. Spaeth, and M. Scheffler, *Phys. Rev. Lett.*, **52**, 851 (1984).

the ODESR spectra of the transition metals in III–V semiconductors the ESR spectra were observed not only in their intracenter absorption bands, but also in the ionizing transitions to both the conduction and the valence bands [76]. This observation was unexpected. However, it renders the MCD technique particularly powerful, since ionizing transitions of defects into bands are almost always present with rather good transition probabilities.

6.5 Optically Detected Electron Nuclear Double Resonance

Except for triplet states in organic systems only very few experiments were performed, where ENDOR was observed in luminescence [77]. In ionic crystals it was Tm^{2+} in CaF_2 [78], a rare earth defect. A few observations were reported in semiconductors using the donor–acceptor recombination luminescence. There are observations in amorphous Si [79, 80] and in ZnSe [81]. The ENDOR lines were observed as an emission increase when NMR transitions

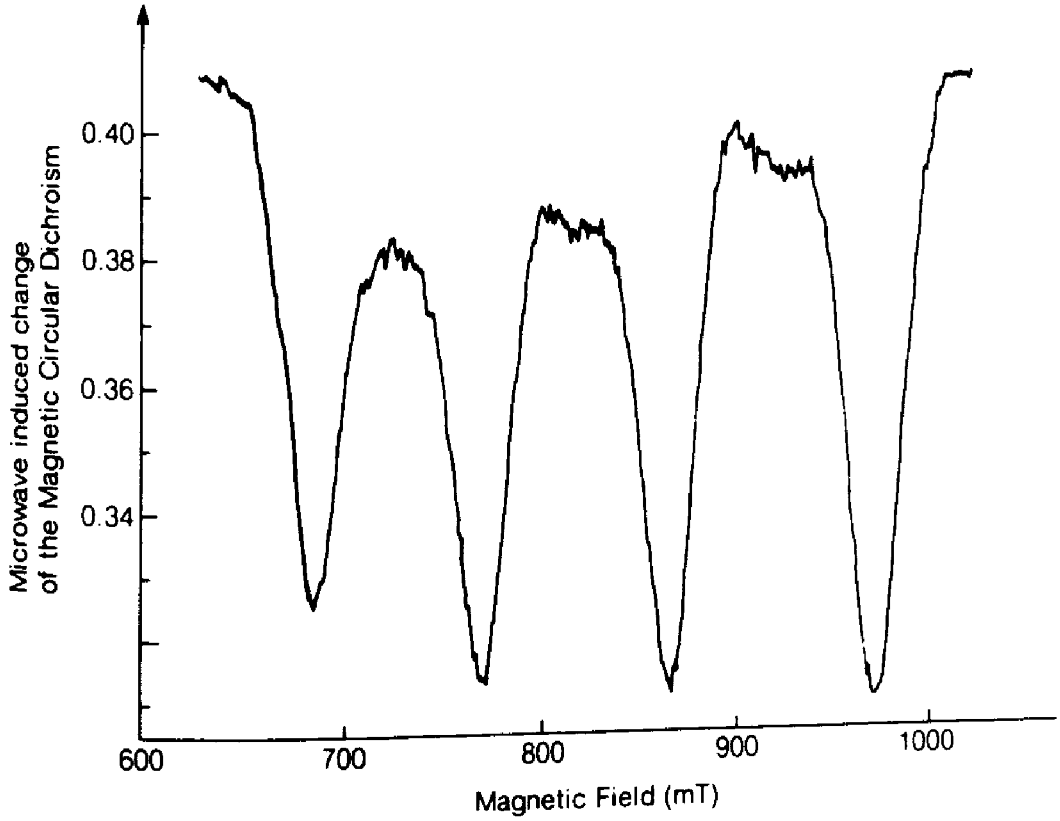

Figure 6.48 Optically detected ESR spectrum of paramagnetic EL2 defects in semi-insulating *as-grown* GaAs as microwave-induced decrease of the MCD of the absorption measured at 1350 nm $B_0 \parallel \langle 100 \rangle$, $T = 1.5$ K, $\nu_{ESR} = 24$ GHz. Reprinted with permission from B. K. Meyer, J.-M. Spaeth, and M. Scheffler, *Phys. Rev. Lett.*, **52**, 851 (1984).

were induced by a radio frequency applied in a small loop attached to the sample. In ZnSe, for example, two lines caused by ^{67}Zn and ^{77}Se were seen centered at the frequencies of the free nuclei. The emission enhancement effect was about 1%. The ENDOR lines were broad, about an order of magnitude broader than in conventional ENDOR. No angular dependence is reported [81]. Using time-resolved techniques ENDOR of ^{115}In in ZnO was observed [67].

The observation of ENDOR by emission has a principal disadvantage. If the lifetime of an excited state giving rise to the emission is 1 μs or shorter, then the homogeneous ENDOR line width is 1 MHz or more. Thus, one loses all the detailed information necessary for the structure determination. Furthermore, to be able to shift populations between nuclear Zeeman levels within the radiative lifetime one needs very high NMR transitions probabilities, requiring radio frequency field strengths of 10 mT or more, which at low temperatures causes quite a technical problem.

A better way to observe ODENDOR seems to be by the MCD technique. In principle, both ground-state and excited-state ENDOR can be observed, provided there is a closed optical pumping cycle. For the excited state the same restrictions apply as discussed previously for the emission method (Section 6.3).

Figure 6.49 shows the level scheme when $S = \frac{1}{2}$, and there is a central nucleus with $I_c = \frac{3}{2}$ and one ligand nucleus with $I = \frac{3}{2}$ (e.g., a simplified model for the paramagnetic EL2 defect in GaAs). In the experiment one sets the magnetic field onto a particular position of the ODESR line, for example, into the flank. Electron spin resonance transitions must obey the selection rule $\Delta m_I = 0$, $\Delta m_s = \pm 1$. Thus, when measuring the ESR in one of the four lines of the $I_c = \frac{3}{2}$ system, then at most only $\frac{1}{4}$ of all the spin packets can be involved; only $\frac{1}{4}$ of the MCD can be decreased when saturating the transition. However, if each line is inhomogeneously broadened by further superhyperfine interactions, only a fraction of a decrease should occur, since $\Delta m_{I,a} = 0$ must be obeyed for the ligand I_a. Thus, upon inducing NMR transitions between the nuclear Zeeman levels, one can include more $m_{I,a}$ substates into the ESR pumping cycle and thus increase the effect of decreasing the MCD. Therefore, the ENDOR transitions are detected as a further increase of the ODESR.

Figure 6.50 shows a section of the ODENDOR lines caused by the nearest ^{75}As neighbors of the paramagnetic EL2 defect in an as-grown, undoped GaAs crystal [70, 82, 83]. The ENDOR lines are as sharp and numerous as in conventional ENDOR. From their angular dependence the structure model of the EL2 defects can be derived.

A similar study was recently made for Pb$^+$ centers in CaF$_2$, SrF$_2$, and BaF$_2$, in which the structure was shown to be a Pb$^+$ ion on cation sites next to an F$^-$ vacancy along ⟨111⟩. The ^{19}F ENDOR lines measured in the MCD and their angular dependence clearly showed the symmetry of the defect and its atomic structure [72]. Similarly, as for EL2, the S/N ratio of the ENDOR lines was very good.

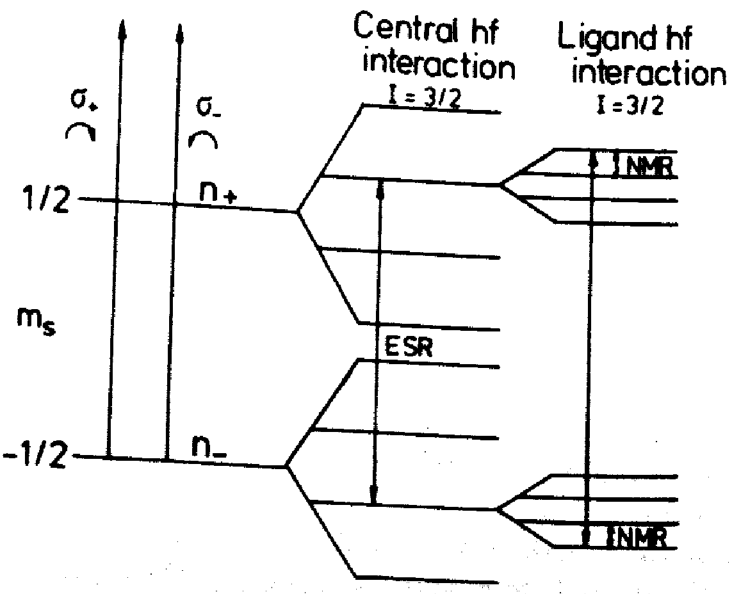

Figure 6.49 Level scheme to illustrate the detection of ENDOR by a radio frequency- and microwave-induced decrease of the MCD of the optical absorption.

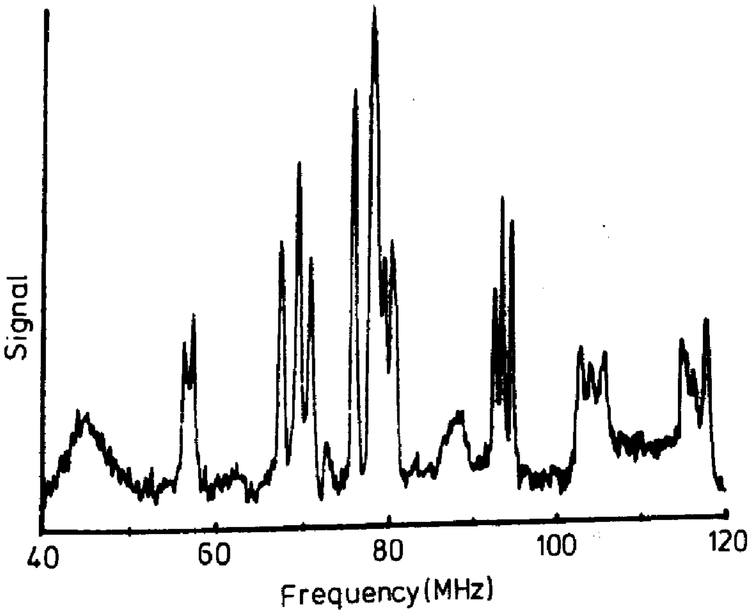

Figure 6.50 Section of the ODENDOR spectrum of the paramagnetic EL2 defects in semi-insulating *as-grown* GaAs. $T = 1.5$ K, with B_0 in a (110) plane. The lines are caused by five ^{75}As neighbors of the As_{Ga}^{+}, which forms the core of the EL^2 defect. Reprinted with permission from B. K. Meyer, D. M. Hofmann, J. R. Niklas, and J.-M. Spaeth, *Phys. Rev. B*, **36**, 1332 (1987).

6.6 Correlation of Optically Detected Electron Spin Resonance and Optically Detected Electron Nuclear Double Resonance With Bulk Properties

6.6.1 Energy Levels

As with the photo-ESR and photo-ENDOR experiments discussed in Section 4.5, photo-ODESR and photo-ODENDOR experiments can be performed to correlate with energy levels and thus with electrical properties of the solid. An investigation of the EL2 defects in undoped GaAs also revealed another kind of correlation, which can be achieved with such an experiment; that is, two energy levels belong to the same defect in different charge states. In Figure 6.51*a* the onset of the MCD (or ODESR) of paramagnetic EL2 centers is shown to occur at a photon energy of 0.52 eV. Before occupying this D^+/D^{2+} level no MCD could be measured. At a photon energy of 0.74 eV the MCD (and again correspondingly the ESR signal) decreases, since the level of the mid-gap EL2, which is diamagnetic, is now reached, a second electron is raised into the defect. At higher energies more and more paramagnetic EL2 defects are transferred into paramagnetic EL2 defects with a corresponding decrease of the MCD. This experiment shows that the two levels belong to the two different charge states of the same defect. After occupying the mid-gap EL2 level its optical intracenter band at 1.18 eV appears, which can be used to calibrate the lost MCD as a consequence of the occupancy of the mid-gap EL2 level. The intracenter band was calibrated by deep level transient spectroscopy [70, 83].

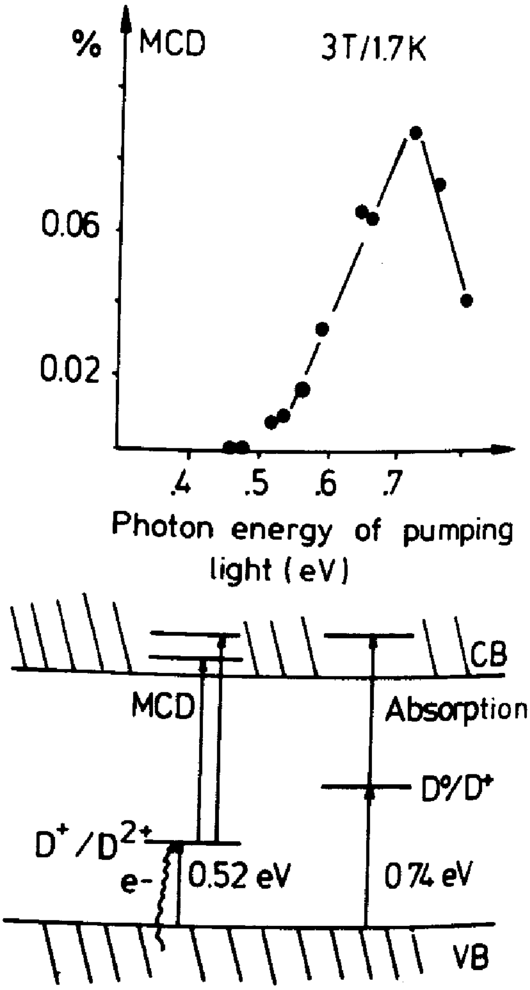

Figure 6.51 Excitation spectrum of the ODESR lines of the paramagnetic EL2 defects in semi-insulating *as-grown* GaAs:Zn (p-type). The paramagnetic EL2 level is occupied by raising the electrons from the valence band as from an exciting photon energy of $h\nu > 0.52\,\mathrm{eV}$. The diamagnetic EL2 level is occupied as from $h\nu > 0.74\,\mathrm{eV}$. The MCD of paramagnetic EL2 appears above the photon threshold of 0.52 eV and decreases again at 0.74 eV, where paramagnetic EL2 is transformed into diamagnetic EL2 by capturing an electron; $T = 1.7\,\mathrm{K}$, $B = 3\,\mathrm{T}$. Upper half: experimental results; lower half: level scheme of paramagnetic EL2/diamagnetic EL2. Reprinted with permission from B. K. Meyer, D. M. Hofmann, J. R. Niklas, and J.-M. Spaeth, *Phys. Rev. B*, **36**, 1332 (1987).

6.6.2 Tagging of the Magnetic Circular Dichroism by Electron Spin Resonance and Electron Nuclear Double Resonance

By detecting the ground-state ESR or ENDOR with the MCD method it is possible to measure a kind of excitation spectrum of the ESR and ENDOR lines of a specific defect. The schemes of Figures 6.44 and 6.49 apply to all transitions to the excited states of the defect, that is, to every optical absorption band belonging to the defect of which the ground-state ESR and ENDOR can be measured. Therefore, one can set the ESR or ENDOR resonance conditions to a particular ESR or ENDOR line, vary the optical wavelength, and monitor the ODESR or ODENDOR signal intensity as a microwave- (and radio frequency) induced change of the MCD. Thus, from the total MCD of a sample one can measure in this way only the part that belongs to the selected ESR or ENDOR signal. This is especially useful when a superposition of optical absorptions that were caused by several defects is present, which is, for example, typical with radiation damage and impurity problems. Figure 6.45*a* shows the optical absorption after X-irradiation of KCl doped with Tl; Figure 6.52*a* shows the MCD measured as the excitation signal of one ESR line of the $\mathrm{Tl}^0(1)$ center for

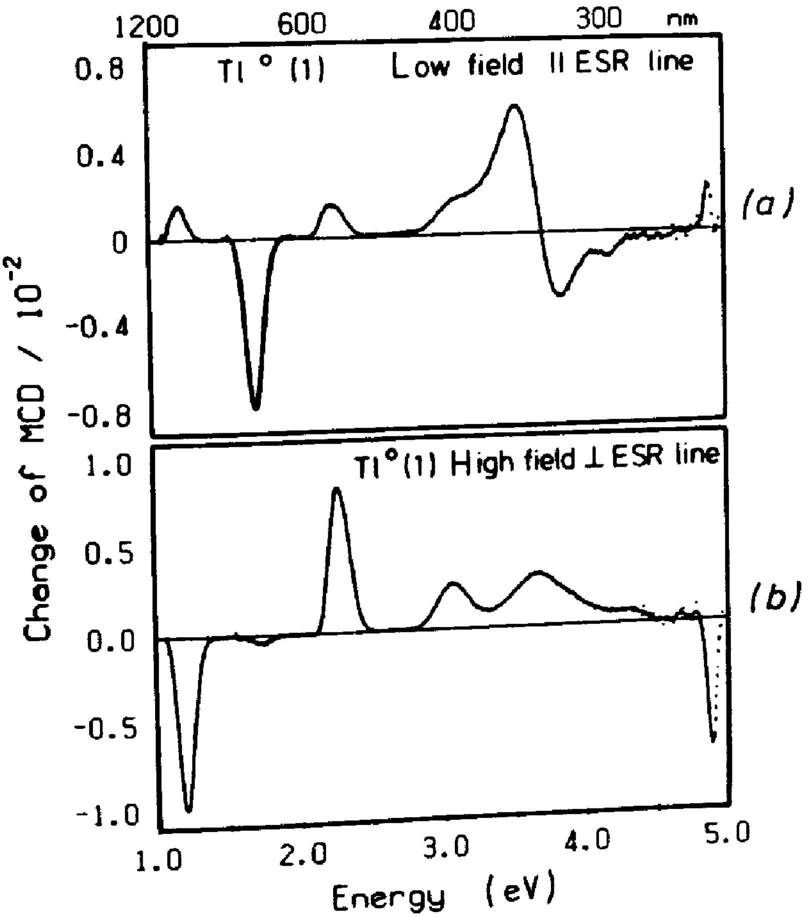

Figure 6.52 (*a*) Magnetic circular dichroism (MCD) at 1.4 K of the *parallel* Tl^0(1) centers in KCl as tagged by the low-field ESR line. (*b*) The same for the *perpendicular* Tl^0(1) centers tagged by their high-field ESR line. Reprinted with permission from F. J. Ahlers, F. Lohse, J.-M. Spaeth, and L. F. Mollenauer, *Phys. Rev. B*, **28**, 1249 (1983).

B_0 parallel to the center axis; B_0 perpendicular to the center axis is shown in Figure 6.52*b*. Thus, the MCD tagged by ESR [69] reveals only the optical transitions belonging to one center or center orientation. Altogether, eight optical Tl^0(1) center absorptions were detected in this way. For the analogous Ga^0(1) and In^0(1) centers, the positions of the absorption bands can only be detected by this method, since they were buried in shoulders of other much stronger absorptions [84].

The MCD tagged by ESR of the V^{3+} defect on Ga sites in GaAs (Figure 6.53) reveals a rich optical absorption spectrum with several zero phonon lines and phonon replica, intracenter transitions into Jahn–Teller excited states, and an ionizing transition (at about 1.4 eV) into the conduction band. It is the first time that all the details of the optical spectrum, which were observed only partly by different authors, could unambiguously be assigned as belonging to one specific center. The sample also contained V^{2+} on Ga sites and another V-related complex defect, which make a clear assignment of optical bands very difficult otherwise [85, 86].

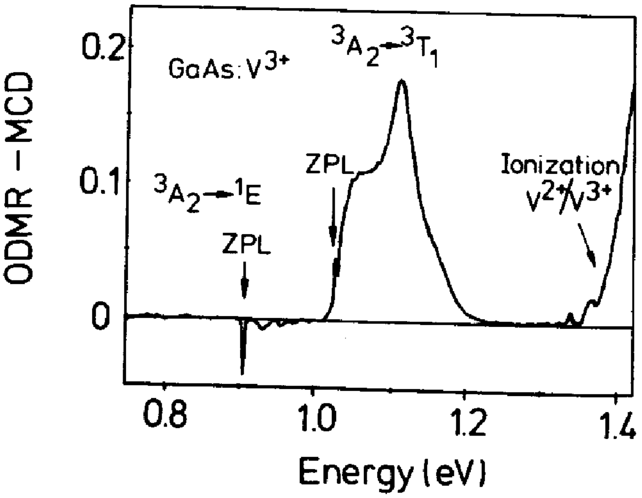

Figure 6.53 Excitation spectrum of the ODESR line of V_{Ga}^{3+} defects in high resistivity GaAs (MCD tagged by ESR). $T = 1.6$ K. Adapted from A. Görger, "Vanadiumzentren in GaAs und GaP: Magnetooptische und optisch nachgewiesene magnetische Resonanzuntersuchungen," Diplomarbeit, Universität-GH- Paderborn, 1987. J.-M. Spaeth, A. Görger, D. M. Hofmann, and B. K. Meyer, *Mater. Res. Sci. Symp. Proc.*, **104**, 363 (1988).

Similarly, for Fe^{3+} in InP such a rich optical spectrum can be identified. It was also found that the MCD and ESR can be observed in ionizing transitions to the bands.

As seen from Figure 6.52*a* this kind of experiment also gives information about the polarization of specific transitions; for example, the optical transition at 725 nm of the $Tl^0(1)$ centers in KCl is almost entirely polarized for the electrical vector perpendicular to the center axis since it is absent in Figure 6.52*b*.

6.7 Mapping With Optically Detected Electron Spin Resonance

In materials science the necessity to measure the presence of defects with spatial resolution is hard to meet by conventional methods. However, with emission and absorption, optical detection of ESR is possible within the limitations of the light beam diameter used to detect the resonances. Since, at least in principle, one can use (tunable) lasers, a resolution of approximately 10 × 10 μm should be obtainable.

Figure 6.54 shows the first experiment of this kind using the MCD of paramagnetic EL2 centers in GaAs (at 1350 nm) and the IR band of mid-gap EL2 (at 1 μm) to linearly map the concentration of the two charge states of the EL2 defect across ½ a wafer (thickness 300 μm, resolution ca. 300 μm). As can be seen the two charge states occur almost in anticorrelation: the mid-gap EL2 follows a W shape; the paramagnetic EL2 an M shape across the wafer. However, the defect is distributed rather homogeneously and it is not W-shaped as was assumed previously. This implies that the shallow acceptors, regulating the occupation of the paramagnetic EL2 and the mid-gap EL2, must exist in an M-shaped distribution. Their nature is still unknown [87, 88].

Clearly, two-dimensional mapping can be developed, and it is currently being undertaken for the EL2 charge states [89].

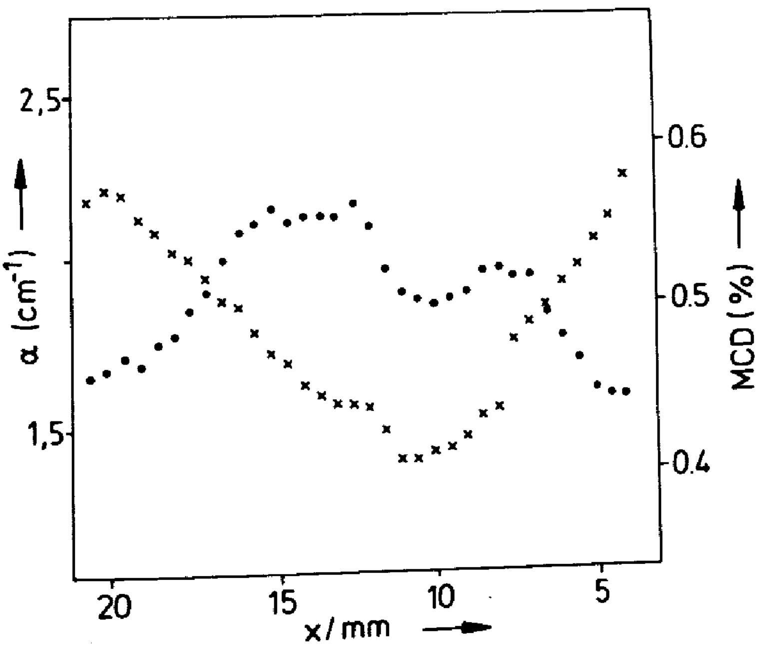

Figure 6.54 Spatially resolved measurement of the IR intracenter absorption band at 1.18 eV of mid-gap EL2 and of the MCD at 1350 nm of paramagnetic EL2 in semi-insulating *as-grown* GaAs across $\frac{1}{2}$ a wafer. Crosses represent paramagnetic EL2, dots represent mid-gap EL2. The spatial resolution was $0.3 \times 0.3\,\text{mm}^2$. Adapted with permission from M. Heinemann, B. K. Meyer, J.-M. Spaeth, and K. Löhnert, in E. R. Weber, Ed., "The Occupation of the Two Charge States of EL2 in LEC-Grown GaAs Wafers—a Mapping Investigation," *Defect Recognition and Image Processing in III–V Compounds II*, Elsevier, New York, 1987.

6.8 Spin Determination by Measuring the Magnetic Circular Dichroism

For the determination of the charge state of a defect it is important to know its spin state. It is normally not easily determined from ESR spectra unless there is a fine structure splitting resolved in a multielectron system. Otherwise, one must resort to ENDOR. However, using the MCD technique, there is yet another way to determine the spin state, as was realized only recently [85, 86].

The following discussion is precise for an orbital singlet state. When there is orbital degeneracy, the same ideas can be followed; however, possible splittings and spin mixings must be taken into account [86, 90].

The MCD is composed of a diamagnetic (dia) and a paramagnetic (para) term: $\text{MCD} = \text{MCD}_{\text{dia}} + \text{MCD}_{\text{para}}$.

The diamagnetic term is proportional to the magnetic field B_0, and it is usually small compared to the paramagnetic part MCD_{para}, which is proportional to the Brillouin function B_S

$$\text{MCD}_{\text{para}} = C\langle S_z\rangle = CSB_S \tag{41}$$

with

$$B_S(\mu) = 1/S\{(S + \tfrac{1}{2}) \coth[(S + 1)/2\mu] - \tfrac{1}{2} \coth(\mu/2)\} \tag{42}$$

$$\mu = g_e\mu_B B_0/kT \tag{43}$$

Here C is a proportionality constant (which depends on the nature of the excited states to which the optical transitions occur); g_e is the electronic g-factor. As will be seen, C does not enter in the determination of the spin state; B_S depends on the static magnetic field B_0, temperature T, and spin S of the defect as well as on its g-factor. The determination of S relies on the measurement of the Brillouin function, which, however, cannot be measured directly, because of the unknown diamagnetic contribution to the experimental MCD. However, since $\mathrm{MCD_{dia}}$ is linear in B, by measuring the total MCD for several magnetic fields (B_1, B_2) and temperatures (T_1, T_2) and following the ratio

$$R_{\mathrm{exp}} = \frac{\mathrm{MCD}(B_1, T_1) - \mathrm{MCD}(B_1, T_2)}{\mathrm{MCD}(B_2, T_1) - \mathrm{MCD}(B_2, T_2)} \tag{44}$$

gives

$$R(S) = \frac{B_S(S, B_1/T_1) - B_S(S, B_1/T_2)}{B_S(S, B_2/T_1) - B_S(S, B_2/T_2)} \tag{45}$$

Equation (45) can be calculated theoretically by varying spin S. Thus, the spin of the defect is determined when the condition $R_{\mathrm{exp}} = R(S)$ is fulfilled. Figure 6.55 shows this for V^{3+} defects on Ga sites in GaAs, which is a $3d^2$ configuration. As expected and known from ENDOR [91] $S = 1$. However, with the same method one can show that for V_{Ga}^{2+} $S = \frac{1}{2}$, a low-spin state exists [85, 86]. Although the ground state is ^2E, there is such a small orbital splitting, if any, that this does not influence the spin determination.

6.9 Experimental Aspects of Optically Detected Electron Spin Resonance and Optically Detected Electron Nuclear Double Resonance

The spectrometer to measure ODESR by a microwave-induced intensity change of the emission is very simple and was described earlier (e.g., [62]). Figure 6.56 shows a schematic description of the spectrometer that can measure microwave-induced MCD or MCPE. The sample is illuminated in a Faraday configuration; that is, the propagation direction of the circularly polarized light and B_0 are parallel. It is convenient for this configuration to produce the magnetic field with a split coil superconducting magnet.

The circularly polarized light is produced with the combination of a linear polarizer and a stress modulator [92]. This combination produces right and left circularly polarized light alternatively in one oscillating cycle of the modulator (frequency about 30 kHz). The absorption difference is detected by a lock-in detector and divided by the total light intensity. Thus, it is measured $(I^- - I^+)/(I^- + I^+)$.

The MCD can be measured to about 10^{-5} for an optical density of 1. For the measurement of the MCPE the stress modulator is placed behind the sample.

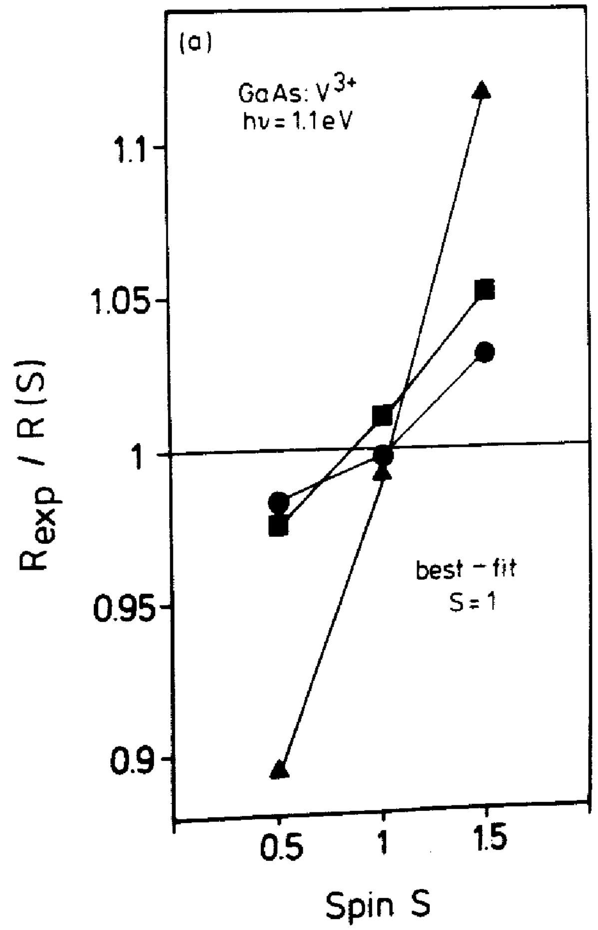

Figure 6.55 Spin determination of V_{Ga}^{3+} centers in GaAs. Ratio of R_{exp} and $R(S)$ as a function of S for V_{Ga} measured at 1.1 eV in high resistivity GaAs: V for the following pairs of magnetic field values: $B_1 = 1.3\,\mathrm{T}$, $B_2 = 0.5\,\mathrm{T}$ $B_1 = 1\,\mathrm{T}$, $B_2 = 0.8\,\mathrm{T}$ (circles), $B_1 = 0.8\,\mathrm{T}$, $B_2 = 0.5\,\mathrm{T}$ (squares), and (triangles) at temperatures $T_1 = 1.65\,\mathrm{K}$ and $T_2 = 4.2\,\mathrm{K}$ (the g-factor is 1.917). Adapted from A. Görger, B. K. Meyer, and J.-M. Spaeth, "Transition Metal Elements in III-V Semiconductors—A Study With Optically Detected Magnetic Resonance," in G. Grossman and L. Ledebo, Eds., *Semiinsulating III-V-Materials, Malmö 1988*, Hilger, Philadelphia, PA, 1988, p. 331; J.-M. Spaeth, A. Görger, D. M. Hofmann, and B. K. Meyer, *Mater. Res. Sci. Symp. Proc.*, **104**, 363 (1988).

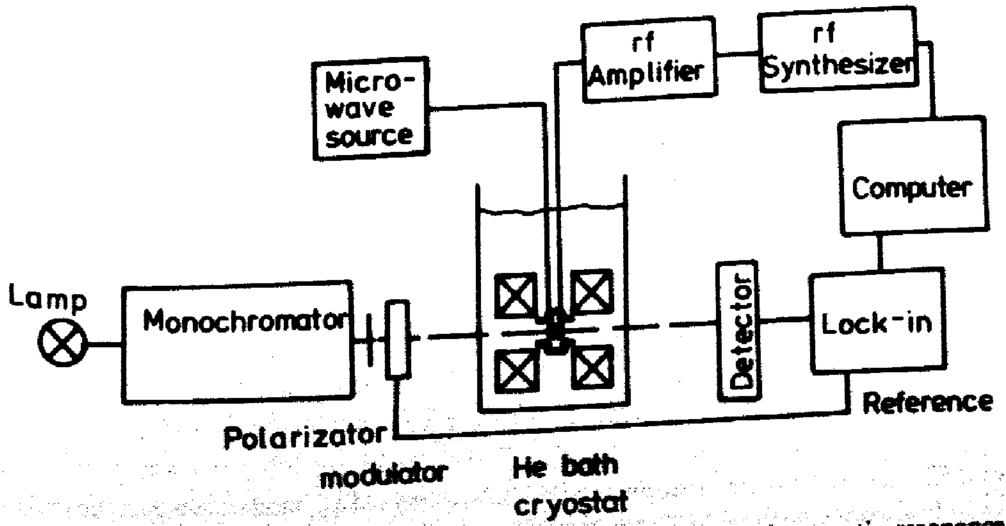

Figure 6.56 Block diagram of the apparatus for optical detection of magnetic resonance. For detection by MCPE the stress modulator and polarizer are placed behind the cryostat.

The sample temperature should be low (ca. 1.5 K), since the ground-state population difference and thus the ESR effect depend on B/T. It is advantageous to control the temperature within 0.1 K, since the irradiation of the sample with light, microwaves, and radio frequency tends to heat the sample and cause *background* signals.

Figure 6.57 presents a useful cavity design for ESR–ENDOR. It is a cylindrical cavity with the mode TE_{011}, which is open around the middle and can be described as two opposite top hats. It allows an optical access angle of 20° for both absorption and emission, which is necessary if one uses conventional light sources. The quality factor is around 5000. For the MCD one requires a highly stable light source, since small differences in absorption within the modulation phase of the stress modulator must be detected. Therefore, the use of lasers with a high amplitude noise of approximately 1% is not necessarily advantageous despite the higher light intensity. For ENDOR the radio frequency field is produced by four rods near the sample that act as two Helmholtz loops. To measure the MCD tagged by ESR and ENDOR it is convenient to computer control the spectrometer, including the positions of optical components, such as lenses.

The ODESR effect found so far is much too large compared to the previous simple explanation. This is especially the case for the EL2 centers in GaAs (Figure 6.48), where in each of the four central hyperfine ESR transitions a decrease of the MCD by about 25% was found, which means that the lines are homogeneous. However, the observation of ENDOR contradicts this deduction. Moreover, the ENDOR effect observed is of the same order as the ESR effect, which is not true in conventional solid-state defect ENDOR, where a

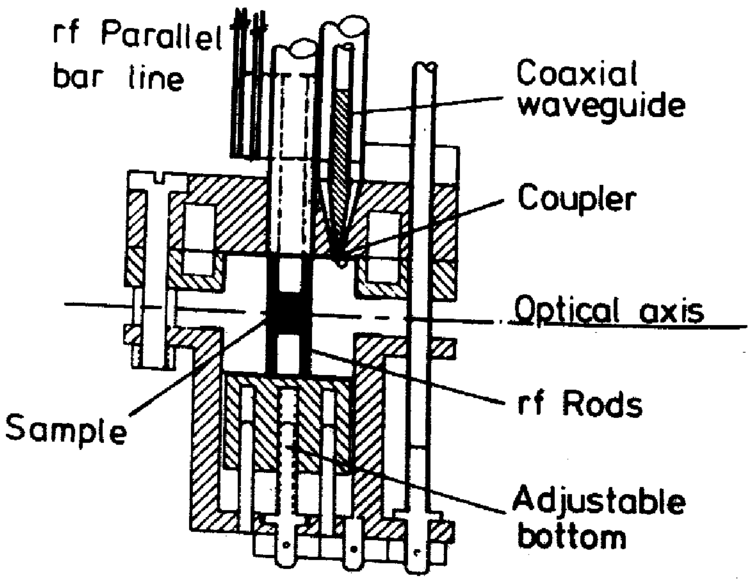

Figure 6.57 Cavity for optical detection of ESR. The cavity (TE_{011} mode) is open in the middle and allows optical access to about a 20° aperture. The coupling hook can be rotated during operation. The cavity can be floated with helium or be in a helium-exchange gas.

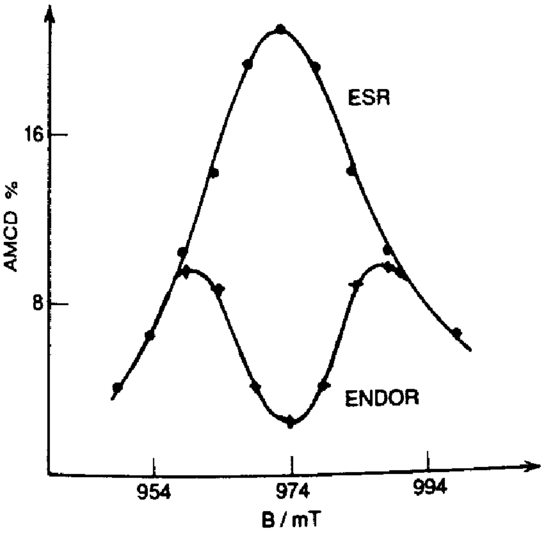

Figure 6.58 The ODESR and ODENDOR effect for paramagnetic EL2 defects in semi-insulating *as-grown* GaAs measured through one ^{75}As hyperfine ESR line. Adapted from D. M. Hofman, "Strukturaufklärung des EL2-Defektes in Galliumarsenid mit optisch nachgewiesener Elektronen–Kern–Doppelresonanz," doctoral dissertation, Universität-GH-Paderborn, 1987.

stationary effect of about 1 to 2% of the ESR is usually observed. Figure 6.58 shows the experimental result on the EL2 defect in GaAs: the ODENDOR effect is high in the wings in each ODESR line [83]. Neither Figure 6.58 nor the size of the observed effects, which are also too large in other cases like P-antisite defects in GaP [83,93] and $Pb^+(1)$ centers in the alkaline earth fluorides [73], are understood.

7 INTERPRETATION OF SUPERHYPERFINE AND QUADRUPOLE INTERACTION CONSTANTS

The atomistic structure of a defect is not all that is determined from ENDOR. The superhyperfine and quadrupole interaction constants and the orientation of the respective tensors give a detailed picture of the electronic structure of these defects. Therefore, they can be used to test a theoretical defect wave function to describe precisely the electronic structure.

However, the problem of the electronic defect structure is a complicated multielectron problem, and thus a theory is not in a position to calculate reliably the superhyperfine structure of defects, although in some simple cases there are quite good approximations available, such as in the field of color centers in alkali halides [94,95].

It is beyond the scope of this chapter to discuss the various approximations made to interpret the superhyperfine and quadrupole constants. Only a few very simple remarks are made, which can be useful when analyzing defect structures.

If it is clear from the system, that the amplitude of the wave function for the defect decreases with distance from the core of the defect (wide-gap insulators and deep-lying defects), then the anisotropic interaction constants b of more distant nuclei are rather well described by the simple classical point dipole–dipole approximation. The unpaired electron is replaced by a point-dipole residing at the center of the defect, and the interaction constant becomes:

$$\frac{b}{h} = \frac{\mu_0}{4\pi} g_I \mu_n g_e \mu_B \frac{1}{h} \frac{2}{R_\alpha^3} \tag{46}$$

where R_α is the distance between the center of the defect in the nucleus in question. This simple observation is useful for an assignment of nuclei of a particular shell. The isotropic constants a, especially for more distant nuclei, are more difficult to interpret, since transfer effects caused by overlaps of ion cores or atomic cores play a decisive role. The near-neighbor interactions are determined mostly by covalency effects [95].

The wave function is often expanded into a linear combination of atomic orbitals (LCAO) to obtain a rough picture of the distribution of the unpaired electrons.

$$\psi = \eta_0 \psi_0 + \sum_i \eta_i \psi_i \tag{47}$$

where ψ_0 is the wave function of the unpaired electron at the central (impurity) atom, η_0 is the localization of the wave function at the central atom, and η_i represents the s and p wave functions of the neighbor atoms i. In semiconductors like Si or III–V compounds, they are usually described as the hybridized s and p functions

$$\psi_i = \alpha_i \psi_s + \beta_i \psi_p \tag{48}$$

$$\alpha_i^2 + \beta_i^2 = 1 \tag{49}$$

where s and p are the outer occupied s and p orbitals; α_i^2 describes the part of the unpaired electron in s orbitals, and β_i^2 is the part of the unpaired electron in p orbitals of the neighbor i.

To get a picture of how the unpaired electron is localized in the central atom and distributed about the neighbors, one uses the experimentally determined superhyperfine constants a_i, b_i to determine the coefficients η_0, η_i and α_i, β_i by comparison to values of a_f, b_f for a full electron residing in the respective orbitals; a_f and b_f are calculated for the *free atom* with a Hartree–Fock method.

$$\eta_i^2 \alpha_i^2 = a_i / a_f \tag{50}$$

$$\eta_i^2 \beta_i^2 = b_i / b_f \tag{51}$$

As an example for Si $a_f = 4150$ MHz, $b_f = 101$ MHz [96].

Therefore,

$$\eta_i^2 \alpha_i^2 + \eta_i^2 \beta_i^2 = \eta_i^2 \tag{52}$$

and

$$\eta_i^2 = \left(\frac{|a_i|}{a_f} + \frac{|b_i|}{b_f}\right) N_i \tag{53}$$

where N_i is the number of equivalent nuclei in one shell; η_i^2 is called the *spin density*, and it is often plotted as a function of distance to show the localization or delocalization of the unpaired electrons.

This treatment is very rough and sometimes misleading. It is assumed that the electron (charge) distribution and the spin distribution are the same. This is generally not the case, as can be seen already from experiments. Often there are negative a values (see Table 6.4) observed indicating that there is a spin polarization [95], which can also reduce the observed b values, as was clearly shown for several O^- defects in various oxides [97]. For substitutional chalcogens in Si there is a first calculation now available of the superhyperfine structure from first principles that shows the decisive influence of spin polarization, which is caused by the influence of the valence band on the deep level states [98].

Particular difficulties arise for shallow defects, that are defects, the energy levels of which are very close to the band energies. The mixing with band states leads to an oscillating wave function making it difficult, if not impossible, to assign an interaction tensor identified by ENDOR to specific nuclei about the defect. Such observations were made for shallow donors in Si in the very early ENDOR spectroscopy [99, 100].

To determine the charge state of a defect it is useful to apply a rough estimate of the quadrupole interaction constants. At a specific nucleus it consists mainly of two parts: one caused by the field gradient of point charges present in the defect structure and one caused by the unpaired spin density moving in p (or d) orbitals of the atom (ion) to which it belongs [101].

$$q = q(p) + q(b) \tag{54}$$

with

$$q(p) = \frac{\pm n e^2 Q (1 - \gamma_\infty)}{8\pi\varepsilon_0 I(2I - 1)} \frac{1}{R^3} \tag{55}$$

$$q(b) = \frac{8e^2 Q(1 - \gamma)}{2I(I - 1)\mu_n g_I \mu_B} b(p) \tag{56}$$

where Q is the quadrupole moment, γ and γ_∞ are the Steinheimer antishielding factors, n is the number of point charges, and R is the distance between the nucleus and the point charge. The second term is determined from the experimental values of the anisotropic superhyperfine constant b; $b(p)$ is that part of b caused by unpaired spin density in p orbitals. The charge-density distribution is at least roughly estimated from an LCAO analysis of the superhyperfine-interaction parameters, and it is approximated as a point-charge distribution to calculate $q(p)$. Such a simple estimate was used successfully to decide on the site of Ni^{3+} centers in GaP (whether a Ni^{3+} was substitutional or on the tetrahedral interstitial site) [22] and more recently on the charge state of the As-interstitial-forming part of the paramagnetic EL2 defect in GaAs [70, 83].

8 CONCLUSIONS AND OUTLOOK

Magnetic multiple resonance methods offer a very powerful tool for the investigation of defects in solids. The availability of modern experimental techniques makes it possible to tackle difficult problems of interest in materials research. The development of these methods is by no means complete. Efforts to improve spatial resolution and also to use the absorption method for thin layers are encouraged. Whether it is possible by microoptic techniques to lead the light beam parallel rather than perpendicular to a surface should be tested. Time-resolved experiments allow not only the study of dynamical phenomena, but also the use of donor–acceptor recombination luminescence to detect hyperfine and superhyperfine structures with better resolution. Furthermore, the correlation spectroscopy correlating defect properties with other properties should be further developed. For instance a combination of magnetic resonance investigations with the spectroscopy that detects level positions in semiconductors certainly would be very fruitful.

References

1. G. Feher, *Phys. Rev.*, **114**, 1219, 1249 (1959).
2. T. M. McKinney and I. B. Goldberg, "Electron Spin Resonance," in B. W. Rossiter and J. F. Hamilton, Eds., *Physical Methods of Chemistry*, Vol. IIIB, 1989, Chap. 4.
3. A. Abragam and B. Bleaney, *Electron Paramagnetic Resonance of Transition Ions*, Clarendon, Oxford, 1970.
4. C. P. Slichter, *Principles of Magnetic Resonance*, Harper & Row, New York, 1963.
5. G. E. Pake and T. L. Estle, *The Physical Principles of Electron Paramagnetic Resonance*, 2nd ed., Benjamin, New York, 1973.
6. A. Schweiger, "ENDOR Methodology," in P. B. Ayscough Ed., *Electron Spin Resonance*, Specialist Periodical Report, The Chemical Society, Vol. 10b, 1987.
7. H. G. Grimmeiss, E. Janzen, H. Ennen, and O. Schirmer, *Phys. Rev. B*, **24**, 4571 (1981).
8. S. H. Muller, M. Sprenger, E. G. Sievers, and C. A. J. Ammerlaan, *Solid State Commun.*, **25**, 987 (1978).
9. J. Michel, J. R. Niklas, and J.-M. Spaeth, *Phys. Rev. Lett.*, **7**, 611 (1986).
10. P. Studzinski, "Paramagnetische Ionen zur Untersuchung struktureller Phasenübergänge–Eine ENDOR Untersuchung," doctoral dissertation, Universität-GH-Paderborn, 1985.

11. U. Kaufmann, W. H. Koschel, J. Schneider, and J. Weber, *Phys. Rev. B*, **19**, 3343 (1979).
12. U. Kaufmann and J. Schneider, *Solid State Commun.*, **25**, 1113 (1978).
13. E. Goovaerts, J. A. Andriessen, S. V. Nistor, and D. Schoemaker, *Phys. Rev. B*, **24**, 29 (1981).
14. J.-M. Spaeth, "Atomic Hydrogen as a Model Defect in Alkali Halides," in V. M. Tuchkevich and K. K. Shvarts, Eds., *Defects in Insulating Crystals*, Springer, New York, 1981, p. 232; *Z. Phys.*, **192**, 107 (1966).
15. G. Heder, J. R. Niklas, and J.-M. Spaeth, *Phys. Status Solidi B*, **100**, 567 (1980).
16. H. Seidel, *Z. Phys.*, **165**, 218, 239 (1961).
17. G. Heder, "ENDOR-Untersuchungen an atomarem Wasserstoff auf Anionengitterplatz in KCl," doctoral dissertation, Universität-GH-Paderborn, 1979.
18. J. R. Niklas and J.-M. Spaeth, *Solid State Commun.*, **46**, 121 (1983).
19. F. Beeler, M. Scheffler, O. Jepsen, and O. Gunnarson, *Mater. Res. Soc. Symp. Proc.*, **46**, 117 (1985).
20. T. E. Feuchtwang, *Phys. Rev.*, **126**, 1628 (1962).
21. J. Hage, J. R. Niklas, and J.-M. Spaeth, *Mater. Sci. Forum*, **10–12**, 259 (1986).
22. Y. Ueda, J. R. Niklas, J.-M. Spaeth, U. Kaufmann, and J. Schneider, *Solid State Commun.*, **46**, 127 (1983).
23. K. Möbius and R. Biehl, "Electron Nuclear–Nuclear Triple Resonance of Radicals in Solutions," in M. N. Dorio and J. H. Freed, Eds., *Multiple Electron Resonance Spectroscopy*, Plenum, New York, 1979.
24. C. P. Poole, Jr., *Electron Spin Resonance*, Wiley, New York, 1973.
25. H. Seidel, *Z. Angew. Phys.*, **14**, 21 (1962).
26. J. R. Niklas, "Elektronen–Kern–Doppelresonanz–Spektroskopie zur Strukturuntersuchung von Festkörperstörstellen," Habilitationsschrift, Universität-GH-Paderborn, 1983.
27. Ch. Hoentzsch, J. R. Niklas, and J.-M. Spaeth, *Rev. Sci. Instrum.*, **49**, 1100 (1978).
28. S. Greulich-Weber, J. R. Niklas, E. Weber, and J.-M. Spaeth, *Phys. Rev. B*, **30**, 6292 (1984).
29. J. R. Niklas, private communication.
30. M. U. A. Bromba and H. Ziegler, *Anal. Chem.*, **51**, 1760 (1979).
31. H. Ziegler, *Appl. Spectrosc.*, **35**, 88 (1981).
32. M. U. A. Bromba and H. Ziegler, *Anal. Chem.*, **55**, 648 (1983).
33. M. U. A. Bromba and H. Ziegler, *Anal. Chem.*, **56**, 2052 (1984).
34. H. Söthe, P. Studzinski, and J.-M. Spaeth, *Phys. Status Solidi B*, **130**, 339 (1985).
35. P. Wagner, C. Holm, E. Sirtl, R. Oeder, and W. Zulehner, "Chalcogens as Point Defects in Silicon," in P. Grosse, Ed., *Festkörperprobleme: Advances in Solid State Physics*, Vieweg, Braunschweig, Vol. **24**, 1984, p. 191.
36. J. Michel, J. R. Niklas, and J.-M. Spaeth, *Mater. Res. Soc. Symp. Proc.*, **104**, 185 (1988).
37. J. Michel, J. R. Niklas, J.-M. Spaeth, and C. Weinert, *Phys. Rev. Lett.*, **57**, 611 (1986).
38. J.-M. Spaeth, *Cryst. Lattice Defects and Amorphous Mater.*, **12**, 381 (1985).

39. Ch. Hoentzsch and J.-M. Spaeth, *Phys. Status Solidi B*, **94**, 479 (1979).
40. P. Studzinski, J. R. Niklas, and J.-M. Spaeth, *Phys. Status Solidi B*, **101**, 673 (1980).
41. P. Studzinski and J.-M. Spaeth, *Radia. Eff.*, **73**, 207 (1983).
42. P. Studzinski and J.-M. Spaeth, *J. Phys. C.*, **18**, 6441 (1986).
43. J. Bourgoin and M. Lannoo, "Point Defects in Semiconductors II, Experimental Aspects," in M. Cardona, Ed., *Springer Series in Solid State Sciences*, Vol. 35, Berlin, 1983.
44. S. Greulich-Weber, "ENDOR-Untersuchungen an Chalkogenen in Silizium," doctoral dissertation, Universität-GH-Paderborn, 1987.
45. S. Greulich-Weber, J. R. Niklas, and J.-M. Spaeth, *J. Phys. Condensed Matter*, **1**, 35 (1989).
46. J.-M. Spaeth and J. R. Niklas, in J. T. Devreese, Ed., *Recent Developments in Condensed Matter Physics*, **1**, Plenum, New York, 1981, p. 393.
47. J. R. Niklas and J.-M. Spaeth, *Phys. Status Solidi B*, **101**, 221 (1980).
48. R. C. Barklie, J. R. Niklas, and J.-M. Spaeth, *J. Phys. C*, **13**, 1745, 1757 (1980).
49. R. C. DuVarney, J. R. Niklas, and J.-M. Spaeth, *Phys. Status Solidi B*, **97**, 135 (1980).
50. B. Biehl, M. Plato, and K. Möbius, *J. Chem. Phys.*, **63**, 3515 (1975).
51. N. S. Dalal and C. A. McDowell, *Chem. Phys. Lett.*, **6**, 617 (1970).
52. J. R. Niklas, R. U. Bauer, and J.-M. Spaeth, *Phys. Status Solidi B*, **119**, 171 (1983).
53. R. C. DuVarney, J. R. Niklas, and J.-M. Spaeth, *Phys. Status Solidi B*, **128**, 673 (1985).
54. W. B. Fowler, Ed., *Physics of Color Centers*, Academic, New York, 1968.
55. D. L. Dexter, C. C. Klick, and G. A. Russell, *Phys. Rev.*, **100**, 603 (1955).
56. R. H. Bartram and A. M. Stoneham, *Solid State Commun.*, **17**, 1593 (1975).
57. M. Lannoo and J. Bourgoin, "Point Defects in Semiconductors I, Theoretical Aspects," in M. Cardona, Ed., *Springer Series in Solid State Sciences*, Vol. 22, Berlin, 1981.
58. W. B. Lynch and D. W. Pratt, *Magn. Reson. Rev.*, **10**, 111 (1985).
59. P. Edel, C. Henniers, Y. Merle d'Aubigné, R. Romestain, and Y. Twarowsky, *Phys. Rev. Lett.*, **28**, 1268 (1972).
60. P. Dawson, C. M. McDonagh, B. Henderson, and L. S. Welch, *J. Phys. C*, **11**, L983 (1978).
61. F. J. Ahlers, F. Lohse, and J.-M. Spaeth, *Solid State Commun.*, **43**, 321 (1982).
62. B. C. Cavenett, *Adv. Phys.*, **30**, 475 (1981).
63. J. D. Dunstan and J. J. Davies, *J. Phys. C.*, **12**, 2927 (1979).
64. K. P. O'Donnell, M. K. Lee, and G. D. Watkins, *Solid State Commun.*, **44**, 1015 (1982).
65. N. Killoran, B. C. Cavenett, M. Godlewski, A. T. Kennedy, and N. D. Wilsey, *Phys. Status Solidi B*, **116**, 425 (1982).
66. B. K. Meyer, Th. Hangleiter, J.-M. Spaeth, G. Strauch, Th. Zell, A. Winnacker, and R. H. Bartram, *J. Phys. C*, **18**, 1503 (1985).
67. D. Block, A. Hervé, and R. T. Cox, *Phys. Rev. B*, **25**, 6049 (1982).
68. L. F. Mollenauer and S. Pan, *Phys. Rev. B*, **6**, 772 (1972).

69. F. J. Ahlers, F. Lohse, J.-M. Spaeth, and L. F. Mollenauer, *Phys. Rev. B*, **28**, 1249 (1983).

70. B. K. Meyer, D. M. Hofmann, J. R. Niklas, and J.-M. Spaeth, *Phys. Rev. B*, **36**, 1332 (1987).

71. B. K. Meyer, J.-M. Spaeth, and M. Scheffler, *Phys. Rev. Lett.*, **52**, 851 (1984).

72. M. Fockele, F. Lohse, J.-M. Spaeth and R. H. Bartram, *J. Phys. Condens. Matter*, **1**, 13 (1989).

73. M. Fockele, "Strukturaufklärung laseraktiver Bleizentren in Erdalkalifluoriden," doctoral dissertation, Universität-GH-Paderborn, 1987.

74. A. Görger, B. K. Meyer, and J.-M. Spaeth, "Transition Metal Elements in III–V Semiconductors—A Study With Optically Detected Magnetic Resonance," in G. Grossmann and L. Ledebo, Eds., *Semiinsulating III-V-Materials, Malmö 1988*, Hilger, Philadelphia, PA, 1988, p. 331.

75. A. Görger, "Vanadiumzentren in GaAs und GaP: Magnetooptische und optisch nachgewiesene magnetische Resonanzuntersuchungen," Diplomarbeit, Universität-GH-Paderborn, 1987.

76. J.-M. Spaeth, A. Görger, M. Heinemann, D. M. Hofmann, and B. K. Meyer, *Proceedings of the E-MRS Conference, Les Editions de Physique*, Paris, 1987, XVI, p. 421.

77. K. P. Dinse and C. J. Winscon, "Optically Detected ENDOR Spectroscopy," in R. H. Clarke, Ed., *Triplet State ODMR Spectroscopy*, Wiley, New York, 1984.

78. G. Strauch, Th, Vetter, and A. Winnacker, *Phys. Lett.*, **34**, 160 (1983).

79. Y. Sano, K. Morigaki, and I. Hirabayashi, *Phys. Status Solidi*, **117A** and **118B**, 923 (1983).

80. F. Boulitrop, *Phys. Rev. B*, **28**, 6192 (1983).

81. J. J. Davis, J. E. Nichols, and R. P. Barnard, *J. Phys. C*, **18**, L93 (1985).

82. D. M. Hofmann, B. K. Meyer, F. Lohse, and J.-M. Spaeth, *Phys. Rev. Lett.*, **53**, 1187 (1984).

83. D. M. Hofmann, "Strukturaufklärung des EL2-Defektes in Galliumarsenid mit optisch nachgewiesener Elektronen–Kern–Doppelresonanz," doctoral dissertation, Universität-GH-Paderborn, 1987.

84. F. J. Ahlers, F. Lohse, Th. Hangleiter, J.-M. Spaeth, and R. H. Bartram, *J. Phys. C*, **17**, 4877 (1984).

85. J.-M. Spaeth, A. Görger, D. M. Hofmann, and B. K. Meyer, *Mater. Res. Sci. Symp. Proc.*, **104**, 363 (1988).

86. A. Görger, B. K. Meyer, J.-M. Spaeth, and A. M. Hennel, *Semicond. Sci. Technol.*, **3**, 832 (1988).

87. M. Heinemann, B. K. Meyer, J.-M. Spaeth, and K. Löhnert, in E. R. Weber, Ed., "The Occupation of the Two Charge States of EL2 in LEC-Grown GaAs Wafers—a Mapping Investigation," *Defect Recognition and Image Processing in III–V Compounds II*, Elsevier, New York, 1987.

88. K. Krambrock, private communication.

89. A. Winnacker, private communication.

90. B. Clerjaud, private communication.

91. J. Hage, J. R. Niklas, and J.-M. Spaeth, *J. Electron. Mater.*, **14a**, 1051 (1985).

92. S. N. Jasperson and S. E. Snatterley, *Rev. Sci. Instrum.*, **40**, 761 (1969).

93. B. K. Meyer and J.-M. Spaeth, *Phys. Rev. B*, **32**, 1409 (1985).

94. G. Heder, J.-M. Spaeth, and A. H. Harker, *J. Phys. C*, **13**, 4965 (1980).

95. A. M. Stoneham, *Theory of Defects in Insulators and Semiconductors*, Clarendon, Oxford, 1975.

96. G. D. Watkins, "Point Defects in Solids," in J. H. Crawford, Jr. and L. M. Slifkin, Eds., *Semiconductors and Molecular Crystals*, Vol. 2, Plenum, New York, 1975, p. 349.

97. F. J. Adrian, A. N. Jette, and J.-M. Spaeth, *Phys. Rev. B*, **31**, 3923 (1985).

98. H. Overhof, C. M. Weinert, and M. Scheffler, *Proceedings of the 15th International Conference on Defects in Semiconductors, Budapest, 1988, Materials Science Forum*, Vol. 38–41, Part 1, Trans. Tech. Publications Aedermannsdort, Switzerland, 1989, p. 293.

99. E. B. Hale and R. L. Mieher, *Phys. Rev.*, **184**, 751 (1969).

100. J. L. Ivey and R. L. Mieher, *Phys. Rev. B*, **11**, 822 (1975).

101. P. von Engelen, *Phys. Rev. B*, **22**, 3144 (1980).